AN ELECTRONICALLY STEERED ULTRASONIC TRANSDUCER

by

Samuel Harry Maslak

S.B., S.M., E.E., Massachusetts Institute of Technology
(1971)

SUBMITTED IN PARTIAL FULFILLMENT OF THE

REQUIREMENTS FOR THE DEGREE OF

DOCTOR OF SCIENCE

at the

MASSACHUSETTS INSTITUTE OF TECHNOLOGY
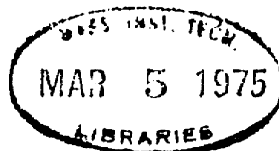
January, 1975

Signature of Author _____
      Department of Electrical Engineering, November 1, 1974

Certified by _____
                                              Thesis Supervisor

Accepted by _____
      Chairman, Departmental Committee on Graduate Students

AN ELECTRONICALLY STEERED ULTRASONIC TRANSDUCER

by

Samuel Harry Maslak

Submitted to the Department of Electrical Engineering on November 1, 1974 in partial fulfillment of the requirements for the Degree of Doctor of Science.

ABSTRACT

A recognized need exists for scanning ultrasonic transducers for medical applications. Manually scanned transducers are currently used, but such transducers are unsatisfactory due to their slow scan rates. The phased-array approach to the design of electronically steered transducers encounters difficulties due to the requirements of high directivity and operation at sub-millimeter wavelengths posed by medical applications.

A new type of scanning transducer is developed which avoids the "classic" phased-array problems. The new transducer is easy to drive and steer because it is a frequency-scanned device possessing only a single pair of electrical terminals. The transducer can be easily and reliably fabricated on a continuum piezoelectric substrate using standard photo-lithographic techniques; no grooving, etching or machining of the substrate is required. The directivity of the transducer radiation is essentially diffraction limited; therefore the transducer can be made as directive as desired simply by increasing its size.

A theoretical analysis of the new transducer is performed, and the performance of experimental transducers is evaluated. Measured and theoretical performance are in good agreement; moreover, the measured performance of two of the experimental devices suggests they could find immediate practical use in many medical ultrasonic applications.

THESIS SUPERVISOR: James K. Roberge
TITLE: Associate Professor of Electrical Engineering

ACKNOWLEDGEMENT

TABLE OF CONTENTS

Chapter 1

INTRODUCTION

This report describes a new type of scanning ultrasonic transducer which can be driven and electronically steered in a simple manner and is well-suited for operation at sub-millimeter wavelengths. While these features should be useful for many purposes, the primary motive for developing the new transducer is its potential value to medical ultrasound. Therefore, this chapter will begin by briefly considering possible applications of the transducer to this field and will outline special characteristics required of it. In the process, the need for a novel approach to the design of a scanning transducer will become evident.

1.1 Medical Applications

Ultrasound is of increasing value in medicine for the non-invasive study of the human body. Pulse echo techniques reminiscent of radar and sonar are used for such investigations as monitoring the motion of the mitral valve in the heart or imaging any of a variety of biological tissues.[1] Moving target indicator (MTI) techniques can be used to detect moving blood because of its doppler-shifted backscatter,[2] resulting in an important tool for the study of cardio-vascular disease. Ultrasonic diagnostic techniques are desirable because they are non-invasive, can obtain information not readily available by other techniques, and are apparently not subject to radiation hazards such as accompany x-ray methods.

Several present applications of ultrasound involve the use of scanning transducers. Examples include B-scan methods for the two-dimensional

visualization of the heart and abdominal areas.* Manually scanned trans-
ducers are used for these purposes, but such transducers are unsatisfactory
for many applications due to their slow scan rates. For example, when targets
pulsate with the cardiac cycle, as do arteries and the heart itself, it is
necessary to synchronize data taking with the cardiac cycle in order to
produce an acceptable image. As a result, only a few scans can be obtained
per heartbeat and the inherently slow scan rate of manually scanned trans-
ducers is further degraded. A composite picture of any detail may require
several minutes to produce.

On the other hand, electronically scanned transducers have the poten-
tial for very high scan rates. In many cases, it should be possible to
obtain complete images in a time short compared to the heart cycle, elimi-
nating the need for cardiac synchronization. Therefore, one area of possible
application for an electronically scanned transducer is simply to speed up
existing diagnostic techniques. This can be a significant contribution
when dealing with seriously ill patients.

The high scan rate available from an electronically steered transducer,
in addition to speeding up old techniques, should also allow new types of
measurements to be performed which were previously difficult or impossible.
Most intriguing are possibilities for obtaining stop-action images of major
arteries or portions of the heart during the cardiac cycle. The potential
medical diagnostic value of such images is self-evident. Alternatively,
the transducer might be coupled with pulse doppler techniques of blood-flow

---

*A B-scan indicates the positions of echo sources in a cross-sectional plane
by intensity modulating an oscilloscope. One coordinate of the scope is
distance from the transducer, the other coordinate is the lateral dimension
of the cross-sectional plane.

measurement[3,4,5] in order to obtain continuous cross-sectional blood velocity profiles in vessels throughout the cardiac cycle. Along this same line, the transducer should be of value in the newly developing area of doppler angiography.*

Another interesting potential application for an electronically scanned transducer is in combination with existing A-scan techniques.** These techniques are highly refined and widely used for such measurements as the position of the midline of the brain and the size of the fetal skull in pregnancy. A-scans are also used to obtain time-position recordings for study of the mitral valve.[1] In this connection, echos received from the mitral valve are displayed on the A-scope, and the distance between the valve and transducer is electronically determined from the echo transit time. A chart recording of this distance versus real time aids in the diagnosis of mitral valve disease.

Despite their value, considerable difficulty occurs in connection with A-scan methods because of their one-dimensional nature. Ultrasonic probes produce a narrow pencil-shaped beam normal to their face. In order to obtain maximum lateral resolution, this beam is made as narrow as possible (typically 0.5 to 1 cm). The A-scope displays the echo returns from the illuminated volume. Even if the returns were clean and free from spurious

---

*Angiography is the process of mapping the flow of blood and is used to determine whether blood flow in vessels is obstructed. This information is vital in assessing the extent of arteriosclerosis. Doppler angiography combines the use of ultrasound and MTI signal processing to map blood flow. Both continuous wave (CW) and pulse doppler angiography are possible. Pulse doppler methods utilize a range gate to obtain depth resolution, permitting three-dimensional angiography.

**An A-scan is a uni-dimensional scan, generally displayed on an "A-scope" with distance (echo transit time) on one axis and signal return on the other.

effects, it is easy to see that the identification of structures and diagnosis of abnormality must be very difficult. The pencil-shaped area of illumination provides no indication of geometric shape or orientation with respect to other structures. In practice, ultrasonic studies are made even more difficult by the presence of target clutter, probe reverberation, and false echos known as artifacts. Further confusing the issue, ultrasonic reflections from most tissues are composed of many specular components; therefore, a structure may repeatedly disappear and reappear as the transducer undergoes a small angular rotation. These factors explain why considerable expertise is required with an A-scope in order to locate desired targets and interpret the returns.

A major new application for an electronically scanned transducer could be to provide rapidly obtained B-scans to aid existing A-scope studies. The transducer would perform a B-scan covering the target area, and one of the scan directions comprising the B-scan image would be selected for display on the A-scope. The scan chosen would be indicated on the B-scope for reference. The value of the B-scope in this case is to provide the orientation that is lacking with the A-scope alone; also, some of the recognition problems due to target specularity may be avoided because echos would be returned from several directions.

An electronically steered transducer should be able to obtain a complete B-scan image in a time comparable to that required for an A-scan. In fact, the transducer proposed in this report can scan in several directions simultaneously, and the signals returned from each direction distinguished by their differing carrier frequencies. Thus, a complete B-scan could be performed just as quickly as a single A-scan. Increased scan rates that allow the simultaneous and continuous presentations of A- and B- scope displays would add a new dimension to virtually every ultrasonic technique

presently in use. Measurements which today require highly trained radiologists to perform and interpret may well become simple and uncomplicated with the geometrical orientation provided by simultaneous B-scan images. From the preceding discussion, we see that the B-scans would be of value even if they only covered a small angular range, say 20°.

We have described several applications that exploit the potentially high scan rates available from an electronically scanned transducer. However, many uses could be found for a scanning transducer that can be driven and steered in a simple manner. For example, the transducer could be incorporated into a CW or pulse doppler system and programmed to search an area and lock onto blood vessels. This feature is best appreciated after having made several unsuccessful attempts to locate and monitor blood flow in a vessel using a pulse doppler system. The ability to find and track a target would also facilitate automatic patient monitoring techniques. Of course, these functions could currently be performed with a mechanically scanned transducer, but this is less attractive due to the bulk and expense of mechanical scanning systems.

In summary, we have discussed several areas of medical ultrasound that could benefit from a practical electronically scanned transducer. In some instances, benefits would apply to currently existing techniques; in other cases new techniques would be made feasible. Success in any given case will depend upon the specific properties of the transducer. However, enough potentially valuable applications abound that any practical form of an electronically steered transducer is likely to find significant application.

1.2 Objectives and Constraints

In order to proceed with the analysis and design of the scanning transducer introduced in this report, we must:

1. Obtain an idealized model for the operating environment of the transducer, and

2. Provide a frame of reference for evaluating design objectives and constraints.

For purposes of ultrasonic propagation, most soft biological tissues may be viewed as slightly viscous fluids (bone and lung tissue are important exceptions, as we shall discuss shortly). The acoustic behavior of any fluid medium is summarized by its velocity of sonic propagation, c, and its characteristic impedance, Z. For most soft tissues in the human body, the values of these two parameters are within ten percent of their respective values for water, a fact easily observed from Table 1-1. We may conclude that many parts of the human body must look very much like water for purposes of ultrasonic radiation and transmission.

The preceding conclusion does not imply that small differences in the characteristic impedances of biological tissues are unimportant to medical ultrasound; indeed, impedance discontinuities are the sources of ultrasonic echos. However, for an acoustic wave normally incident upon a ten percent impedance discontinuity, only 0.3 percent of the incident energy is reflected. This figure increases to less than 0.8 percent for oblique incidence at 45°, assuming the discontinuity in velocity of propagation is also less than ten percent. Thus, we see that small variations in the impedances and sonic velocities of soft tissues should have little effect on the gross propagation of acoustic waves in the tissues, except to slightly increase attenuation due to scattering.

Table 1-1. Characteristic Impedances and Sonic Velocities
for Some Relevant Materials*

Material	Characteristic Impedance (units of 10^6 kg/m^2-sec)	Sonic Velocity (units of m/sec)
Biological		
Fat	1.38	1450
Muscle	1.7	1585
Brain	1.58	1541
Kidney	1.62	1561
Spleen	1.64	1566
Liver	1.65	1549
Blood	1.61	1570
Skull bone	7.8	4080
Non-biological		
Air (at STP)	.0004	343
Water (fresh)	1.48	1480

Table 1-2. One-way Attenuation for Relevant Materials
in the 1-15 MHz Frequency Range*

Material	Attenuation at 1 MHz (dB/cm)	Approximate Frequency Dependence
Biological		
Fat	0.63	f
Muscle	1.0	f
Brain	0.85	f
Kidney	1.0	f
Liver	0.94	f
Blood	0.18	f
Bone	12-18	f^2
Lung	41	?
Non-biological		
Air (at STP)	1.4	f^2
Water (fresh)	.002	f^2

* Data from references 1 and 5.

The major difference between the propagation of ultrasound in soft
biological tissues and in water is the relatively higher rate of attenuation
in soft tissues. At frequencies typically used for medical ultrasound,
1-15 MHz, the attenuation in biological materials is approximately propor-
tional to frequency. Biological attenuation constants are generally given
in units of dB/cm-MHz, a typical value for soft tissues being 1 dB/cm-MHz.
The attenuation rates for a variety of soft tissues are listed in Table 1-2,
though it should be realized that reported values have shown substantial
variations in literature (again, bone and lung tissue are special cases).
For purposes of comparison, the attenuation of acoustic propagation in
water is .002 dB/cm at 1 MHz. Unlike the soft tissues, water and most non-
biological fluids exhibit attenuation rates proportional to the square of
frequency.

The load seen by a transducer radiating into a fluid is determined by
the characteristic impedance of the fluid, and we have said that the charac-
teristic impedances of most biological tissues are nearly equal to that of
water. However, we can ask whether the presence of loss significantly alters
this situation, because the characteristic impedance of an absorbing fluid
must include an imaginary component to account for its loss. For small loss,
the magnitude of this imaginary part is proportional to the ratio of attenu-
ation in dB/cm to operating frequency.[6] An attenuation of 4 dB/cm-MHz would
account for an imaginary component equal to only one percent of the lossless
characteristic impedance. Evidently, the characteristic impedances of bio-
logical tissues may be considered real and unaffected by the presence of
loss. Together with earlier discussions, this observation leads to a very
important result -- that water and the human body are almost identical loads
insofar as a transducer is concerned. Consequently, transducer analysis and

experimentation can be conducted with water as the acoustic medium, and the results directly applied to medical ultrasound.

Though most tissues in the body transmit ultrasound very much like water, but with increased loss, there are important exceptions. Bone and calcified areas have characteristic impedances approximately five times higher than water, primarily due to the greater speed of sound in these materials. Thus, these substances are good sonic reflectors when in contact with soft tissues. In addition, they attenuate transmitted ultrasound much more severely than do most soft tissues. Attenuation rates between 10 and 20 dB/cm are common for these materials at 1 MHz; furthermore, their attenuation rates increase with the square of frequency up to several megahertz. Because of this severe attenuation, acoustic transmission through bone is very difficult and usually avoided.

Another significant type of obstruction to the transmission of ultrasound in the body is presented by air-filled tissues. The lungs are the most obvious example of these tissues, but gas in the intestines, stomach or bladder may also impede ultrasonic examinations. Difficulty of ultrasonic transmission through air-filled tissues is easily understood by computing the fraction of energy in a normally incident plane wave that is transmitted through an air/tissue interface: owing to the severe differences in characteristic impedances, acoustic energy will experience a 30 dB loss each way.

It is thus evident that bones, calcified areas and air-filled tissues constitute serious obstructions to ultrasonic transmission. The necessity of avoiding these structures determines some of the practical constraints of the medical ultrasonic operating environment. For example, the heart must be examined by directing a beam of ultrasound through a small area located

in the third or fourth intercostal space, near the sternum. This is done in
order to avoid transmission through ribs or lung. Therefore, any attempted
scanning of the heart must be done by angling the radiation through this
aperture. In fact, this sort of "limited accessibility" problem is fairly
common when viewing the body's vital organs, particularly the heart and brain,
because nature protected them with structures that, coincidentally, tend to
obstruct ultrasonic propagation.

One conclusion that may be drawn from these pragmatic requirements of
the clinical environment is that "line of sight" transmission is most suitable
to medical ultrasound, an observation supported by present practice. How-
ever, if line of sight operation is to be coupled with good lateral resolu-
tion, it is necessary to operate in the near field of an ultrasonic transducer,
before its beam has diverged. Therefore ultrasonic transducers are frequently
designed for protracted near fields, extending approximately to their targets
of interest. Since the propagation of ultrasound is governed by many of the
laws which apply to optics, it follows that the requirement for a long near
field is equivalent to specifying a narrow angular beamwidth in the far field
of the radiation pattern. Thus, ultrasonic transducers must be highly direc-
tional.

The frequency range used for medical ultrasonic work is determined
by two conflicting requirements: the need for good resolution, which implies
short wavelengths, and the prohibition from using high frequencies because
of their excessive attenuation rates. It follows from these criteria that
the typical frequencies used in medical ultrasound are in the range of
1-15 MHz. The upper frequency range is used for opthamological studies
and for monitoring peripheral blood flow, where very little penetration
depth is needed. The lower frequency range is used for deep penetration.

Frequencies less than 1 MHz are not generally used because diffraction and other resolution-degrading effects become severe.

We have discussed several factors which determine the operating environment and clinical constraints that must be met by any transducer used for medical ultrasound. These and other considerations are intended to provide a frame of reference for subsequent discussions of transducer characteristics. The considerations are summarized below:

1. For purposes of ultrasonic radiation and propagation, soft biological tissues "look" like water to a transducer. Consequently, transducer analysis and experimentation can be conducted with water as the acoustic medium, and the results directly applied to medical ultrasound.

2. Because of obstructions and the general inhomogeneity of the body, line of sight transmission methods are most suitable for medical ultrasound.

3. The frequency range under consideration is from 1-15 MHz, so acoustic wavelengths will range from 0.1 to 1.5 mm.

4. The transducer should have a deep near field to provide good lateral resolution. This is equivalent to requiring a highly directional transducer.

5. The transducer should be as efficient as possible because the returned signals will already be greatly attenuated by transmission through the body. It is only partly possible to compensate for poor efficiency by increasing transmitted power, because average ultrasonic intensities greater than 0.1 watt/cm^2 may pose a medical hazard due to joule heating or other direct biological interaction.[1]

6. In addition, it is desirable that the transducer should be reasonably rugged, lightweight and portable to enhance its clinical usefulness.

1.3 Approach

1.3.1 Difficulties with Phased Arrays

Electronically steered radiating structures are commonly found in radar and sonar systems. They are invariably implemented as phased arrays, and the design of this type of structure is well-advanced. However, when phased array techniques are applied to the design of medical ultrasonic transducers, important problems arise. These result from the need for operation with sub-millimeter wavelengths and the requirement of highly directional radiation characteristics, as discussed in the preceding section. In this thesis we will take an approach to the design of a scanning transducer which avoids classic phased array techniques and their attendant problems. The value of this new approach can be seen by examining some of the difficulties encountered with phased arrays.

The difficulty of constructing a phased array to operate at sub-millimeter wavelengths is simply a consequence of the small physical size demanded of the individual radiators of the array. It can be shown that the center-to-center spacing of the radiators comprising a phased array must be less than a half-wavelength if spurious radiation lobes are to be avoided. At 5 MHz, for example, this would require the width of each element of the array to be less than .15 mm (about .006 inch). Problems involving the handling, machining, and attaching of wires to such small structures are self-evident.

Another difficulty with small physical size results from material considerations. In many respects, the most desirable materials available for ultrasonic transducer construction are the ferroelectric ceramics.[7] These materials have very strong piezoelectric coupling coefficients, are easily produced and molded, and are symmetric in the plane transverse to their

direction of polarization (theory requires piezoelectric materials to be anisotropic). However, ferroelectric ceramics tend to be brittle and fragile; and since they are ceramics with microscopic grain sizes, they tend to crumble when lapped or etched too thin. Manufacturers contacted by the writer felt that the minimum dimension a ferroelectric ceramic may attain before it becomes uncomfortably fragile and likely to crumble is approximately 0.25 mm (.01 inch).

The foregoing problems associated with sub-millimeter wavelengths are by no means fundamental in character. Certainly, it should be possible to obtain ferroelectric ceramics with sufficiently small grain size to allow the requisite small dimensions, and ways could be found to machine such small radiators. However, the nature of the problems and the substantial engineering effort necessary to eliminate them make the phased array approach to a scanning transducer unattractive; a transducer produced by these means would likely be expensive and fragile.

The requirement of highly directional radiation leads to other difficulties common to all phased arrays possessing this characteristic. These problems involve the large number of individually phased radiators required to form the array, and the equally large number of transceivers and phase shifters required to drive them. Typically, transducers should have an aperture of at least 15 wavelengths in order to have sufficient directivity for medical applications. Using half-wavelength element spacing to prevent spurious lobes, it is apparent that 30 or more radiators, transceivers and phase shifters would be required. This number can in fact be reduced somewhat by careful design of the individual radiators forming the array and by tolerating the existance of a few spurious lobes, and some sharing of transceivers

and phase shifters is likely. Even so, prospects of building so many drivers

and connecting them to a small multi-element array remain unappealing.

We have implicitly assumed that the phased array under consideration is

a linear array, capable of scanning in one dimension only. An array able to

scan in two dimensions would square the number of radiators contemplated for

the linear array. Fortunately, the medical applications discussed earlier

depend only upon a transducer's ability to scan in one dimension. Two-

dimensional visualization is possible because range is determined by echo

transit time.

Perhaps the most compelling evidence of practical difficulties with the

phased array approach to the construction of medical ultrasonic transducers

is the observation that no such transducer is currently available, commer-

cially or on a routine laboratory basis. This is true despite the obvious

potential applications for a steerable transducer discussed earlier, and the

realization that these advantages have been apparent since the early 1950's.

Moreover, activity directed toward the development of the type of phased

array suitable for medical application has frequently been reported.[8,9,10,11]

These facts illustrate that despite the lack of fundamental problems prevent-

ing its construction, the impediments for constructing a suitable phased

array for medical application are not trivial.

1.3.2 Advantages of a New Approach

In this report we avoid many of the "classic" problems of phased arrays

by using a continuum transducer and employing a frequency scanning technique

for beam steering. Frequency scanning is often used with phased arrays; how-

ever, we will use a "zero-delay" method of frequency scanning that requires

no time delays or phase shifters. To introduce this scanning technique and

compare it with phased array methods, we will briefly review techniques for steering phased arrays.

The principles of phased array beam steering can be illustrated by the two-element array of Fig. 1-1. This array is composed of the two point sources, S_1 and S_2, which radiate spherical waves at frequency ω with amplitudes $Ae^{j\phi_1}$ and $Ae^{j\phi_2}$ respectively, where A is real and positive.* By superposition, the acoustic pressure at point P of Fig. 1-1 becomes

$$p(r,\theta) = \frac{A}{r_1} e^{j(\omega t + \phi_1 - \beta r_1)} + \frac{A}{r_2} e^{j(\omega t + \phi_2 - \beta r_2)} \quad , \qquad (1-1)$$

where r_1 and r_2 are the distances from point P to S_1 and S_2 respectively. If P is sufficiently distant that

$$\frac{1}{r_1} \approx \frac{1}{r_2} \approx \frac{1}{r} \quad , \qquad (1-2)$$

the pressure at P is approximately

$$P(r,\theta) = \frac{2A}{r} \left\{ \cos\left[(\Delta\phi - \beta dr)/2\right] \right\} \exp\left\{ j\left[\omega t + (\phi_1 + \phi_2 - \beta r_1 - \beta r_2)/2\right] \right\} \quad , \qquad (1-3)$$

where $\Delta\phi = \phi_1 - \phi_2$ and $dr = r_1 - r_2$. From Fig. 1-1,

$$dr = r_1 - r_2 = D\sin\theta \quad , \qquad (1-4)$$

and since the wavenumber is given by

$$\beta = \omega/c \quad , \qquad (1-5)$$

_____

*For present purposes, the amplitude of an acoustic spherical wave source can be defined in terms of the acoustic pressure amplitude at an arbitrary distance r from the source. Thus, a source of amplitude A and frequency ω would generate an acoustic pressure amplitude at distance r of

$$p(r) = \frac{A}{r} e^{j(\omega t - \beta r)} \quad ,$$

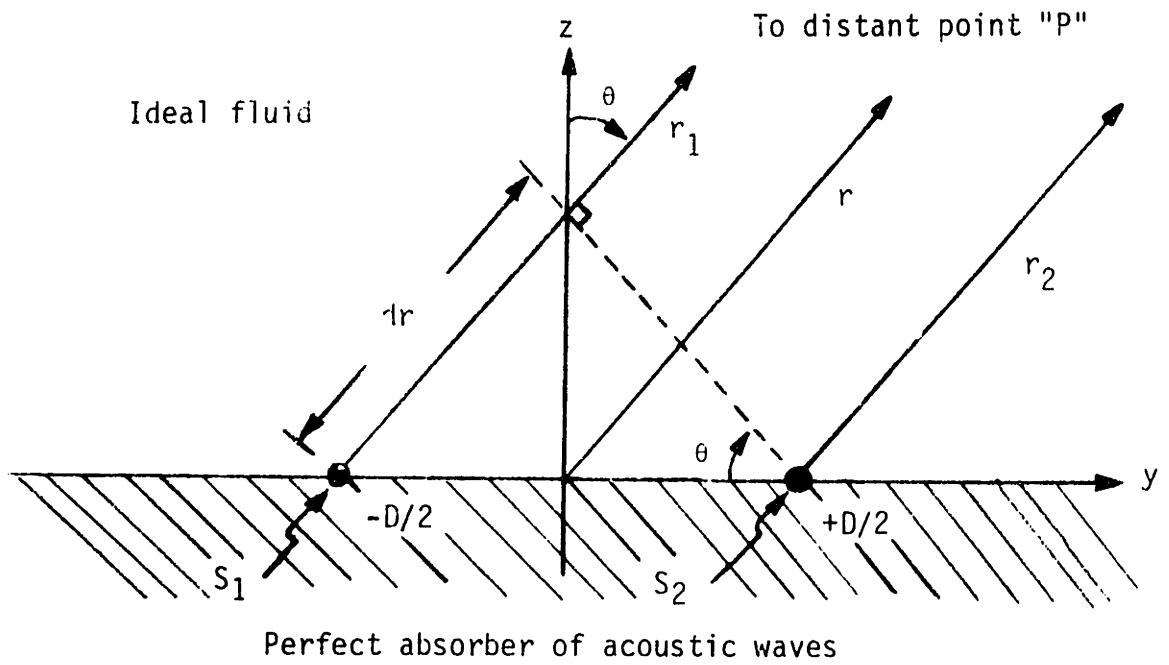where $\beta = \omega/c$, and c is the velocity of sound in the fluid.

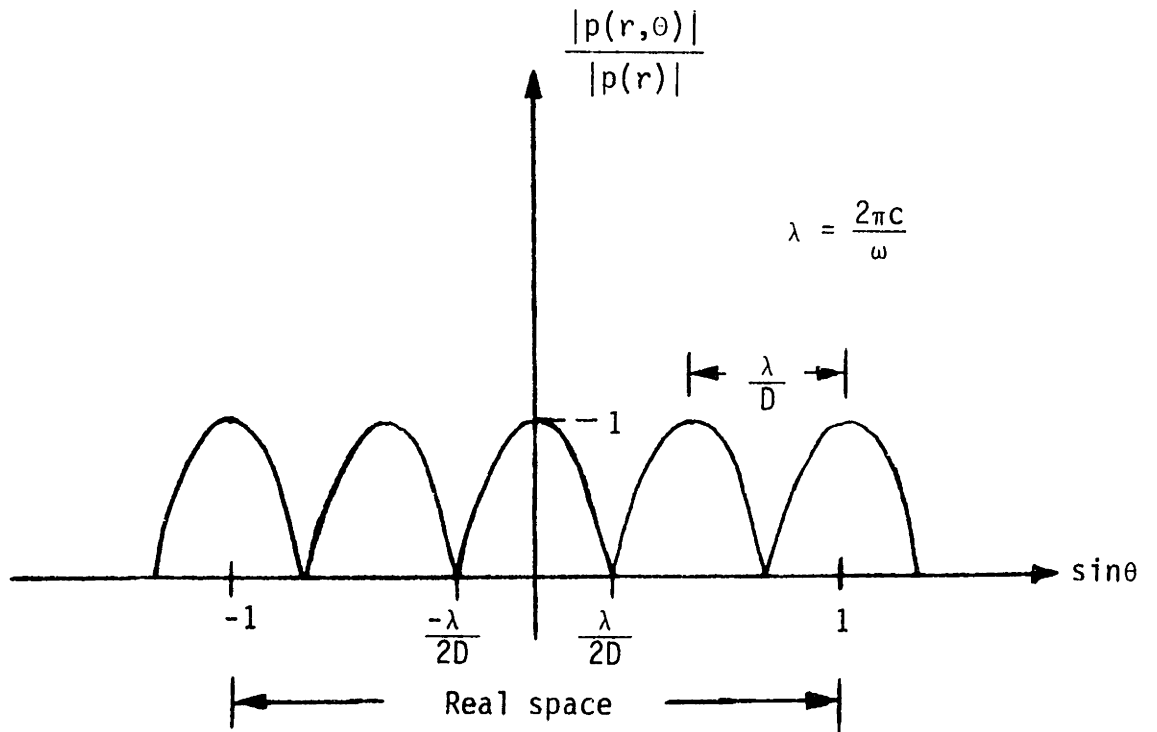Figure 1-1. A two-element phased array.

Figure 1-2. Normalized radiation pattern of a two-element array.

the following expression for the normalized angular dependence of the acoustic pressure amplitude results from equation (1-3),

$$\frac{|p(r,\theta)|}{|p(r)|} = |\cos\left[(\Delta\phi - \frac{\omega D}{c} \sin\theta)/2\right]| \quad , \qquad (1\text{-}6)$$

where $|p(r)|$ is the magnitude of the right side of (1-3) when $\Delta\phi = \theta = 0$.

Figure 1-2 presents a plot of (1-6) with $\sin\theta$ as the argument and under the condition $\Delta\phi = 0$. Notice that the choice of $\sin\theta$ for the abscissa prevents distortions which would result if the "real" angular variable, θ, were used. Furthermore, equation (1-6) shows that when $\Delta\phi$ is non-zero, the radiation pattern undergoes a translation in the "$\sin\theta$-space" of Fig. 1-2 that is proportional to the phase delay, $\Delta\phi$. This observation illustrates the "phase-scanning" technique of beam steering.[12]

From equation (1-6), we see that the maxima of the radiation lobes in Fig. 1-2 are determined by the phase condition,

$$\sin\theta = \frac{c}{D\omega}(\Delta\phi + 2\pi n) \quad , \qquad (1\text{-}7)$$

n integer. Only those lobes for which

$$|\sin\theta| \leq 1 \qquad (1\text{-}8)$$

actually exist in real space; however, when considering the steering of phased arrays, it is convenient to think of lobes as being steered in $\sin\theta$-space, and to imagine various lobes as moving in and out of "real space" defined by equation (1-8).

Every lobe in $\sin\theta$-space can be regarded as "named" by the integer n assigned to it by equation (1-7), thus the maximum, θ_n, of the nth lobe is given by

$$\sin\theta_n = \frac{c}{D\omega}(\Delta\phi + 2\pi n) \quad . \qquad (1\text{-}9)$$

Suppose we are interested in the "n^{th}" lobe, so that n is fixed in equation (1-9). The speed of sound, c, is a fixed property of the fluid medium and interelement spacing, D, must also be treated as fixed because it is a mechanical dimension of the array. Then it is evident from equation (1-9) that the direction, θ_n, of the nth lobe can be steered only by varying the phase difference, $\Delta\phi$, the frequency, ω, or some combination of these two parameters.

We have seen that phase scanning is accomplished by varying the phase delay, $\Delta\phi$, among the elements of the array while maintaining the frequency fixed. On the other hand, frequency scanning results from a simultaneous variation of frequency and phase. Referring to Fig. 1-1, suppose S_1 and S_2 are excited by the same waveform, $Ae^{j\omega t}$, but delayed by amounts T_1 and T_2 respectively. Then the amplitudes of S_1 and S_2 become $Ae^{j\omega(t-T_1)}$ and $Ae^{j\omega(t-T_2)}$ respectively; the interelement phase shift is

$$\Delta\phi = \omega(T_2 - T_1) = \omega\Delta T \quad . \tag{1-10}$$

Substituting (1-10) into (1-9),

$$\sin\theta_n = \frac{c}{D\omega}(\omega\Delta T + 2\pi n) = \frac{c}{D}(\Delta T + 2\pi n/\omega) \quad . \tag{1-11}$$

Equation (1-11) demonstrates frequency scanning for radiation lobes having a non-zero value of n, because $\sin\theta$ is determined by the excitation frequency ω. For any interelement spacing, D, and any non-zero value of n, it is possible to find a differential time delay, ΔT, and a frequency range over which the nth lobe can be directed at any angle in real space, yet no adjacent lobes (called "grating" lobes) will appear in real space. For example, given D and integer $n \geq 1$, choose

$$\Delta T = -D(1 + Rn)/c \tag{1-12}$$

where R is an arbitrary positive real number. Then an appropriate frequency range is given by

$$\frac{1+Rn}{2+Rn} \leq \frac{\omega}{\omega_0} \leq \frac{1+Rn}{Rn} \quad , \qquad (1-13)$$

with

$$\omega_0 = \frac{2\pi n c}{D(1+Rn)} \qquad (1-14)$$

Frequency scanning is often used with electromagnetic arrays where the time delays involved can be conveniently provided by the transmission lines or waveguides that are used to deliver power to the array elements.[13] However, for an acoustic array operating with the same size wavelength as an electromagnetic array, the time delays would have to be 10^5 times longer owing to the difference between the speed of light and the speed of sound. Therefore, frequency scanning is less attractive for acoustic arrays.

Consider equation (1-11) for the lobe n=0; in this case (1-11) simplifies to

$$\sin\theta_0 = c\Delta T/D \qquad (1-15)$$

Since ΔT is the amount by which the same excitation is delayed before being applied to the elements S_1 and S_2, equation (1-15) describes the technique of time-delay scanning whereby the beam is steered by varying the interelement time delay, ΔT. The principle advantage of time-delay scanning is that the beam direction is independent of frequency; therefore, time-delay scanning implements a very broadband array. The only frequency limitation is that when the frequency is increased beyond

$$\omega = \frac{\pi c}{2D} \qquad (1-16)$$

portions of a grating lobe may appear in real space. Of course, the practical difficulty with time-delay scanning is the problem of constructing broadband electronically-controlled time delays.

Now we consider a degenerate form of frequency scanning that is especially appropriate for acoustic arrays. For this scanning method, the interelement phase difference, $\Delta\phi$, remains fixed while the excitation frequency is varied. Frequency scanning, it may be recalled, involved the simultaneous variation of frequency and phase.

Suppose n=0 in equation (1-9), and let $\Delta\phi = \pi$; then (1-9) becomes

$$\sin\theta_0 = \frac{\pi c}{D\omega} , \qquad (1-17)$$

so the beam direction, θ_0, can clearly be scanned with frequency. Next, if we again set $\Delta\phi = \pi$, but let $n = -1$ in (1-9),

$$\sin\theta_{-1} = \frac{-\pi c}{D\omega} . \qquad (1-18)$$

It is apparent that $\theta_{-1} = \theta_0$ is a solution to (1-18) whenever θ_0 is a solution to (1-17). In other words, there are always (at least) two lobes in real space, one each at $\theta = \pm \theta_0$, with θ_0 given by equation (1-17). Of course, this result is exactly what one would expect due to the physical symmetry of the array when $\Delta\phi = \pi$. Consequently, we do not view this second lobe as a grating lobe, but recognize instead that the scanning technique is inherently bi-directional.

Notice that this steering technique differs from conventional frequency scanning in an important practical sense, because setting $\Delta\phi = \pi$ amounts to simply reversing the sign of the element excitations; therefore, no phase shifters or time delays are required. For this reason we will call this type of beam steering "zero-delay" frequency scanning. This zero-delay frequency scanning technique is the two-element array analog of the method used to steer the transducer to be introduced in this thesis.

The approach to the design of a scanning transducer taken in this report involves the application of zero-delay frequency scanning to a continuum transducer. For a continuum transducer, the piezoelectric substrate is not divided

into a mosaic of individual radiators, as would be the case for a phased array. Instead, an electrode pattern containing a sequence of metallic stripes is deposited upon the piezoelectric substrate; strong mechanical interelement coupling is permitted, and in some respects, exploited. Electromechanical coupling with the transducer is achieved by virtue of the piezoelectric nature of the substrate. The electrode pattern deposited upon the substrate has two electrical terminals, and when these terminals are excited by the application of a sinusoidal voltage, the transducer will radiate two narrow, symmetrically located beams, as discussed in connection with zero-delay frequency scanning. The directions of these beams are determined by the sinusoidal frequency of excitation according to an equation similar to (1-17).

This approach easily circumvents the two major phased array problems of sub-millimeter wavelengths and high directivity. No problems are posed by operating at sub-millimeter wavelengths because fabrication consists of the deposition of a metallic electrode pattern, which is easily accomplished using standard photolithographic techniques already developed for integrated circuit technology. Since the transducer is a continuum structure, no grinding, grooving, or other machining is necessary.

The requisite high directivity of the transducer is easily achieved with this structure because its directivity is essentially diffraction limited, just as is true of the piston transducers commonly used in ultrasound. Therefore, the transducer can be made as directive as is desired simply by increasing its width. No problems are posed by large numbers of elements, because the electrode pattern always possesses exactly two terminals. For this same reason, no phase shifters and only one transceiver are required to drive the device. These features make the transducer very easy to drive, and since it is steered by merely changing the frequency of its excitation, it is easily steered as well.

It is necessary to accept some performance constraints on the new trans-
ducer in return for the advantages gained. These performance constraints will
be explored throughout the remainder of the report. Some of them can be elim-
inated at the expense of slightly increased complexity in the drive or construc-
tion of the transducer. However, for many applications the new constraints are
not very restrictive, so an increase in complexity would not be required.

Chapter 2

PRINCIPLES OF OPERATION

This chapter develops several fundamental operating principles for a continuum transducer using "zero-delay" frequency scanning. Many variations of the same basic transducer are possible, but we must choose one version as a focus for study. This chapter will include a general analysis of this prototype transducer, emphasizing the method of beam steering. The analysis may be easily extended to other transducer variations.

2.1 Description of the Transducer

The prototype transducer is sketched in Fig. 2-1. It consists of a piezoelectric substrate on which metal electrodes have been applied in the form of equally spaced parallel stripes. As shown, alternate stripes are connected together to form two interdigitated electrodes. Fabrication of the interdigitated electrode structure is amenable to the use of standard photolithographic techniques as developed for integrated circuits. More importantly, however, the electrode pattern has only two electrical terminals. We shall see that this feature allows the transducer to be driven and steered simply.

2.2 Method of Analysis

The following assumptions pertaining to Fig. 2-1 will simplify the analysis of the transducer without changing its essential features:

1. The fluid in contact with the transducer is ideal and inviscid.

2. The width and length of the electroded region are sufficiently large that the transducer can be considered to occupy an infinite plane.

Ideal fluid

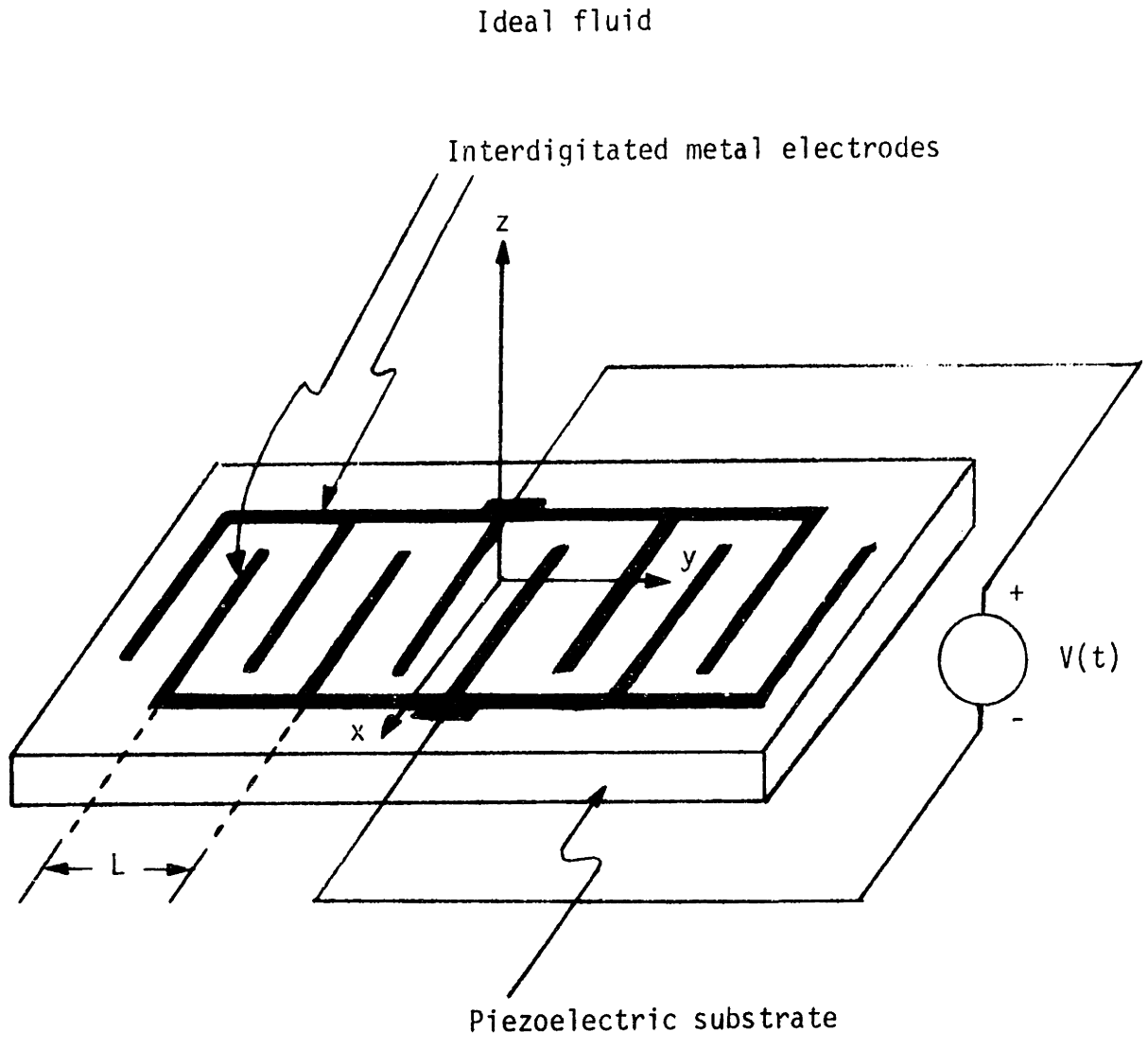Interdigitated metal electrodes

Figure 2-1. The prototype transducer.

3. The effects of the two interconnecting edge strips are ignored.

4. The thickness and mass of the electrodes are negligible.

These assumptions along with inherent symmetry reduce the problem to the two-dimensional situation shown in Fig. 2-2.

Our task in this chapter is to understand the general nature of the transducer, particularly the way it radiates and steers ultrasonic energy. Our method of analysis will be to assume a sinusoidal steady state, and to consider a spatial Fourier series expansion for the mechanical motion of the surface of the piezoelectric substrate. The total radiation from the transducer can then be determined by superposing the components generated by each term of the Fourier series. We shall see that a frequency range exists for which only the radiation from the first term of the spatial Fourier series can propagate; moreover, the direction of this radiation is determined by the sinusoidal frequency of the electrical drive. Therefore, the radiation from the transducer can be steered by varying its frequency of excitation. By analogy with the earlier discussion of phased-array frequency scanning, we shall call this type of scanning "zero-delay" frequency scanning because no delay lines or phase shifters are required for its implementation.

2.3 Sinusoidal Steady-State Analysis

Assume that the two-dimensional idealization of the transducer depicted in Fig. 2-2 is excited by a sinusoidal voltage, $V(t)$. Because the piezoelectric coupling and resulting mechanical interactions are linear and time-invariant, a sinusoidal steady state will be reached in which all stresses and particle motions vary sinusoidally in time, each with the same frequency, ω, as the exciting voltage, $V(t)$. In the following, therefore, we shall regard relevant variables as containing a suppressed $e^{j\omega t}$ time dependence.
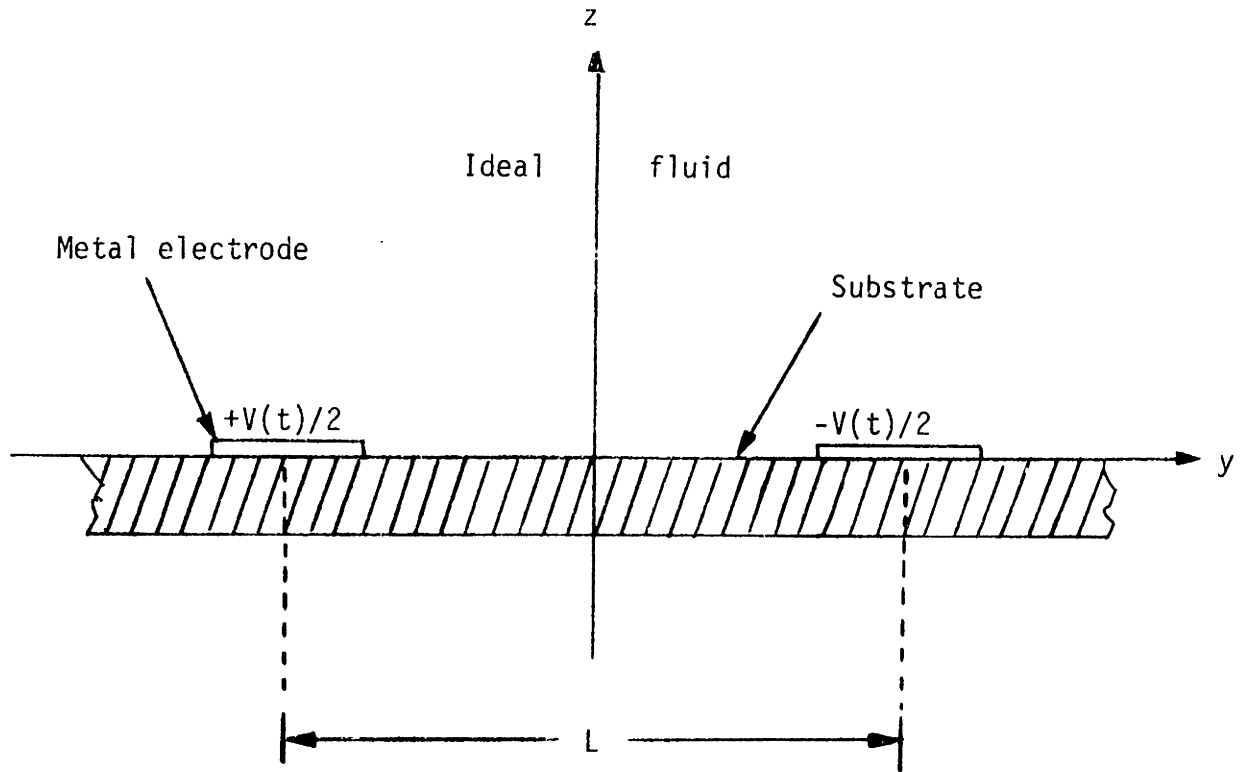
Figure 2-2. Two-dimensional idealization of the transducer.

Consider the incremental displacements from equilibrium of the material particles, $\vec{u}(x,y,z)$. In particular, consider the z-component of displacement at the surface of the piezoelectric substrate, $u_z(x,y,z)\big|_{z=0}$. In view of the two-dimensional character of Fig. 2-2, this quantity is independent of x, and since our attention is fixed on the plane at z=0, we will use the following notation for the z-component of substrate surface deformation.

$$\delta(y) = u_z(x,y,z)\Big|_{z=0} \qquad . \qquad (2-1)$$

Notice that $\delta(y)$ may be complex because of the suppressed $e^{j\omega t}$ time dependence.

Any function of a space coordinate can in general be expressed in terms of its spatial Fourier transform,*

$$\delta(y) = \frac{1}{2\pi} \int_{-\infty}^{+\infty} \Delta(\beta)e^{j\beta y} \, d\beta \quad , \qquad (2-2)$$

where

$$\Delta(\beta) = \int_{-\infty}^{+\infty} \delta(y)e^{-j\beta y} \, dy \qquad . \qquad (2-3)$$

For the situation depicted in Fig. 2-2, where the structure is periodic and of infinite length, the appropriate Fourier representation of $\delta(y)$ becomes a Fourier series,

$$\delta(y) = \sum_{n=-\infty}^{+\infty} \Delta_n e^{j2\pi ny/L} \quad , \qquad (2-4)$$

where

$$\Delta_n = \frac{1}{L} \int_{-\frac{L}{2}}^{\frac{L}{2}} \delta(y)e^{-j2\pi ny/L} \, dy \qquad . \qquad (2-5)$$

---

*The function must, of course, satisfy an appropriate set of mathematical conditions. These conditions are satisfied by virtually all functions of physical interest.

Symmetry can be used to obtain additional information about the Fourier representation for $\delta(y)$:

1. The physical situation in Fig. 2-2 is unchanged by a rotation of about 180° about the z-axis, except that the sign of the electrical excitation appears reversed. Because of the linearity of the piezoelectric coupling and mechanical laws, the result must be a change in the sign of $\delta(y)$. Since the rotation is equivalent to substituting -y for y, we conclude that

$$\delta(-y) = -\delta(y) \quad . \tag{2-6}$$

Using Eq. (2-6) in (2-5), there results

$$\Delta_{-n} = -\Delta_n \quad , \tag{2-7}$$

so the Fourier series for $\delta(y)$ contains only sine terms,

$$\delta(y) = 2j \sum_{n=1}^{\infty} \Delta_n \sin\left(\frac{2\pi n y}{L}\right) \quad . \tag{2-8}$$

2. If we start at any point on the transducer in Fig. 2-2 and move a distance $\frac{L}{2}$ parallel to the y-axis, we will again see the same physical situation, except that the sign of the sign of the excitation appears reversed. The linearity of the piezoelectric coupling and mechanical laws require a change in the sign of $\delta(y)$; in symbols,

$$\delta\left(y + \frac{L}{2}\right) = -\delta(y) \quad . \tag{2-9}$$

We conclude from Eqs. (2-9) and (2-5) that

$$\Delta_n = 0 \quad \text{for } n \text{ even} \quad . \tag{2-10}$$

Hence, the Fourier series for $\delta(y)$ contains only odd harmonics.

Using Eqs. (2-8) and (2-10), we obtain the following expression for $\delta(y)$

$$\delta(y) = 2j \sum_{\substack{n=1 \\ n \text{ odd}}}^{\infty} \Delta_n \sin\left(\frac{2\pi n y}{L}\right) \quad . \tag{2-11}$$

For the present, this series expansion for $\delta(y)$ is a sufficient description of the sinusoidal steady-state response of the transducer.

2.4 Acoustic Radiation in the Sinusoidal Steady State

The mechanical radiation into an ideal, inviscid fluid is completely determined by the normal component of particle velocity along its boundary. It is this fact which explains our interest in $\delta(y)$.

Consider a typical term in the expansion (2-11) of $\delta(y)$. By including its heretofore suppressed exponential time dependence, we can express the nth term as the sum of two traveling waves of substrate deformation normal to its surface,

$$2j\Delta_n \sin\left(\frac{2\pi ny}{L}\right)e^{j\omega t} = \Lambda_n \exp j\left(\omega t + \frac{2\pi n}{L}y\right) - \Delta_n \exp j\left(\omega t - \frac{2\pi n}{L}y\right) . \tag{2-12}$$

If the mechanical radiation into the fluid caused by a single traveling wave along its boundary were known, the response due to the two traveling waves of the nth term (2-12) could be found by superposition. Indeed, the response due to the entire infinite series (2-11) could be determined by superposing the radiation components generated by traveling "boundary" waves of normal displacement.

We derive the radiation into an ideal fluid generated by a traveling wave along a plane boundary in detail in Appendix I; for now, the results are merely described. Let the traveling wave on the boundary be given by

$$\delta(y) = \delta_0 e^{j(\omega t - \beta y)} , \tag{2-13}$$

as indicated in Fig. 2-3 (the figure is two-dimensional because the boundary is uniform in the $\pm x$- directions). Then, in general, a single plane wave will be radiated into the fluid. Its direction of propagation will lie in the YZ-
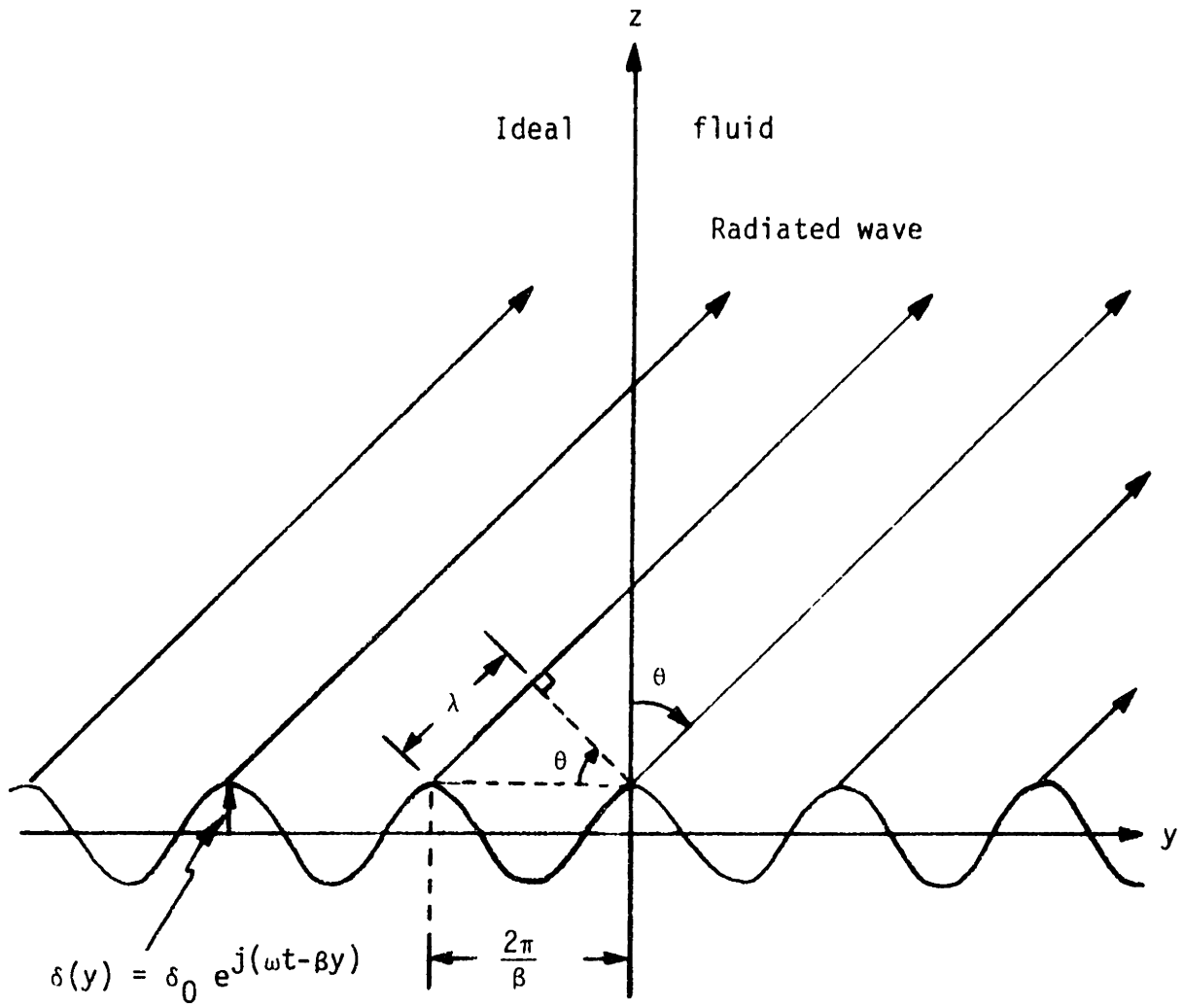
Figure 2-3. Radiation from a traveling wave on a plane boundary.

plane and will make an angle, θ, with the boundary normal. This angle, θ, is given by the solution of

$$\sin \theta = \frac{\beta c}{\omega} \quad , \tag{2-14}$$

where c is the speed of sound in the fluid.

Observe that equation (2-14) is suggested by the geometry of Fig. 2-3 by using the criterion that the path difference from two adjacent wave crests to a distant point in the radiation field must equal one wavelength of sound in the fluid. From Fig. 2-3,

$$\frac{2\pi}{\beta} \sin \theta = \lambda = \frac{2\pi c}{\omega} \quad , \tag{2-15}$$

which is simply (2-14) rearranged.

When

$$\left| \frac{\beta c}{\omega} \right| > 1 \quad , \tag{2-16}$$

no real solution to equation (2-14) exists. This situation corresponds in Fig. 2-3 to attempted radiation in a direction more than 90° from the boundary normal, which is physically impossible. In this case there can be no propagation into the fluid. Instead, an evanescent or "cutoff" wave is set up in the fluid immediately adjacent to the boundary. The amplitude of this wave decays exponentially with distance away from the boundary; the wave carries no real power and dissipates no energy. The rate of decay of this evanescent wave in water at medical ultrasonic frequencies is generally so great that its existence in the radiation field can be disregarded.

Suppose we think of the wave-number, β, in (2-13) as a spatial frequency. Then inequality (2-16) implies that low spatial frequencies will be radiated, while higher spatial frequencies will be cut off. These two spatial frequency ranges for propagation or cutoff correspond respectively to

$$|\beta| < \frac{\omega}{c} \qquad \text{radiation}$$

and

$$|\beta| > \frac{\omega}{c} \qquad \text{cutoff} \qquad . \qquad (2\text{-}17)$$

If the series expansion (2-11) for $\delta(y)$ is re-examined in view of equations (2-17), an important situation can be imagined. For this situation, only the lowest spatial frequency ($\beta = 2\pi/L$) in the expansion for $\delta(y)$ is propagated, while all higher frequencies ($\beta = 2\pi n/L$, $n \geq 3$) are cut off. From equations (2-17), this case requires

$$\left|\frac{2\pi c}{L\omega}\right| < 1$$

and

$$\left|\frac{2\pi n c}{L\omega}\right| > 1 \qquad \text{for } n \geq 3 \qquad . \qquad (2\text{-}18)$$

Because the parameters c and L are fixed for a specific transducer and fluid,* the relations (2-18) amount to restrictions on the temporal frequency, ω, of the excitation. Rearranging (2-18), these restrictions constrain ω to the range

$$\frac{2\pi c}{L} < \omega < \frac{6\pi c}{L} \qquad . \qquad (2\text{-}19)$$

Thus, when the temporal drive frequency, ω, obeys (2-19), radiation will occur only from the first term of the expansion (2-11) for $\delta(y)$. As expressed in equation (2-12), this term represents the sum of two oppositely-directed traveling waves. Accordingly, radiation will occur from each of the traveling waves at two equal angles, $\pm\,\theta$, with respect to the boundary normal. Applying (2-14) to the first term in expansion (2-11), the angle, θ, is given by

---

*Recall that L is the period of the interdigital electrode structure of the transducer, and c is the speed of sound in the fluid.

$$\sin \theta = \frac{2\pi c}{L\omega} \quad . \tag{2-20}$$

The overall picture of radiation by the transducer is clarified by a term-by-term accounting of the radiation from the expansion (2-11) for $\delta(y)$. For example, the fact that each term of (2-11) is the sum of two traveling waves of equal amplitude and opposite direction, as expressed in equation (2-12), simply means that the radiation will be symmetric about the boundary normal. This result is expected from Fig. 2-2 anyway, because the physical picture is unchanged by a 180° rotation about the Z-axis.

Next, consider the role of the temporal frequency, ω. With the help of relations (2-17), we see that for low frequencies, $\omega < \frac{2\pi c}{L}$, each term in (2-11) is cut off and no radiation occurs. When the frequency is increased to $\omega = \frac{2\pi c}{L}$, the first term in the expansion for $\delta(y)$ will begin radiating two lobes, one each at $\pm$ 90° from the boundary normal; all higher terms will remain cut off. As the frequency is increased further, these two radiation lobes will rotate toward the boundary normal, according to equation (2-20). This behavior is indicated in Fig. 2-4, and the directions of propagation, $\pm \theta$, are given by (2-20).

At a still higher frequency, radiation will begin from the next term, n = 3, in (2-11); radiation continues from the first term in directions determined by equation (2-20). Again, two lobes appear at $\theta = \pm$ 90°, and rotate toward the boundary normal with increasing frequency. Evidently this pattern is repeated in turn for each higher term. In general, the nth term will radiate for temporal frequencies, ω, given by

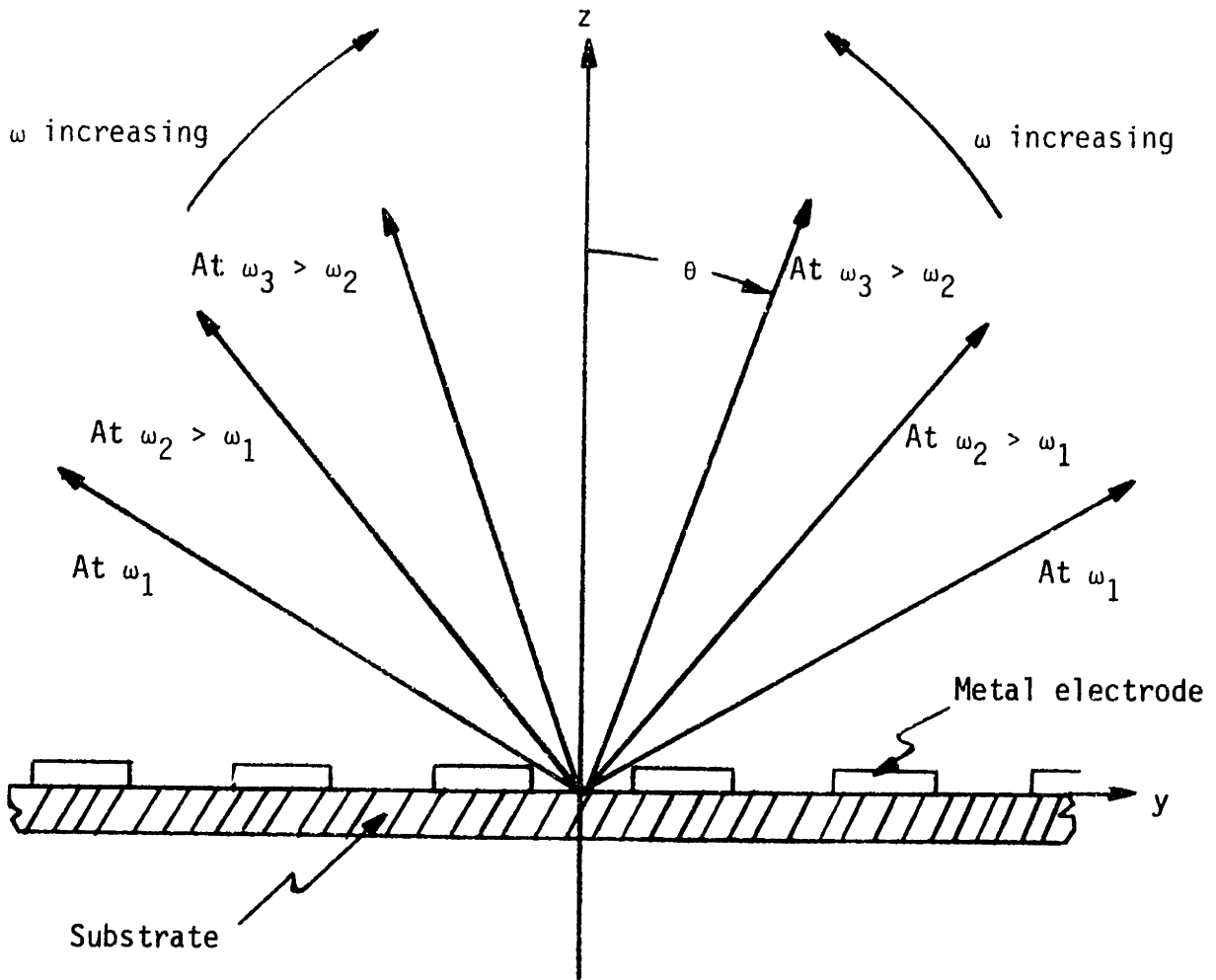$$\omega > \frac{2\pi n c}{L} \quad , \tag{2-21}$$

Figure 2-4. Radiation from the first term in expansion (2-11) for $\delta(y)$.

resulting in two lobes of radiation which makes angles of $\pm\,\theta$ with the boundary normal, where θ is given by

$$\sin\,\theta \;=\; \frac{2\pi nc}{L\omega} \qquad . \qquad\qquad (2\text{-}22)$$

Equations (2-21) and (2-22) are obtained from (2-17) and (2-14) respectively.

2.5 Beam Steering

Clearly, the radiation from the transducer is "steered" by changing its temporal frequency of excitation. This effect is called frequency scanning; and we are particularly interested in the situation for which radiation occurs from only the first term in the expansion for $\delta(y)$. In this case, there are no spurious lobes due to the higher order terms, and the directions of radiation are $\pm\,\theta$, where θ is determined by (2-20), repeated below,

$$\sin\,\theta \;=\; \frac{2\pi c}{L\omega} \qquad . \qquad\qquad (2\text{-}20)$$

This equation provides a quantitative description of the frequency scanning of the radiation pattern. It may be compared with equation (1-17) which describes "zero-delay" frequency scanning for a two-element phased array analog of the prototype transducer.

Because the transducer is frequency scanned, any constraint on frequency is mapped into a region of allowable radiation. Therefore, we can give an operational interpretation to the frequency range (2-19) over which only the first term of $\delta(y)$ propagates. Using (2-20), this frequency range is transformed into the angular range described by

$$90° \;>\; |\theta| \;>\; \sin^{-1}(1/3) \;\approx\; 19.5° \qquad . \qquad (2\text{-}23)*$$

---

*Notice that the absolute value of θ is used in (2-15) because of the symmetrical radiation at $\pm\,\theta$.
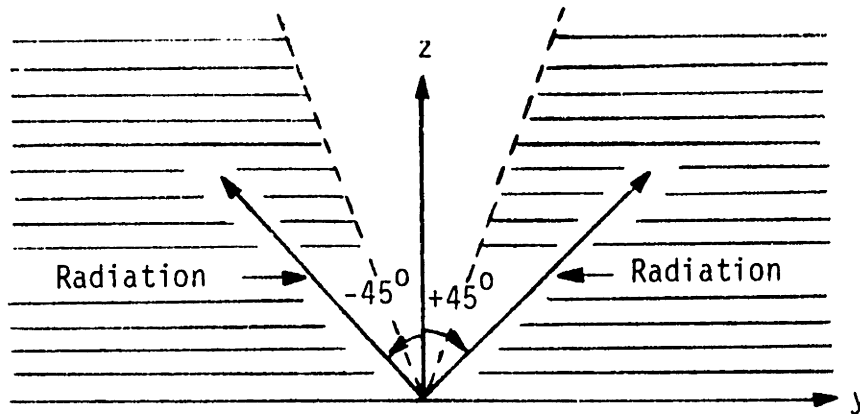
Figure 2-5a. Radiation from the transducer when $\omega = 2\sqrt{2}\,\pi c/L$. The shaded region is the angular range given by equation (2-23).
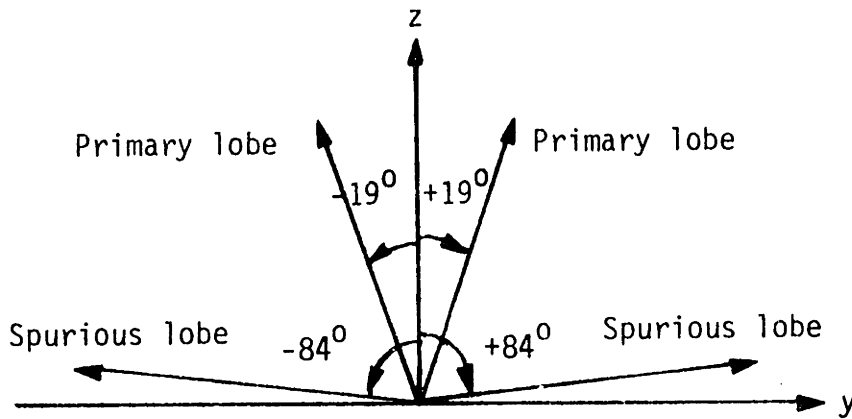

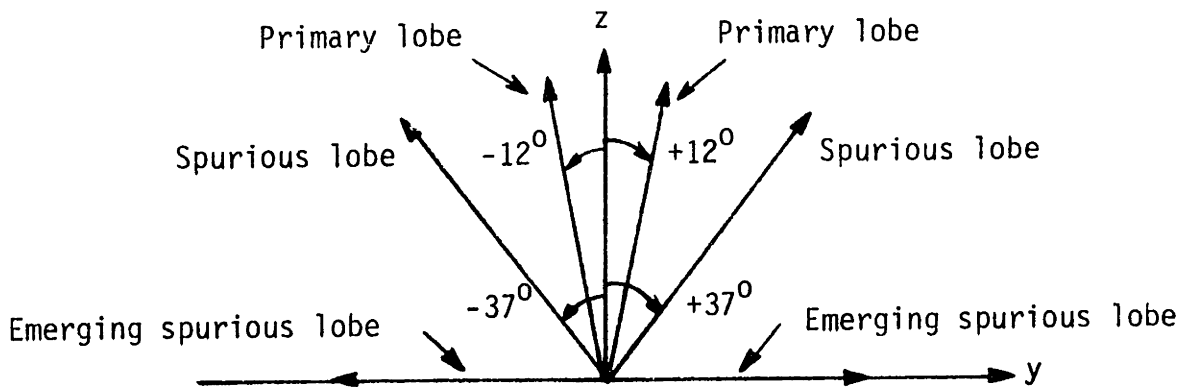Figure 2-5b. Radiation from the transducer when $\omega = 6.03\pi c/L$.

Figure 2-5c. Radiation from the transducer when $\omega = 10\pi c/L$.

Figure 2-5. Radiation patterns of the transducer for several frequencies.

Over this region, radiation occurs from the first term of $\delta(y)$ only, it is symmetrical about the boundary normal, and the radiation is frequency scanned as set forth by (2-20).

The situation is illustrated in Fig. 2-5. Figure 2-5a shows the radiation from the transducer for $\omega = \sqrt{2}\,\pi\,c/L$. Two symmetrically located lobes occur at $\theta = \pm\,45°$, as required by Eq. (2-20). No spurious lobes are present, because radiation cannot occur from the higher terms in the expansion for $\delta(y)$. The angular range given by (2-23) is inidicated in Fig. 2-5a.

Figure 2-5b illustrates the radiation from the transducer when $\omega = 6.03\,\pi\,c/L$, a frequency just outside the range given by (2-14). Now two spurious radiation lobes are present at $\theta \approx \pm\,84°$, along with the "primary" lobes at $\theta \approx \pm\,19.4°$. The spurious lobes are due to radiation from the $n = 3$ term in the expansion (2-11) for $\delta(y)$. The angles of radiation for the various lobes are given by Eq. (2-22) with $n = 1$ or $n = 3$.

Finally, Fig. 2-5c indicates the radiation pattern for $\omega = 10\,\pi\,c/L$. Once again, radiation occurs from the $n = 1$ and $n = 3$ terms, although the lobes now appear in different relative positions than in Fig. 2-5b. Observe that the $n = 3$ term has nearly "caught up" to the $n = 1$ lobe. This type of behavior holds for every term as the frequency increases, because Eq. (2-22) requires that the direction of radiation from each term assymptotically approaches $\theta = 0°$ as ω approaches infinity. Of course, a higher term can never actually "catch" a lower term.

2.6 Modifying the Radiation Field

We have seen that the radiation from the transducer is bi-directional, containing lobes symmetrically located about the transducer normal. For some applications, this bi-directionality may be unacceptable; therefore, we shall consider methods for breaking up the symmetry of the transducer in order to

eliminate its bi-directional character. In this section, we will be concerned with modifications to the prototype transducer that consist of the addition of electrodes, parallel to the existing metal stripes, which are then driven by appropriate voltage excitations. In a later chapter, we shall present a geometric method for eliminating the symmetric radiation lobes.

Consider the transducer shown in Fig. 2-6.* This transducer is a periodic structure similar to the prototype, but it contains three electrodes per spatial period, L, instead of only two. Every third electrode is connected together, yielding three electrical terminals for this device. These terminals are driven by the voltages $V_0(t)$, $V_1(t)$ and $V_2(t)$, which are defined with respect to an external datum node, as shown in Fig. 2-6.

Our method of analysis once again will be to assume a sinusoidal steady state, with each voltage source varying sinusoidally at the same frequency, ω, and to consider the spatial Fourier series expansion for $\delta^{(3)}(y)$.** We will express $\delta^{(3)}(y)$ as a linear combination of the responses $\delta_k^{(3)}(y)$, k = 0,1,2, which result from the unit amplitude excitation of the kth terminal of the transducer, with the other terminal voltages set to zero. By appropriately selecting the amplitudes of the terminal excitations, it is possible to obtain unidirectional radiation over a limited frequency range.

Suppose we apply unit amplitude excitation to terminal 0 of the structure in Fig. 2-6, and ground the other terminals. Then we may expand the resulting surface deformation, $\delta_0^{(3)}(y)$, as follows,

---

*This structure was suggested by the unidirectional surface wave transducer described in Ref. 14.

**The superscript notation, $\delta^{(3)}(y)$, is used to indicate that this expansion applies to the transducer with three electrodes per spatial period.

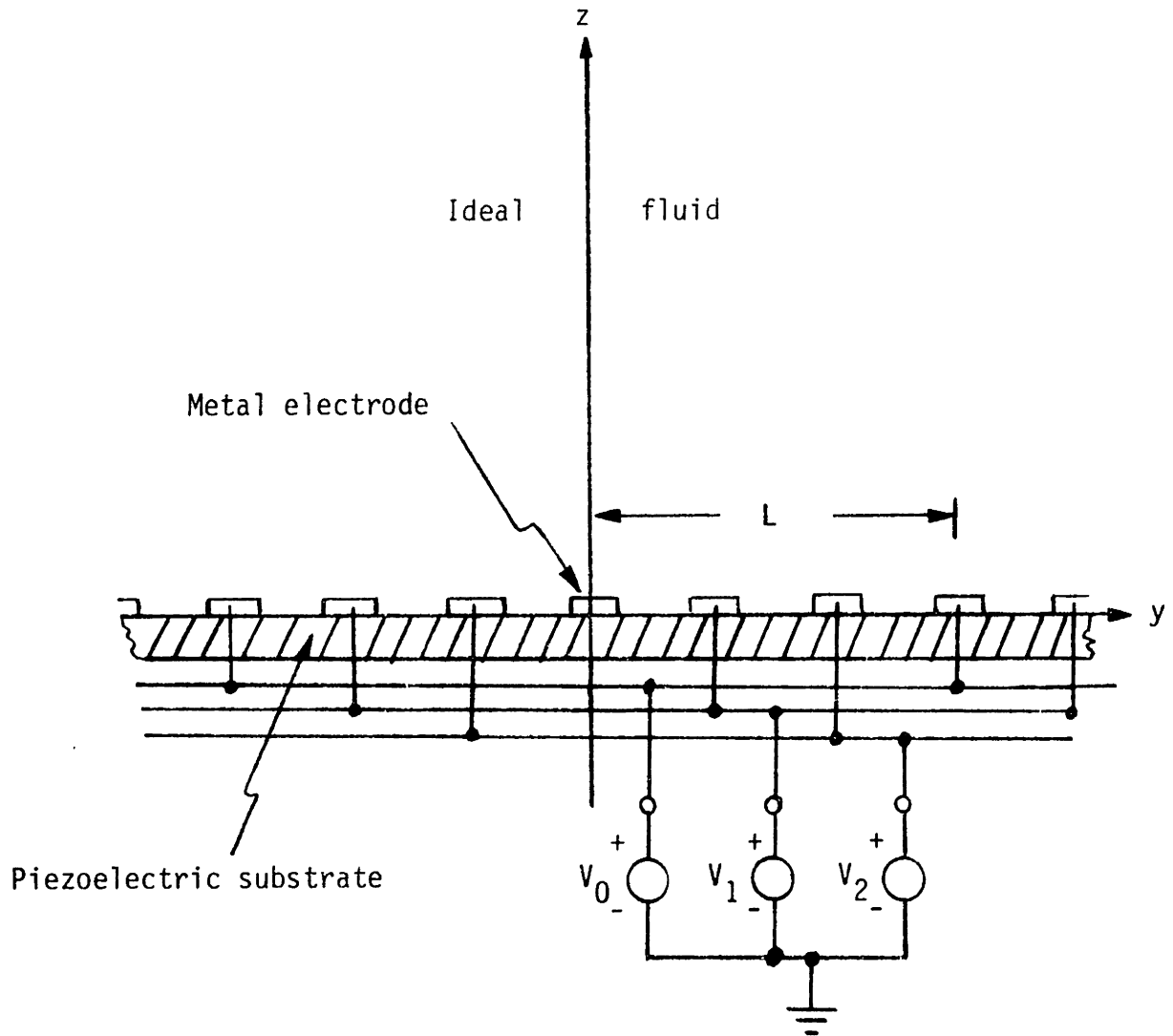z

Ideal   fluid

Metal electrode

L

y

Piezoelectric substrate

V_0 $+$ $-$

V_1 $+$ $-$

V_2 $+$ $-$

Figure 2-6. Two-dimensional idealization of the transducer with three elements per spatial period, L.

$$\delta_0{}^{(3)}(y) = \sum_{n=-\infty}^{+\infty} \Delta_n{}^{(3)} e^{j2\pi ny/L} \tag{2-24}$$

where

$$\Delta_n{}^{(3)} = \frac{1}{L} \int_{-\frac{L}{2}}^{\frac{L}{2}} \delta_0{}^{(3)}(y) e^{-j2\pi ny/L} dy \quad . \tag{2-25}$$

Next, consider the Fourier series expansion for $\delta_1{}^{(3)}(y)$. Clearly, this response must be identical to $\delta_0{}^{(3)}(y)$, but shifted to the right by amount $L/3$; therefore,

$$\delta_1{}^{(3)}(y) = \sum_{n=-\infty}^{+\infty} \Delta_n{}^{(3)} e^{j2\pi n(y-L/3)/L} \quad . \tag{2-26}$$

Similarly,

$$\delta_2{}^{(3)}(y) = \sum_{n=-\infty}^{+\infty} \Delta_n{}^{(3)} e^{j2\pi n(y-2L/3)/L} \quad . \tag{2-27}$$

By superposition, the net response, $\delta^{(3)}(y)$, due to arbitrary excitation amplitudes, V_0, V_1, and V_2, must be

$$\delta^{(3)}(y) = \sum_{n=-\infty}^{+\infty} \left[\sum_{k=0}^{2} V_k e^{-j2\pi nk/3} \right] \Delta_n{}^{(3)} e^{j2\pi ny/L} \quad . \tag{2-28}$$

If we select the amplitudes

$$V_k = V_0 e^{-j2\pi k/3} \quad , \quad k = 0,1,2 \quad ; \tag{2-29}$$

the term in brackets in equation (2-28) becomes

$$F_n{}^{(3)} \equiv V_0 \sum_{k=0}^{2} e^{-j2\pi(n+1)k/3} \quad . \tag{2-30}$$

By direct substitution, we can see that this term is periodic in n with period $N = 3$,

$$F_{n+3}^{(3)} = V_0 \sum_{k=0}^{2} e^{-j2\pi(n+1+3)k/3}$$

$$= V_0 \sum_{k=0}^{2} e^{-j2\pi(n+1)k/3} \qquad . \qquad (2\text{-}31)$$

Equation (2-30) can be summed to give

$$F_n^{(3)} = V_0 \sum_{k=0}^{2} \nu^k = V_0\left(\frac{1-\nu^3}{1-\nu}\right) \quad , \qquad (2\text{-}32)$$

where $\nu = e^{-j2\pi(n+1)/3}$. For n=0 and n=1, $F_n^{(3)} = 0$ because $\nu^3 = 1$. When $n = 2$, equation (2-32) is of the form $0/0$, but in this case (2-30) is easily summed to give $F_2^{(3)} = 3V_0$. Collecting these results,

$$F_n^{(3)} = \begin{cases} 3V_0 & \text{for} \quad n = 2 + 3q \quad , \quad q \quad \text{any integer} \\ \\ 0 & \text{otherwise} \quad . \qquad (2\text{-}33) \end{cases}$$

Substituting equation (2-33) into the expansion (2-28) for $\delta^{(3)}(y)$, we obtain

$$\delta_{(y)}^{(3)} = V_0 \sum_{q=-\infty}^{+\infty} \Delta_{3q+2}^{(3)} e^{j2\pi(eq+2)y/L} \qquad . \qquad (2\text{-}34)$$

From our earlier, term by term discussion of the radiation from a Fourier expansion for $\delta(y)$, we know that as the temporal frequency of excitation, ω, is increased from zero, radiation will begin from the term with the lowest (in absolute value) spatial frequency, while all higher terms remain cut off. For the expansion (2-34) above, this term with lowest spatial frequency would be the term

$$V_0 \Delta_{-1}^{(3)} e^{j(\omega t - 2\pi y/L)} \quad , \qquad (2\text{-}35)$$

where the $e^{j\omega t}$ time dependence has been included. Radiation would occur at the angle θ_{-1} given by

$$\sin \theta_{-1} = 2\pi c/L\omega \quad , \qquad (2\text{-}36)$$

which follows from (2-14). As the frequency is further increased, radiation will begin from each higher (in absolute value) term in succession, with the angles of radiation following from equation (2-14). From the expansion (2-34) for $\delta^{(3)}(y)$, we see that the first several of these terms, and their respective angles and frequency ranges for radiation, are:

$$n = -1 \quad ; \quad \sin \theta_{-1} = 2\pi c/L\omega \quad ; \quad \omega > \frac{2\pi c}{L} \qquad (2\text{-}37a)$$

$$n = 2 \quad ; \quad \sin \theta_{2} = -4\pi c/L\omega \quad ; \quad \omega > \frac{4\pi c}{L} \qquad (2\text{-}37b)$$

$$n = -4 \quad ; \quad \sin \theta_{-4} = 8\pi c/L\omega \quad ; \quad \omega > \frac{8\pi c}{L} \qquad (2\text{-}37c)$$

$$n = 5 \quad ; \quad \sin \theta_{5} = -10\pi c/L\omega \quad ; \quad \omega > \frac{10\pi c}{L} \qquad (2\text{-}37d)$$

For frequencies in the range

$$\frac{2\pi c}{L} < \omega < \frac{4\pi c}{L} \quad , \qquad (2\text{-}38)$$

unidirectional radiation will ensue at the angle θ_{-1} given by (2-37a), and no spurious lobes will be present. This frequency range corresponds to the angular region,

$$30° < \theta_{-1} < 90° \quad . \qquad (2\text{-}39)$$

Thus, by using three electrodes per period, L, instead of two, we have been able to break up the symmetry of the prototype transducer and achieve unidirectional radiation. Shortly, we will examine the practical implications of this technique, but first let us extend the preceding discussion to a transducer structure with N electrodes per spatial period. Figure 2-7 depicts such a transducer.

The analysis of the structure of Fig. 2-7 directly follows the case of N=3. Thus, we assume a sinusoidal steady state and consider a spatial Fourier
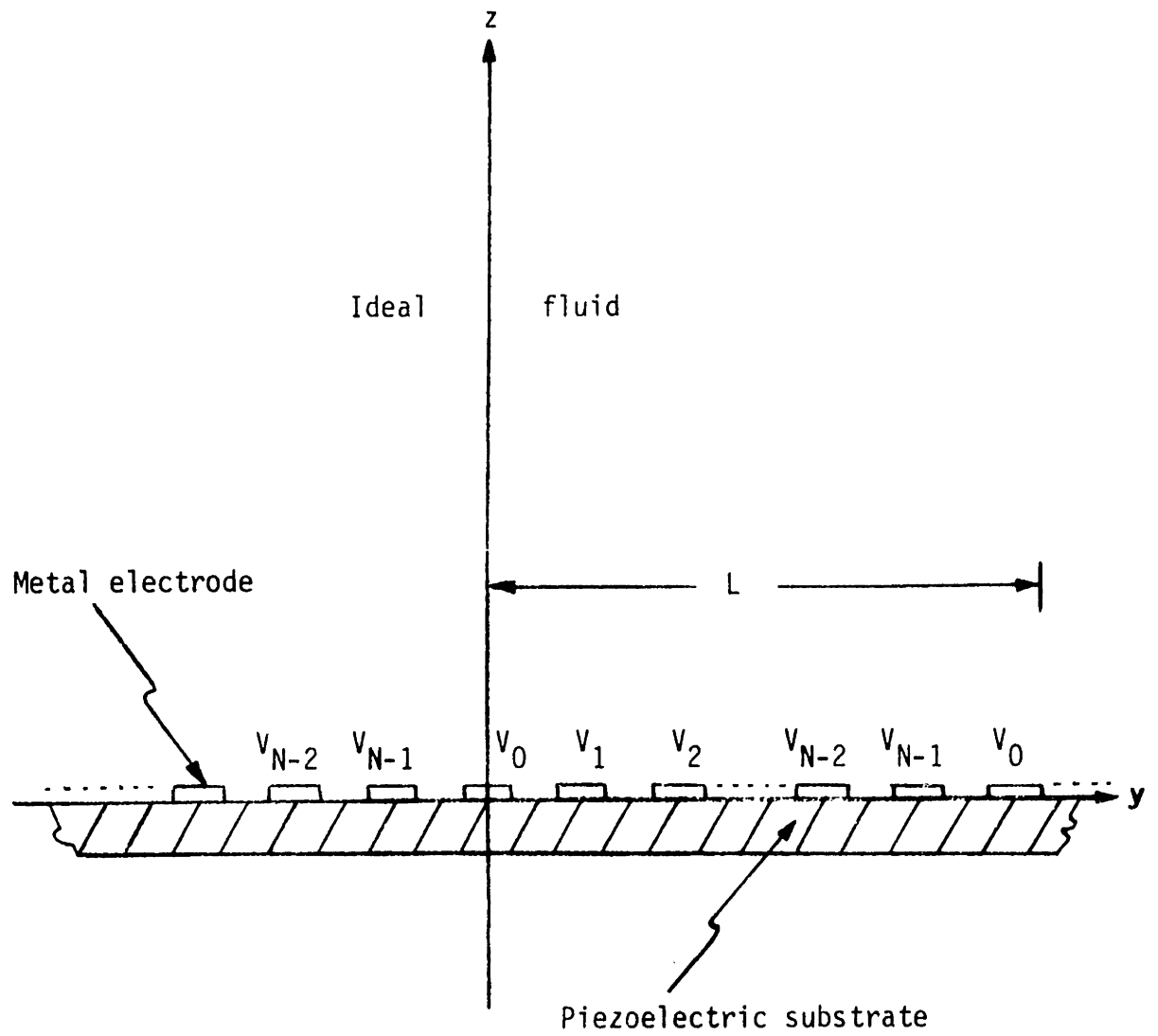
Figure 2-7. Two-dimensional idealization of the transducer with N elements per spatial period, L.

series expansion for $\delta^{(N)}(y)$, which we express as a linear combination of the responses $\delta_k^{(N)}(y)$, k=0,1,2,...N-1. Once again each $\delta_k^{(N)}(y)$ is the response due to a unit amplitude excitation of the kth terminal, with all other terminals grounded.

We begin with the Fourier series for $\delta_0^{(N)}(y)$,

$$\delta_0^{(N)}(y) = \sum_{n=-\infty}^{+\infty} \Delta_n^{(N)} e^{-j2\pi ny/L} \qquad (2\text{-}40)$$

where

$$\Delta_n^{(N)} = \frac{1}{L} \int_{-\frac{1}{2}}^{\frac{L}{2}} \delta_0^{(N)}(y) e^{-j2\pi ny/L} dy \qquad . \qquad (2\text{-}41)$$

For each k, the response $\delta_k^{(N)}(y)$ must be identical to $\delta_0^{(N)}(y)$, but shifted to the right by amount kL/N,

$$\delta_k^{(N)}(y) = \sum_{n=-\infty}^{+\infty} \Delta_n^{(N)} e^{j2\pi n(y-kL/N)} \quad , \quad k = 0,1,2,...N\text{-}1 \qquad .$$
$$(2\text{-}42)$$

Finally, the response $\delta^{(N)}(y)$ due to arbitrary excitation amplitudes, V_k, is found by superposition,

$$\delta^{(N)}(y) = \sum_{n=-\infty}^{+\infty} \left[\sum_{k=0}^{N-1} V_k e^{-j2\pi nk/N} \right] \Delta_n^{(N)} e^{j2\pi nk/L} \qquad . \qquad (2\text{-}43)$$

We define the term in brackets in equation (2-43) to be $F_n^{(N)}$,

$$F_n^{(N)} = V_0 \sum_{k=0}^{N-1} V_k e^{-j2\pi nk/N} \qquad . \qquad (2\text{-}44)$$

The reader may observe that $F_n^{(N)}$ as defined in (2-44) is the discrete Fourier transform (DFT) of the N-point sequence, V_k.[15] It follows from this observation, or by direct inspection of (2-44), that

$$F_{n+N}^{(N)} = F_n^{(N)} \qquad . \qquad (2\text{-}45)$$

In order to obtain radiation from the transducer that is free from spurious lobes, we would like to have $F_n^{(N)} = 0$ for each n except n = -1 (n = -1 is the primary lobe); but in view of equation (2-45), we can do no better than to have

$$F_n^{(N)} = 0 \quad \text{for all n except when}$$
$$n = qN - 1, \text{ q integer} \quad . \tag{2-46}$$

Extending the discussion leading to equation (2-33) to the present case of N electrodes, it is easy to see that the condition (2-46) would be satisfied if

$$V_k = V_0 e^{-j2\pi k/N} \quad , \quad k = 0,1,2,...N-1 \quad . \tag{2-47}*$$

Thus we observe that a transducer with N electrodes per spatial period, and driven by the terminal voltages

$$V_k(t) = V_0 e^{j(\omega t - 2\pi k/N)} \quad , \tag{2-48}$$

has a Fourier expansion for $\delta^{(N)}(y)$ of the form

$$\delta_{(y)}^{(N)} = \sum_{q=-\infty}^{+\infty} \Delta_{qN-1}^{(N)} e^{j2\pi(qN-1)y/L} \tag{2-49}$$

where

$$\Delta_n^{(N)} = \frac{1}{L} \int_{-\frac{L}{2}}^{\frac{L}{2}} \delta_0^{(N)}(y) e^{-j2\pi ny/L} dy \quad . \tag{2-50}$$

---

*This amplitude assignment is for undirectional radiation at positive angles, θ_{-1}, given by equation (2-36). For unidirectional radiation at negative angles, θ_1, where

$$\sin \theta_1 = -\frac{2\pi c}{L\omega} \quad ,$$

the amplitude assignment should be

$$V_k = V_0 e^{j2\pi k/N} \quad ; \quad k = 0,1,2,...N-1 \quad .$$

Notice that the results obtained originally for the prototype transducer are a special case of (2-49) and (2-50) with N=2. We have also seen that when N=3, unidirectional radiation can be achieved over the angular range (2-39). More generally, we see that in view of equation (2-49), it is possible to extend the region for unidirectional radiation when $N \geq 3$ to the angular range

$$\sin^{-1} \frac{1}{N-1} < \theta_{-1} < 90° \qquad\qquad (2-51)$$

where the direction, θ_{-1}, of the primary lobe is given by equation (2-36). Thus the benefit from increasing the number, N, of elements per spatial period is that the angular range (2-51) for unidirectional radiation is extended.

Now let us consider some practical implications of the technique for obtaining unidirectional radiation by the use of multiple electrodes per spatial period. Whereas the prototype transducer was a two-terminal device, which is very easily driven, the transducer shown in Fig. 2-6, for example, is a three-terminal device and requires a three-phase drive. If the transducer is to be used as a receiver, phase shifters would also be required to implement a three-phase to single-phase conversion. However, in practical terms, the cost of such increased drive complexity is not very great, at least for the cases of N=3 or N=4. The real problem with constructing a transducer with more than two electrodes per spatial period is that the electrode structure deposited upon the piezoelectric substrate would no longer be planar*. This fact implies that one would need multilayer techniques to interconnect the elements of the array. While various multilayer techniques exist, they would significantly increase the effort necessary to fabricate the transducer, and might result in a less rugged structure.

---

* A planar network is one which can be drawn on a plane without any elements crossing each other.

Nonetheless, the prospect of constructing a multilayer electrode structure remains attractive in comparison with the prospect of constructing a phased array. Certainly, a multielement structure with N=3 or N=4 appears to be a reasonable approach to the design of a scanning transducer in the event that a bi-directional radiation pattern is unacceptable.

Chapter 3

EFFECTS OF FINITE APERTURE AND PULSED EXCITATION

In the preceding chapter, we analyzed the prototype transducer under the assumption that it occupied an infinite plane, and found that for a given frequency of excitation the transducer radiates only in certain discrete directions. This result implies perfectly tight beams of radiation, but the radiation from a finite-size transducer must diverge with distance because of diffraction, and this divergence implies non-zero radiated beamwidths. Non-zero beamwidths would also result if the prototype transducer were excited by a pulse waveform rather than a steady state sinusoid. An excitation of finite duration contains energy over a band of frequencies, and since the transducer is frequency scanned, radiation will occur over the angular range which corresponds to the pulse frequency spectrum. Thus the effects on the radiation field due to restrictions on the duration of the transducer excitation, or upon transducer size, are quite similar in that they both serve to broaden the radiated beams. In this chapter we analyze the effects of these restrictions and consider their implications upon the design of practical transducers.

3.1 Finite Aperture

In Chapter 2, we considered an infinite plane transducer and developed an expression for the normal component of substrate surface deformation, $\delta(y)$, which we used to determine the radiation from the transducer. In order to model the effect of finite transducer size, we modify the preceding development by introducing a multiplicative aperture function, $A(x,y)$, such that the expression for the normal component of substrate surface deformation becomes

$$\delta'(x,y) = \delta(y)A(x,y) \quad . \tag{3-1}$$

The aperture function is non-zero over the finite region occupied by the transducer, and zero elsewhere. Two observations concerning the expression (3-1) are:

1. We have chosen to expand $\delta'(x,y)$ as the product of $\delta(y)$ and an aperture function, instead of simply considering $\delta'(x,y)$ directly, because we expect that for a moderately large transducer, $A(x,y)$ will be approximately unity over the region occupied by the transducer.

2. The assumption that $A(x,y)$ is uniformly zero over the region not occupied by the transducer is equivalent to assuming that the transducer is set in an infinite plane baffle. For most practical applications, no such baffle exists. However, we are concerned with transducer apertures several acoustic wavelengths in extent, and for such large transducers, the presence or absence of a baffle has little effect upon its radiation.

In Chapter 2, we obtained a spatial Fourier expansion for $\delta(y)$; this expansion reduced to a Fourier series in the single spatial variable, y, because $\delta(y)$ was periodic in y and independent of the x-coordinate. No such reduction is possible for Eq. (3-1), so the appropriate expansion is the two-dimensional Fourier transform:

$$\delta'(x,y) = \left(\frac{1}{2\pi}\right)^2 \iint\limits_{-\infty}^{+\infty} \Delta'(\beta_x,\beta_y) \, e^{j(\beta_x x + \beta_y y)} \, d\beta_x d\beta_y \tag{3-2}$$

where

$$\Delta'(\beta_x,\beta_y) = \iint\limits_{-\infty}^{+\infty} \delta'(x,y) e^{-j(\beta_x x + \beta_y y)} dxdy \quad . \tag{3-3}$$

In view of the rectangular geometry of the finite aperture transducer depicted in Fig. 3-1, it is reasonable to assume that the aperture function, $A(x,y)$, is separable in x and y,
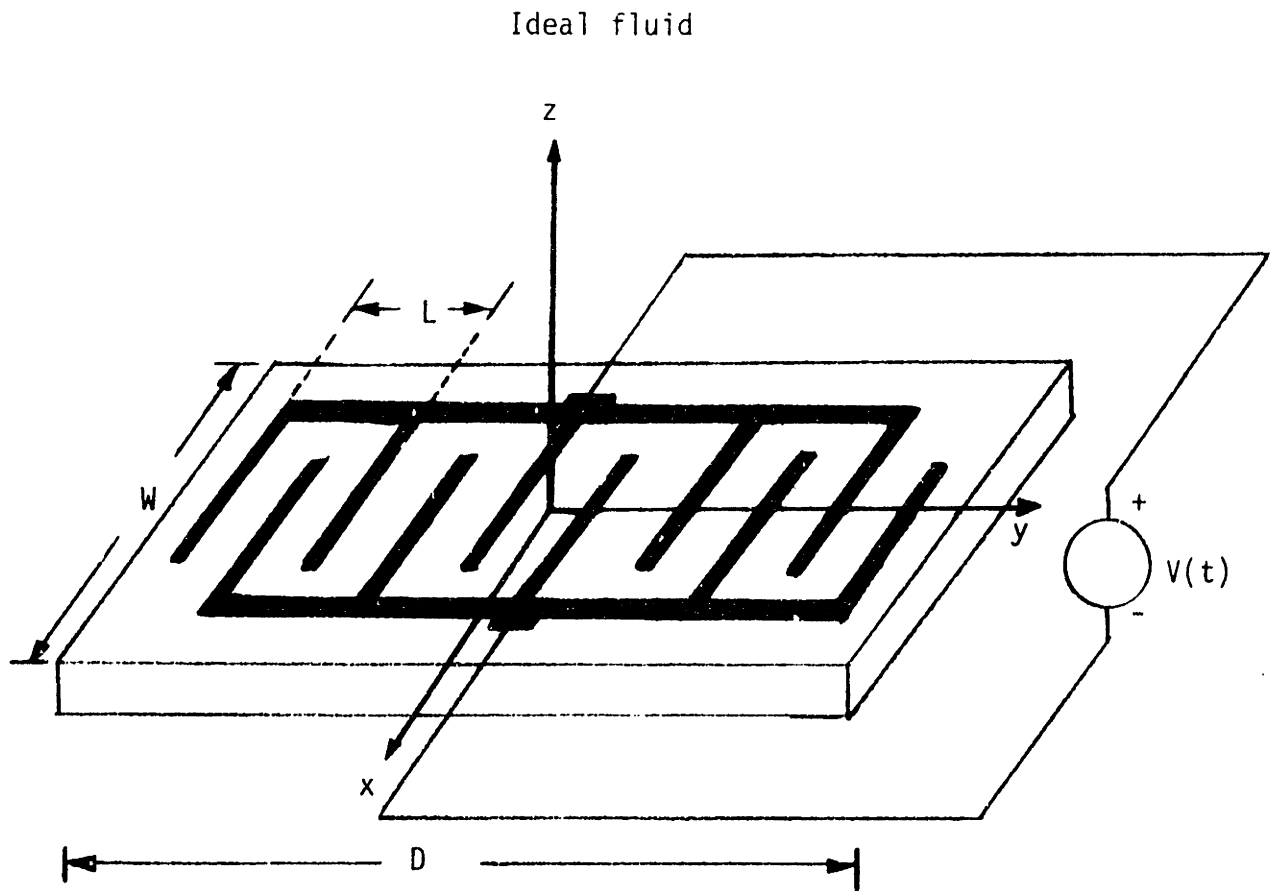
Ideal fluid

Figure 3-1.   Finite aperture transducer.

$$A(x,y) = X(x)Y(y) \quad ; \tag{3-4}$$

therefore, Eq. (3-1) becomes

$$\delta'(x,y) = \delta(y)X(x)Y(y) \quad . \tag{3-5}$$

If (3-5) is substituted into (3-3), the integrations over x and y can be performed separately,

$$\Delta'(\beta_x,\beta_y) = \left[\int_{-\infty}^{+\infty} X(x)\, e^{-j\beta_x X}dx\right]\left[\int_{-\infty}^{+\infty} \delta(y)Y(y)\, e^{-j\beta_y Y}dy\right]$$

$$= \left(\frac{1}{2\pi}\right)\hat{X}(\beta_x)\Delta(\beta_y) * \hat{Y}(\beta_y) \quad , \tag{3-6}$$

where

$$\Delta(\beta_y) * \hat{Y}(\beta_y) = \int_{-\infty}^{+\infty} \hat{Y}(\beta-\eta)\, \Delta(\eta)\, d\eta \quad , \tag{3-7}$$

$$\hat{X}(\beta_x) = \int_{-\infty}^{+\infty} X(x)\, e^{-j\beta_x X}dx \quad , \tag{3-8}$$

$$\hat{Y}(\beta_y) = \int_{-\infty}^{+\infty} Y(y)\, e^{-j\beta_y Y}dy \quad , \tag{3-9}$$

and

$$\Delta(\beta_y) = \int_{-\infty}^{+\infty} \delta(y)\, e^{-j\beta_y Y}dy \quad . \tag{3-10}$$

Using definition (3-10) and expression (2-4) developed for $\delta(y)$ in Chapter 2,

$$\Delta(\beta_y) = 2\pi \sum_{n=-\infty}^{+\infty} \Delta_n\, u_0\left(\beta_y - \frac{2\pi n}{L}\right) \quad , \tag{3-11}*$$

and substituting (3-11) into (3-6), yields the following expression for the Fourier spectrum of $\delta'(x,y)$:

---

*The function $u_0(\beta_y)$ is the Dirac delta function.

$$\Delta'(\beta_x,\beta_y) = \sum_{n=-\infty}^{-\infty} \Delta_n \hat{X}(\beta_x)\hat{Y}\left(\beta_y - \frac{2\pi n}{L}\right) \quad . \tag{3-12}$$

It is worthwhile to compare Eq. (3-12) with the two-dimensional Fourier transform, $\Delta\left(\beta_x,\beta_y\right)$, of the substrate surface deformation for the infinite plane transducer of Chapter 2. From Eq. (2-4) and definitions (3-2) and (3-3),

$$\Delta(\beta_x,\beta_y) = \sum_{n=-\infty}^{-\infty} (2\pi)^2 \Delta_n u_0(\beta_x) u_0\left(\beta_y - \frac{2\pi n}{L}\right) \tag{3-13}$$

with

$$\Delta_{-n} = - \Delta_n \quad \text{for all } n \tag{2-7}$$

and

$$\Delta = 0 \quad \text{for } n \text{ even} \quad . \tag{2-10}$$

The discrete lines in the spectrum (3-13) have been replaced in (3-12) by the Fourier transform of the aperture function, $X(x)Y(y)$. However, if the spectra $\hat{X}(\beta_x)$ and $\hat{Y}(\beta_y)$ are both narrowband compared to their periodic spacing, $\frac{4\pi}{L}$, the basic picture of the radiation field developed in Chapter 2 will also apply to the finite aperture structure. In particular, if the temporal frequency of excitation, ω, of the finite transducer is restricted to the range (2-19), radiation should result only from the terms $n = \pm 1$ in (3-12).

If we substitute the terms $n = \pm 1$ into (3-2) and recall the suppressed $e^{j\omega t}$ time dependence of $\delta'(x,y)$, we find

$$\delta'(x,y)\, e^{j\omega t\omega} = \left(\frac{1}{2\pi}\right)^2 \int_{-\infty}^{+\infty} \Delta_1 \hat{X}(\beta_x)\, \hat{Y}\left(\beta_y - \frac{2\pi n}{L}\right) e^{j(\omega t + \beta_x X + \beta_y Y)} d\beta_x d\beta_y$$

$$- \left(\frac{1}{2\pi}\right)^2 \int_{-\infty}^{+\infty} \Delta_1 \hat{X}(\beta_x)\, \hat{Y}\left(\beta_y + \frac{2\pi}{L}\right) e^{j(\omega t + \beta_x X + \beta_y Y)} d\beta_x d\beta_y \quad .$$

$$\tag{3-14}$$

From our discussion in Chapter 2 of the radiation produced by plane "boundary waves" of surface deformation, we know that acoustic radiation in the direction (ϕ_x, ϕ_y) of Fig. 3-2 would be generated by a boundary wave with the space-time dependence

$$e^{j\left(\omega t - \frac{x\omega}{c} \sin\phi - \frac{y\omega}{c} \sin\phi_y\right)} . \tag{3-15}$$

In view of (3-14) and (3-15), the angular distribution of the radiation produced by the terms $n = \pm 1$ of (3-12) is given by the normalized (amplitude) directivity function

$$D(\phi_x, \phi_y) = \left[\frac{\hat{X}\left(-\frac{\omega}{c} \sin\phi_x\right)}{\hat{X}(0)\hat{Y}(0)}\right] \left[\hat{Y}\left(-\frac{\omega}{c} \sin\phi_y - \frac{2\pi}{L}\right) - \hat{Y}\left(-\frac{\omega}{c} \sin\phi_y + \frac{2\pi}{L}\right)\right] . \tag{3-16}$$

Evidently, the new feature introduced to the transducer radiation field by finite aperture is the non-zero beamwidth of the radiation implied by Eq. (3-16).

The preceding discussion can be clarified by the following practical example. Consider the finite aperture transducer in Fig. 3-1, with width W and length D both much larger than the spatial period L of the interdigitated electrode structure. We assume the aperture function (3-4) is unity over the region occupied by the transducer and zero elsewhere; specifically,

$$X(x) = \begin{cases} 1 & \text{if } |x| < \frac{W}{2} \; ; \; W >> L \\ 0 & \text{elsewhere} \end{cases} \tag{3-17}$$

$$Y(y) = \begin{cases} 1 & \text{if } |y| < \frac{D}{2} \; ; \; D >> L \\ 0 & \text{elsewhere .} \end{cases} \tag{3-18}$$

The directivity function (3-16) becomes

$$D(\phi_x, \phi_y) = \left[\frac{\sin\psi_x}{\psi_x}\right] \left[\frac{\sin\left(\psi_y + \frac{\pi D}{L}\right)}{\left(\psi_y + \frac{\pi D}{L}\right)} - \frac{\sin\left(\psi_y - \frac{\pi D}{L}\right)}{\left(\psi_y - \frac{\pi D}{L}\right)}\right] \tag{3-19}$$
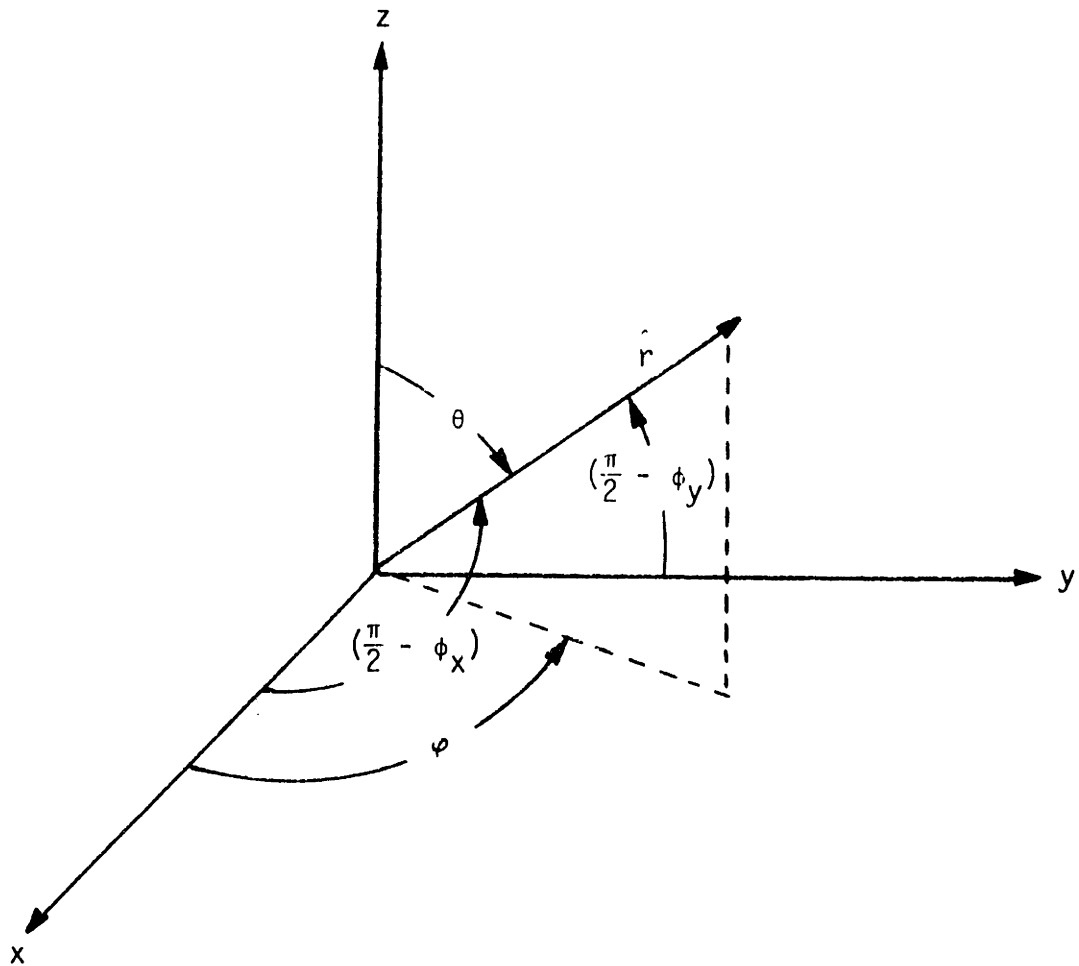
with

Figure 3-2. The direction of vector $\hat{r}$ can be specified in terms of the angles ϕ_x and $\dot{\psi}_y$. The compliments of ϕ_x and ϕ_y are respectively the angles between the x-axis and $\hat{r}$ and between the y-axis and $\hat{r}$. These angles are related to the classical spherical coordinate angles θ and φ by

$$\sin^2\theta = \sin^2\phi_x + \sin^2\phi_y$$

$$\tan\varphi = \frac{\sin\phi_y}{\sin\phi_x} .$$

$$\psi_x = \frac{\omega W}{2c} \sin\phi_x \quad , \tag{3-20}$$

$$\psi_y = \frac{\omega D}{2c} \sin\phi_y \quad . \tag{3-21}$$

Notice that the directivity function has been normalized to approximately

unity peak values, and that in agreement with Chapter 2, peak values occur

in the directions $(0, \pm \theta)$, where

$$\sin\theta = \frac{2\pi c}{L\omega} \quad . \tag{2-20}$$

The directivity function (3-19) is the product of two independent directional patterns, each involving only one angular variable. This feature is useful, because it allows us to analyze the transducer radiation by studying its dependence upon ϕ_x and ϕ_y separately.

Figure 3-3a illustrates the gross geometry of the radiation from the transducer in the XZ- plane ($\phi_y = 0$ in Fig. 3-2). In the near field, the radiation is confined to the width W of the transducer. The radiation diverges in the far field, but the radiated energy is essentially confined to the region bounded by the rays at $\pm\Delta\phi$.* Angle $\Delta\phi$ corresponds to the first zero of the $(\sin \psi_y)/\psi_y$ directivity pattern in (3-19).

The beam geometry in the YZ- plane ($\phi_x = 0$ in Fig. 3-2) is shown in Fig. 3-3b; for clarity only the beam at $+\theta$ is included. The new feature compared to Fig. 3-3a is that the angle of beam divergence, $\Delta\theta$, and the depth of the near field depend upon the center angle, θ, of the beam. It is useful to note, however, that the near field depth and the angle of far field beam divergence can be determined from the equations applying to Fig. 3-3a if the "tilted aperture", D',

---

*We divided the radiation pattern into a near field and a far field according to the geometric construction in Fig. 3-3a; however, the reader is cautioned that this method of division is not the usual convention.
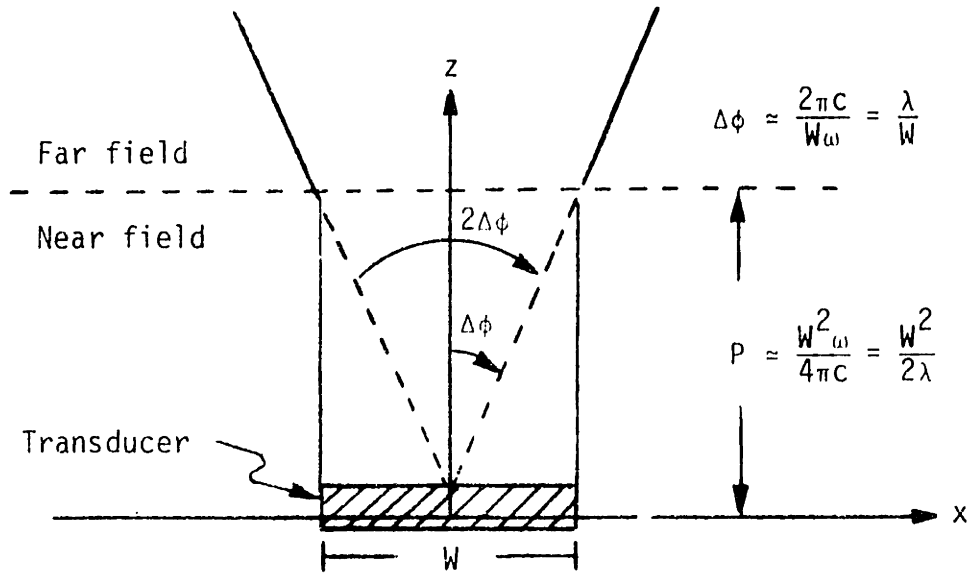
$$\Delta\phi \simeq \frac{2\pi c}{W\omega} = \frac{\lambda}{W}$$

$$P \simeq \frac{W^2\omega}{4\pi c} = \frac{W^2}{2\lambda}$$

Figure 3-3a. Beam geometry for the xz-plane ($\phi_y = 0$).

$$P \simeq \frac{D^2\omega\cos^2\theta}{4\pi c} = \frac{D^2\cos^2\theta}{2\lambda}$$

$$D' = D\cos\theta$$
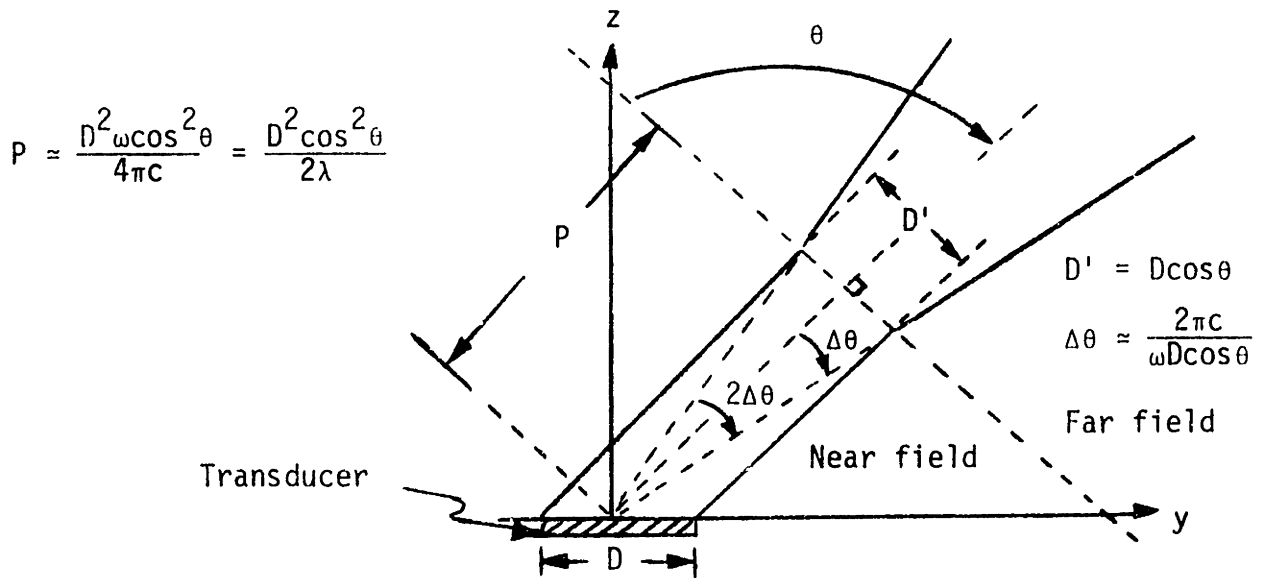
$$\Delta\theta \simeq \frac{2\pi c}{\omega D\cos\theta}$$

Figure 3-3b. Beam geometry for the yz-plane ($\phi_x = 0$). For clarity only the beam at $+\theta$ is shown.

Figure 3-3. Radiated beam geometry for the finite aperture transducer of Figure 3-1 with aperture functions (3-17) and (3-18). The angles $\Delta\phi$ and $\Delta\theta$ were calculated from (3-19) under assumption of narrow beamwidth.

$$D' = D \cos\theta \qquad\qquad (3\text{-}22)$$

is used in place of W.

The beams drawn in Fig. 3-3 use the angle of the first zero of the directivity function to define the beam edges in the far field. Alternate choices are possible; for example, the angle for which the radiation is down 3 dB from its peak value. For any such criterion, the directivity function (3-19) can be used to sketch the resultant beam geometry, which will have the same general shape as the beams shown in Fig. 3-3.

3.2 Pulsed Excitation

A transducer voltage excitation of short duration contains energy over a broad band of frequencies. Since the transducer is frequency scanned, such an excitation will produce radiation over a wide range of angles, destroying the directivity of the transducer. On the other hand, an excessively long voltage excitation is undesirable if the transducer is to be used for echo location, due to the consequent loss in range resolution. Therefore, it is advantageous to excite the transducer with a pulse having the shortest possible duration consistent with angular resolution requirements.

For a finite aperture transducer, there is a natural selection for this pulse duration, such that the loss in angular resolution due to finite pulse width just equals the loss in angular resolution due to finite transducer size. Consider the finite aperture transducer analyzed in the preceding section, with the aperture function given by the product of (3-17) and (3-18). We can determine the angular spread $d\theta$ of a radiated beam due to frequency spread $d\omega$ of the pulsed excitation by differentiating Eq. (2-20),

$$\sin\theta = \frac{2\pi c}{L\omega} \quad , \qquad\qquad (2\text{-}20)$$

yielding

$$|d\theta| = \left(\frac{2\pi c}{L\omega^2 \cos\theta}\right) |d\omega| \quad . \qquad (3\text{-}23)$$

From Fig. 3-3b, the angular spread of a radiated beam due to diffraction is

$$|d\theta| = \frac{2\pi c}{\omega D \cos\theta} \quad . \qquad (3\text{-}24)$$

Equating (3-23) and (3-24),

$$|d\omega| = \frac{L\omega}{D} \quad . \qquad (3\text{-}25)$$

A gated sinusoidal excitation of duration T and frequency $\omega_0 = \frac{2\pi c}{L \sin\theta}$, namely

$$V(t) = V_0 e^{j\omega_0 t} \left[u_{-1}\left(t + \frac{T}{2}\right) - u_{-1}\left(t - \frac{T}{2}\right) \right] \quad , \qquad (3\text{-}26)*$$

has the Fourier transform

$$\hat{V}(\omega) = T \frac{\sin(\omega-\omega_0)T/2}{(\omega-\omega_0)T/2} \quad . \qquad (3\text{-}27)$$

Observe that the Fourier spectrum (3-27) and the angular directivity function (3-19) are both of the form $\frac{\sin x}{x}$. Consistent with our definition in Section 3-1 of the angular spread, $d\theta$, of a radiated beam, we define the temporal frequency spread, $d\omega$, about center frequency ω_0 in (3-27) as the distance to the first zero of $\hat{V}(\omega)$,

$$d\omega = \frac{2\pi}{T} \quad . \qquad (3\text{-}28)$$

Using this expression in (3-25), we find

$$T = \left(\frac{D}{L}\right)\left(\frac{2\pi}{\omega_0}\right) \quad . \qquad (3\text{-}29)$$

Equation (3-29) has a strong intuitive appeal because $\left(\frac{D}{L}\right)$ is the number, N, of electrode finger pairs possessed by the finite aperture transducer of

---

*The function $u_{-1}(t)$ is the unit step function.

Fig. 3-1, and $\left(\frac{2\pi}{\omega_0}\right)$ is the duration of one cycle of the gated sinusoidal drive.

Thus, we have found that when a transducer with N finger pairs is driven by a gated sine wave N cycles in duration, the loss in angular resolution resulting from finite pulse duration is just equal to the resolution loss due to finite aperture.

3.3 Signal Return from a Distant Point Target

We have been considering the operation of the transducer as a radiator of ultrasound. By reciprocity, however, the transducer must also function as a receiver of ultrasound, and it must exhibit the same angular directivity upon reception as on transmission. Consider an acoustic plane wave "impulse" incident on the transducer from the direction θ, as shown in Fig. 3-4. The incident wave requires time

$$\tau = \frac{D \sin\theta}{c} \qquad (3-30)$$

to traverse the transducer structure. Neglecting the dynamics of the piezo-electric substrate, we expect the transducer to produce an electrical output for the time interval, τ, during which the acoustic pulse sweeps across the transducer. Using Eq. (2-20) to relate sinθ to ω in (3-30), the time interval τ may be recognized as

$$\tau = \left(\frac{D}{L}\right)\left(\frac{2\pi}{\omega}\right) = T \quad , \qquad (3-31)$$

the transmission pulse duration found earlier. Evidently, T is a characteristic time interval of the transducer for radiation in the direction θ.

By extending the preceding discussion, it is possible to argue that T is the duration of a "diffraction impulse response" of the transducer. For the transducer we have been considering, the diffraction impulse response for the reception of acoustic radiation from direction θ is a gated sine
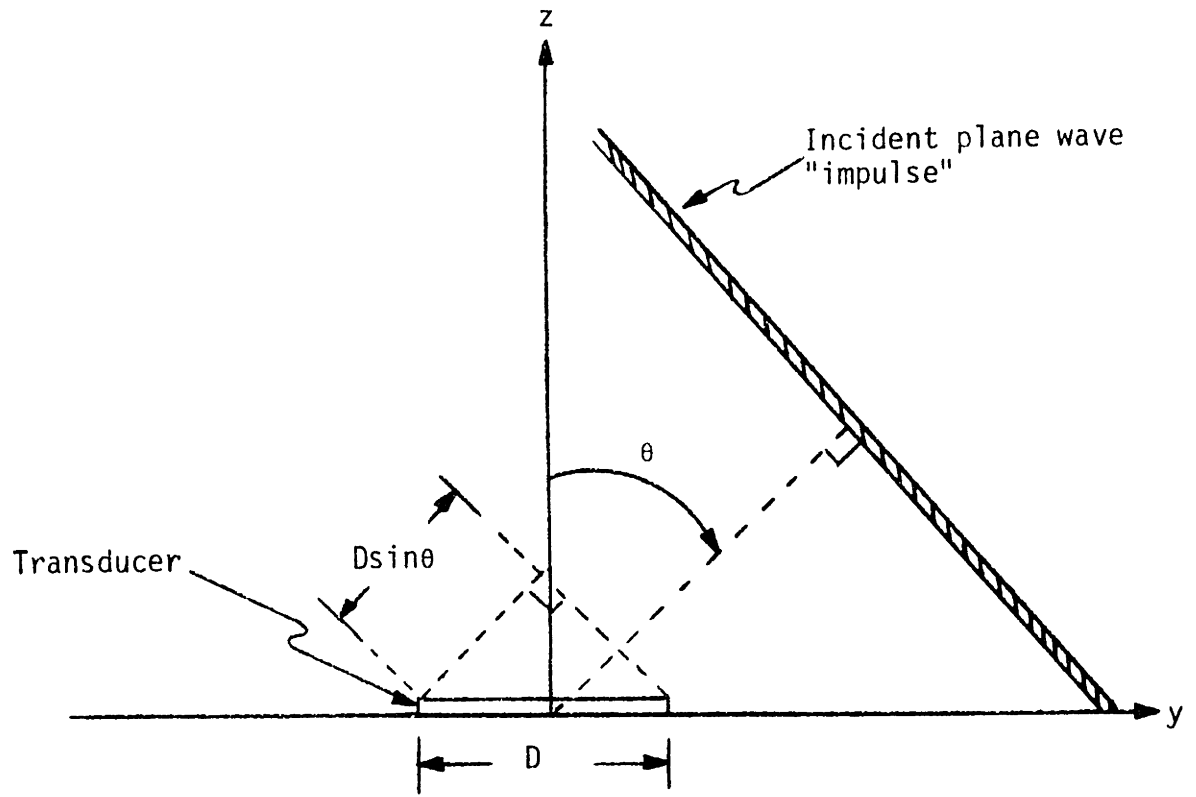
Figure 3-4. Plane wave "impulse" incident on the transducer.

wave $N \left(= \dfrac{D}{L}\right)$ cycles in duration and with center frequency

$$\omega_0 = \frac{2\pi c}{L \sin\theta} \qquad . \qquad (3\text{-}32)$$

By reciprocity, the diffraction impulse function filters both the transmitted and received acoustic radiation. Therefore, the round-trip impulse response due to diffraction is the convolution of the gated sine-wave impulse response with itself. It follows that the resulting round-trip diffraction frequency response for a single distant target in the direction θ is

$$\left|\frac{D(\omega)}{D(\omega_0)}\right| \approx \left[\frac{\sin(\omega-\omega_0)T/2}{(\omega-\omega_0)T/2}\right]^2 \qquad , \qquad (3\text{-}33)*$$

where

$$\omega_0 = \frac{2\pi c}{L \sin\theta} \qquad (3\text{-}32)$$

and

$$T = \left(\frac{2\pi D}{L\omega_0}\right) = \frac{D \sin\theta}{c} \qquad . \qquad (3\text{-}29)$$

The complex amplitude $D(\omega_0)$ depends upon the scattering characteristics of the target.

The diffraction impulse response, which we may now recognize* as the square of the directivity function of Section 3-1, is important because it allows us to determine the form of the echo from a distant target for arbitrary transducer excitation and arbitrary target direction, θ. Specifically, for the pulse excitation suggested in the beginning of this Section, the signal return from a distant point target will be a modulated sine wave with the envelope function shown in Fig. 3-5.

---

* The reader should note that (3-33) can be obtained directly from the directivity function (3-19) of the preceding Section by substituting (3-32) and (3-29) into (3-19).
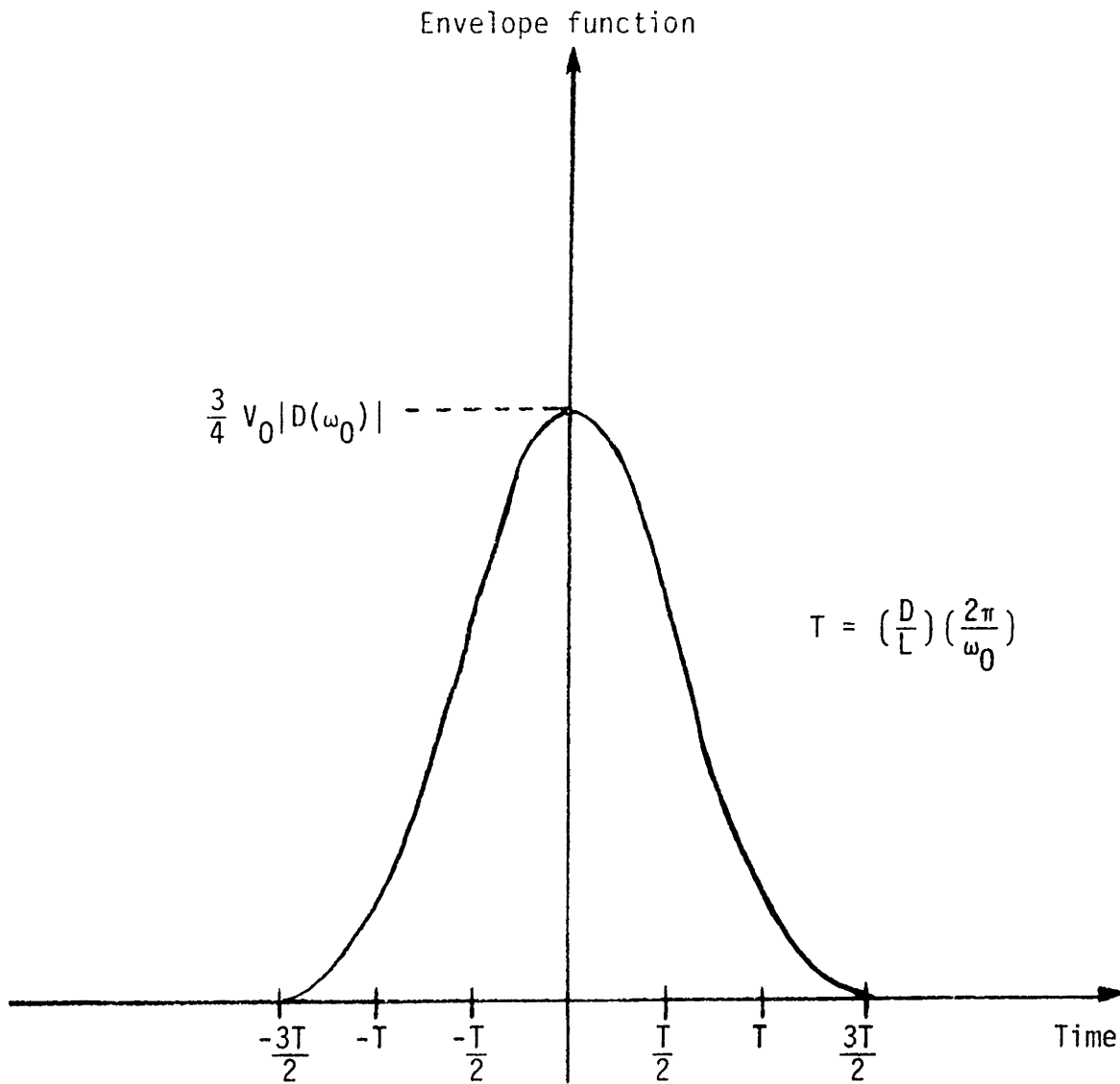
Figure 3-5. Envelope function for echo returned from a distant target in direction θ from the transducer when the transducer is excited by the pulse excitation of Eq. (3-26). The angle θ is specified in terms of ω_0 according to Eq. (3-32).

3.4 Unidirectional Radiation

In Section 2-6 we discussed a method for obtaining unidirectional radiation by modifying the prototype transducer through the use of multiple electrodes per spatial period. However, for a finite-size transducer, it is possible to achieve unidirectional radiation by a geometric construction technique.

Consider the transducer illustrated in side view in Fig. 3-6. The transducer is the finite aperture structure of Fig. 3-1, with two electrodes per spatial period; it is mounted adjacent to a perpendicular plane acoustic reflector located at y=0. As shown in Fig. 3-6, elements of acoustic radiation leaving the transducer in the $-\theta$ direction are reflected by the acoustically hard plane reflector at y=0. Thereafter, they propagate in the $+\theta$ direction as if they had come from the image transducer located to the left of the plane reflector. Thus the transducer radiates a single beam into the first quadrant in Fig. 3-6, and no radiation occurs in the second quadrant. The transducer has an apparent aperture of 2D, twice its actual value. We use this value when computing the radiated beam geometry from Fig. 3-3b of Section 3-1.*

To implement this geometric technique for unidirectional radiation, it is important that the plane reflector in Fig. 3-6 have a characteristic acoustic impedance higher than that of the fluid medium. Otherwise, the radiation elements undergo a sign reversal when reflected, producing an undesirable "dipole" beam. In practice, if the fluid medium is water, a suitable reflector might be made of brass or stainless steel, each of which

---

*The above geometric argument becomes rigorous when we observe that the boundary condition of zero normal velocity at the acoustically hard plane reflector is satisfied by assuming the image transducer shown in Fig. 3-6.
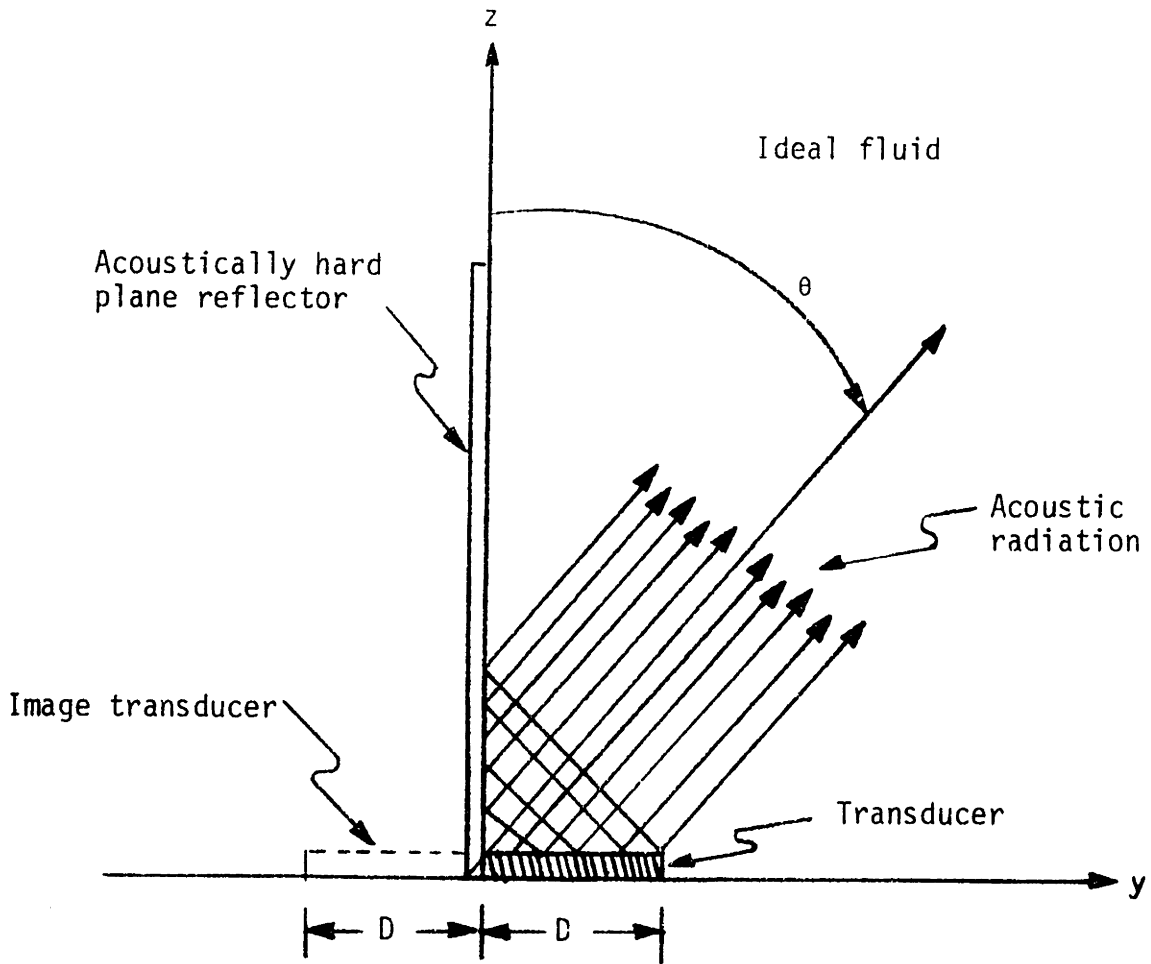
Figure 3-6. Mounting technique for finite aperture transducer to achieve unidirectional radiation (side view).

has a characteristic acoustic impedance more than twenty times greater than water.

In contrast to the geometric method in Fig. 3-6, the method of Section 2-6 for obtaining unidirectional radiation has the advantage that the radiated beam can be electronically switched from the first to the second quadrant. Nonetheless, the geometric method uses the planar electrode structure of Fig. 3-1; this electrode structure is easy to fabricate, and provides some advantages with respect to substrate dynamics, as shown in the next chapter. These are important practical advantages for the geometric technique.

Chapter 4

SUBSTRATE DYNAMICS

The purpose of this chapter is to study the dynamic motions of the transducer substrate resulting from an applied voltage excitation. The vehicle for this study will be a finite aperture thin transducer, described in the next section. We shall see that substrate motions consist of two parts, a driven response and a homogeneous or "natural" response. The driven response is that component of substrate motion considered in Chapters 2 and 3; it is described by an infinite summation identical in form to Eq. (2-11) for $\delta(y)$. The homogeneous response is determined by the boundary conditions at the edges of the finite aperture transducer; it consists of free propagating waves in the substrate, moving with a characteristic substrate wave velocity. These natural substrate waves cause a pair of spurious radiation lobes at equal, frequency-independent angles with respect to the transducer normal. Therefore, in this chapter we also discuss ways in which the homogeneous response can be eliminated or attenuated. Finally, results obtained for thin transducers will be extended qualitatively to the case of thicker transducer substrates; and a criterion will be suggested by which potentially good substrate materials may be selected.

## 4.1 Piezoelectric Coupling to the Substrate

The lack of a center of symmetry in a material is a necessary condition for the existence of piezoelectricity, so all piezoelectric materials are anisotropic.[7,16,17] Fortunately, poled ferroelectric ceramics have a readily described type of anisotropy; they possess a unique axis of polarization, but are isotropic in any plane transverse to this axis. In view
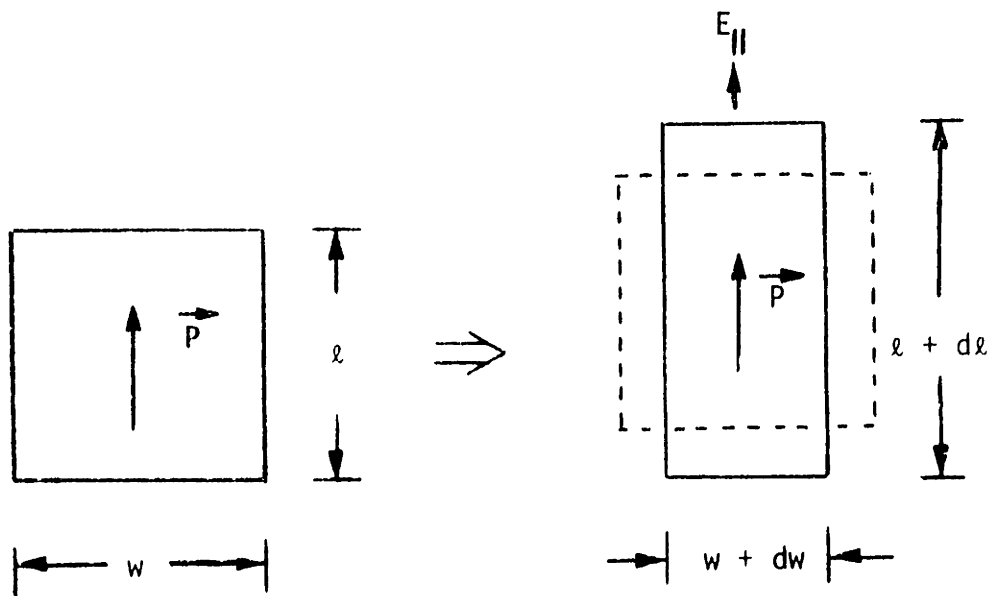
$$\frac{d\ell}{\ell} = d_{33}E_{\parallel}$$

$$\frac{dw}{w} = d_{31}E_{\parallel}$$

Figure 4-1a. Electric field applied in the direction of poling.
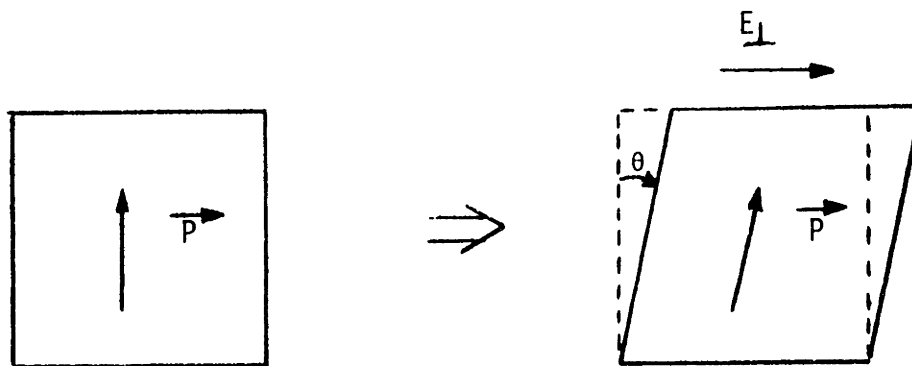
$$\theta = d_{15}E_{\perp}$$

Figure 4-1b. Electric field applied transverse to the direction of poling.

Figure 4-1. Displacement of a ferroelectric ceramic due to applied electric fields. Static conditions of constant stress are assumed; $\vec{P}$ indicates the polarization axis of the ceramic and $\vec{E}$ the direction of the electric field.

of this symmetry property, it is possible to analyze the static mechanical displacement of a ferroelectric ceramic resulting from an applied electric field by resolving the electric field vector, $\vec{E}$, into a component, $E_{||}$, parallel to the polarization axis, and a transverse component, $E_{\perp}$, as shown in Fig. 4-1. To illustrate the order of magnitude of the electromechanical coupling in ferroelectric ceramics, Table 4-1 gives the piezoelectric strain constants for PZT-5A, a material with particularly strong electromechanical coupling.*

As discussed in Section 2-4, the radiation into an inviscid fluid produced by a plane boundary is uniquely determined by the normal component of surface deformation. An inspection of Fig. 4-1 with this fact in mind suggests that a ferroelectric ceramic would be useful as a transducer substrate if it were oriented with its axis of polarization normal to the fluid boundary; that is, parallel to the z-axis of the finite aperture transducer of Fig. 3-1. Moreover, the component of electric field in the substrate most effective in generating acoustic radiation should be the z-component.

Consider a finite aperture transducer such as depicted in Fig. 3-1, fabricated using a thin ferroelectric ceramic substrate with its axis of polarization parallel to the z-axis of Fig. 3-1. According to the preceding discussion, the z-component of the substrate electric field will be the most effective component in producing radiation; but the sketch in Fig. 4-2a of the static electric field produced by an applied voltage reveals that the

---

*The notation for mechanical, electrical and piezoelectric material constants used in this report is defined in Appendix II, Eqs. (A2-1) through (A2-10); also see Ref. 18.

Table 4-1. Piezoelectric Strain Constants and Tensor
Dielectric Constants for PZT-5A*

d_{33} = 3.74 Angstrom/volt (= 10^{-10} C/N)

d_{31} = -1.71 Angstrom/volt (= 10^{-10} C/N)

d_{15} = 5.85 Angstrom/volt (= 10^{-10} C/N)

ε_{33}^{T} = 1700 ε_{0}

ε_{11}^{T} = 1730 ε_{0}

ε_{0} ... the free air dielectric constant
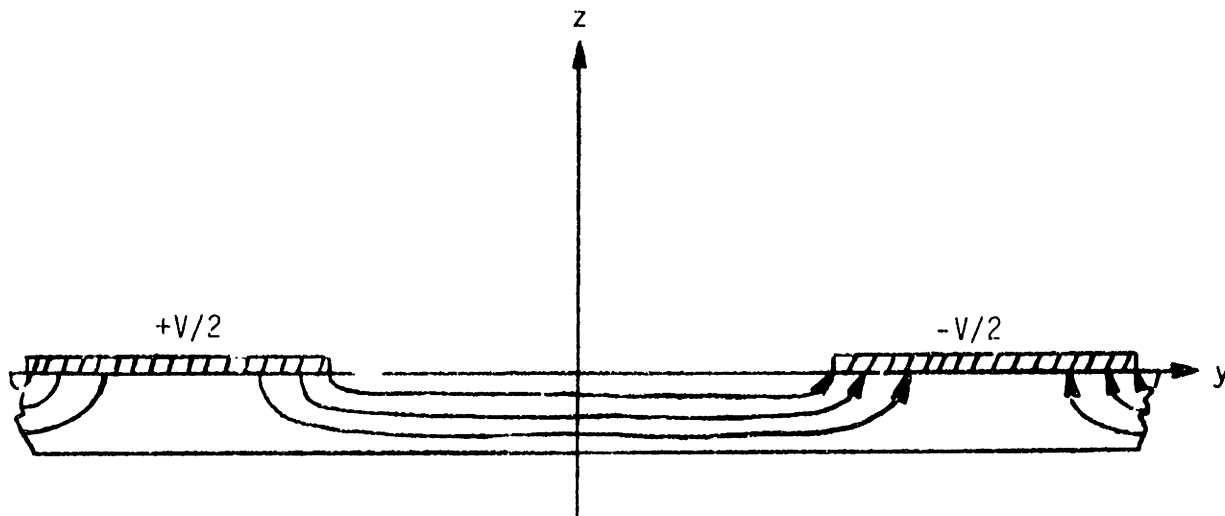
* Data from Ref. 7.

Figure 4-2a. Electric field lines for a thin ferroelectric ceramic substrate.
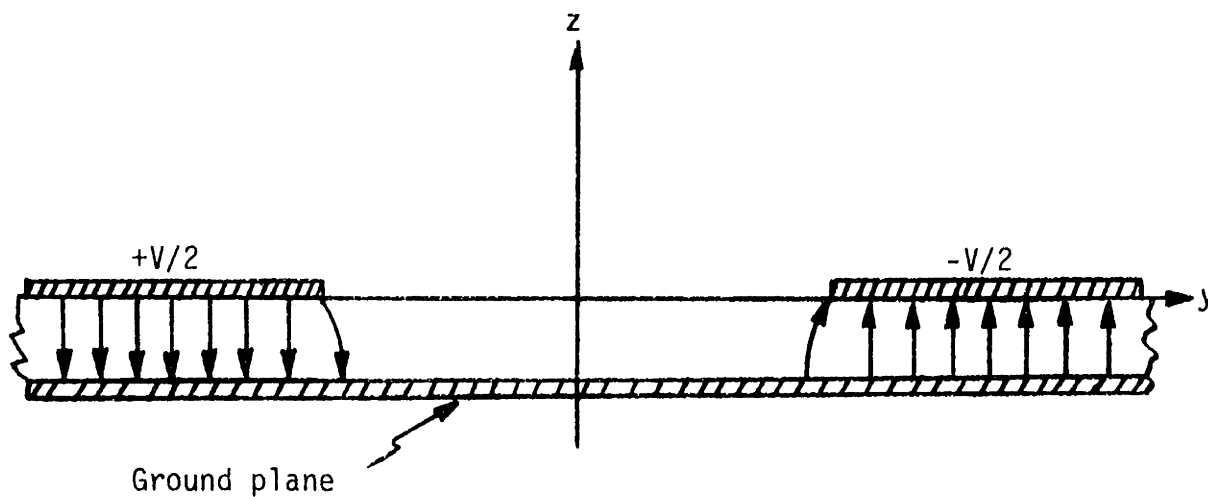

Figure 4-2b. Electric field lines for a thin ferroelectric ceramic substrate with ground plane.

Figure 4-2. A ground plane "directs" the electric field lines in the ±z-direction for efficient coupling to a ferroelectric ceramic substrate.

electrode structure of Fig. 3-1 is an inefficient generator of z-component

electric fields.*

In Fig. 4-2a, most of the electric field lines emanate from the edges

of the metal fingers, and are promptly directed transverse to the z-axis.

However, by placing a metallic ground plane on the underside of the trans-

ducer substrate, as in Fig. 4-2b, we can divert most of the electric field

lines into the ± z-direction. This technique should be effective when the

substrate thickness is thin compared to the periodic electrode spacing.

The transducer geometry of Fig. 4-2b has been suggested by an inspec-

tion of Fig. 4-1, but other plausible transducer structures also exist. For

example, strong electromechanical coupling should result for the geometry

illustrated in Fig. 4-2a, if the ferroelectric ceramic were oriented with

its axis or polarization parallel to the substrate surface; that is, along

the y-axis of Fig. 4-2a.

The general problem of deciding upon an optimal crystallographic orien-

tation for a given substrate material and transducer geometry is fairly

involved. Analytically, the procedure consists of defining a figure of

merit by which optimality can be judged, and then evaluating that figure

of merit for all possible orientations to find the best. For simple geo-

metric structures such as shown in Fig. 4-2, which use ferroelectric ceramic

substrates, symmetry considerations imply that the most effective coupling

will result when the polarization axis of the substrate is orientated along

either the y- or the z-axis. However, for crystalline substrate materials

_____

*In preparing the sketches of Fig. 4-2, it has been assumed that the
dielectric constant of the substrate is much greater than the free air
dielectric constant, ε_0. This assumption is generally true for ferro-
electric ceramics, which typically have dielectric constants greater
than 100 ε_0.[19]

with complicated symmetry properties, either experimentation or the more sophisticated techniques suggested in the literature[20,21] must be used to find the best substrate orientation.

In this report, we analyze in detail only the thin transducer illustrated in Fig. 4-2b, using a ferroelectric ceramic substrate poled in the direction of the z-axis of that figure. This section has argued that such a transducer structure and substrate orientation should provide effective electromechanical coupling between the applied transducer voltage and acoustic radiation in the fluid. Moreover, suitably polarized ferroelectric ceramic substrate materials are readily available commercially (in the form of "compressional mode transducers") for the construction of practical transducers of this type. Therefore in restricting our attention to a single type of transducer substrate material and structure, we are at least selecting a practical transducer implementation. In addition, the qualitative features of the following analysis of the substrate dynamics for that transducer are applicable to other transducer geometry and substrate material choices as well.

4.2 Detailed Analysis of Thin Transducer

The purpose of this section is to analyze the substrate dynamics of the thin transducer discussed in the preceding section. Specifically, consider the finite aperture thin transducer of Fig. 4-3, which uses a ferroelectric ceramic substrate polarized in the + z-direction and radiates into an inviscid fluid. We make the following assumptions:

1. The width W of the substrate is so great that no appreciable substrate motion takes place in the ± x-direction.

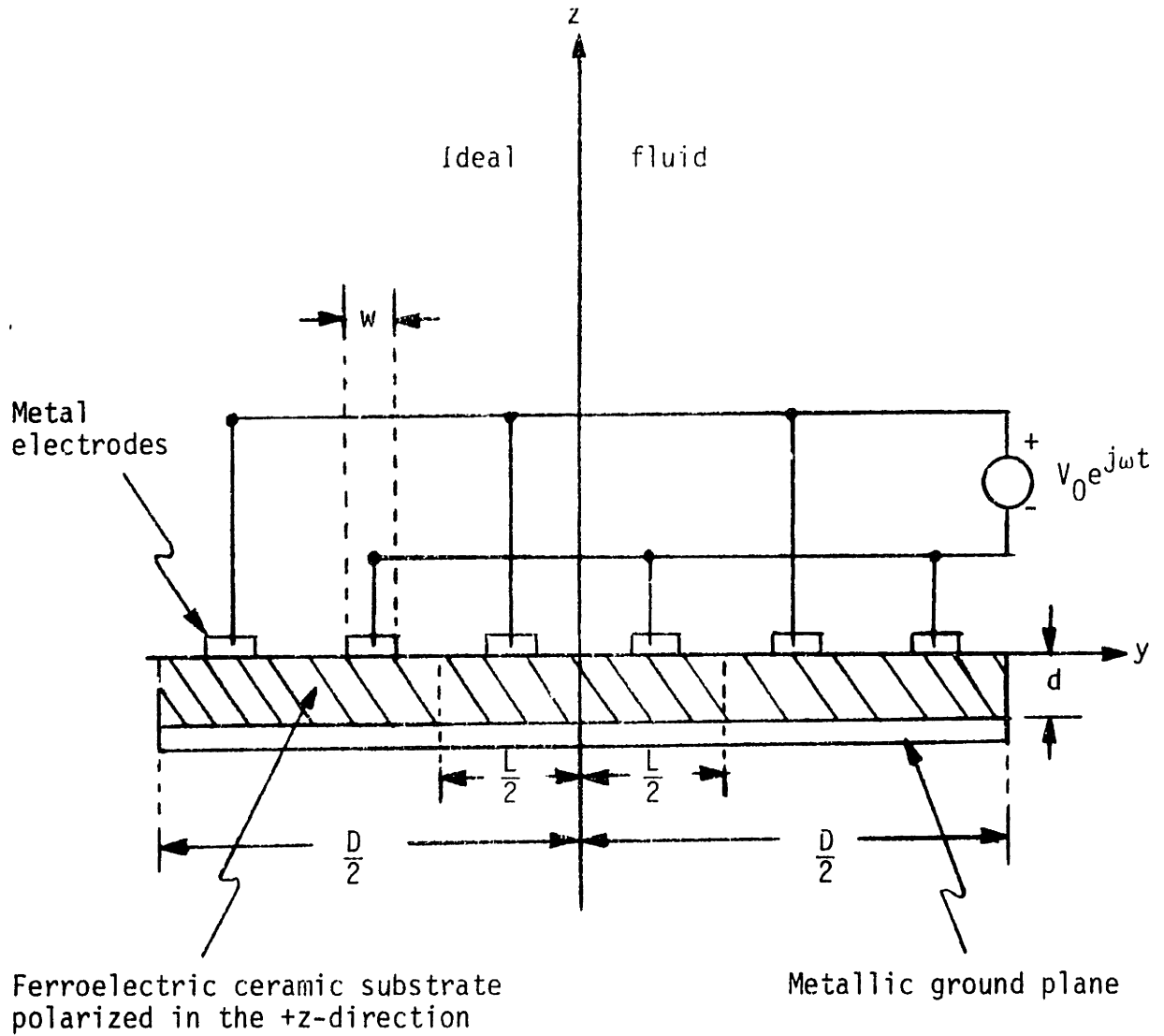2. Stress-free boundary conditions exist at the substrate edges, $y = \pm \frac{D}{2}$.

Figure 4-3. Side view of finite aperture thin transducer. The transducer extends a distance $\frac{W}{2}$ in the ±x-directions.

3. The substrate is sufficiently thin that electrical fringing fields can be neglected.

4. The transducer is so thin that mechanical stresses and strains in the substrate are independent of z.

5. The fluid is a light mechanical load for the substrate.

Assumption 5 is motivated by the observation that the characteristic acoustic impedances of ferroelectric ceramics are more than ten times greater than that of water (see the tables of material constants in Ref. 19); the stress-free boundary conditions of assumption 2 are perhaps the easiest conditions to implement in practice.

In Appendix II, we show that assumptions 1 through 5 result in the following expression for $\delta(y)$, the normal component of substrate surface deformation caused by a sinusoidal steady state voltage excitation at temporal frequency ω (see Eqs. (A2-45) through (A2-48)):

$$\delta(y) = V_0 \sum_{\substack{n=1 \\ n \text{ odd}}}^{\infty} \Delta_n \sin\left(\frac{2\pi n y}{L}\right)$$

$$+ V_0 H \sin\left(\frac{\omega y}{v}\right) \quad \text{for} \quad |y| < \frac{D}{2} \tag{4-1}$$

where

$$\Delta_n = \left[\frac{(-1)^{\left(\frac{n-1}{2}\right)} \sin\left(\frac{n\pi w}{L}\right)}{n\pi}\right] \left[\hat{d}_{33} - \hat{d}_{31} - \frac{\hat{d}_{31}\left(\frac{2\pi n}{L}\right)^2}{\left(\frac{\omega}{v}\right)^2 - \left(\frac{2\pi n}{L}\right)^2}\right] \tag{4-2}$$

$$H = \sum_{\substack{n=1 \\ n \text{ odd}}}^{\infty} \left[\frac{(-1)^{\left(\frac{n-1}{2}\right)} \sin\left(\frac{n\pi w}{L}\right)}{n\pi}\right] \left[\hat{d}_{31} + \frac{\hat{d}_{31}\left(\frac{2\pi n}{L}\right)^2}{\left(\frac{\omega}{v}\right)^2 - \left(\frac{2\pi n}{L}\right)^2}\right] \left[\frac{\sin\left(\frac{n\pi D}{L}\right)}{\sin\left(\frac{\omega D}{2v}\right)}\right] . \tag{4-3}$$

The constants w, d, D and L in these equations are geometric dimensions of the finite aperture thin transducer shown in Fig. 4-3. The other constants,

$\hat{d}_{33}$, $\hat{d}_{31}$ and ν, are functions of the substrate material constants, defined in Appendix II, and V_0 is the amplitude of the applied voltage.

4.2.1 Homogeneous Substrate Response

The right side of Eq. (4-1) for $\delta(y)$ consists of two terms. The first constitutes the driven response of the transducer substrate caused by the electric field of the interdigitated electrode structure: it is identical in form to the summation (2-11) derived and analyzed in Chapter 2. But the second term on the right side of (4-1) presents a new feature. Mathematically, this term is the homogeneous solution of the second order differential wave equation obtained in Appendix II, Eq. (A2-36); its amplitude is determined by the mechanical boundary conditions at the edges of the finite aperture transducer. If the suppressed $e^{j\omega t}$ time dependence of $\delta(y)$ is recalled, this second term can be recognized as the superposition of a pair of oppositely-directed traveling waves of substrate surface deformation, each moving with the characteristic substrate wave velocity ν. Physically, these "free" traveling waves are produced at the substrate boundaries, $y = \pm \frac{D}{2}$, as a by-product of the generation and reflection of the driven waves.

When the fluid medium into which the transducer radiates is water, it will generally be true that

$$\frac{c}{\nu} < 1 \quad , \qquad (4-4)$$

where c is the speed of sound in the fluid medium. Therefore, according to the discussion of Section 2-4, the two oppositely-directed traveling waves from the homogeneous term will produce radiation at frequency-independent angles $+ \theta_s$ and $- \theta_s$ with respect to the z axis in Fig. 4-3. The angle θ_s is determined from Eq. (2-14),

$$\sin \theta_s = \frac{c}{v} \quad . \qquad (4\text{-}5)$$

To avoid spurious radiation, we must eliminate or reduce the homogeneous component of the transducer substrate motion. There are two techniques by whicn this objective may be accomplished:

1. We can attempt to prevent the generation of homogenous substrate waves by establishing boundary conditions at the transducer edges that are satisfied by the driven substrate response alone.

2. We can attempt to restrict the homogeneous substrate waves to the immediate vicinity of the transducer edges by introducing loss mechanisms that attenuate their propagation in the substrate.

To apply the first of these methods to our case of a thin transducer with stress-free substrate boundary conditions, imagine for a moment that the transducer were an infinite plane structure. Only the driven substrate response would be present in this transducer because there are no boundaries to generate the homogeneous waves. (Alternatively, any homogeneous waves produced at infinity will have died away at infinity because of energy lost to spurious acoustic radiation.) Midway between any two adjacent electrode fingers, symmetry considerations require a zero value for T_{22}, the y-component of internal substrate stress acting on a material face normal to the y-axis.* Therefore, if the infinite transducer were cut midway between two adjacent electrode fingers, stress-free boundary conditions would be met by

---

*According to the rules for tensor transformation, the stress component T_{22} is unchanged by a 180° rotation about the z-axis. But when the z-axis is located midway between two adjacent electrode fingers, such a rotation is equivalent to inverting the sign of the electrical excitation, which must reverse the sign of T_{22} because of linearity. Together, these statements require $T_{22} = 0$.

the driven response alone and no homogeneous waves would result.* In particular, this criterion is satisfied for the thin transducer of Fig. 4-3 when its length is made an integral multiple of the interdigital period, L

$$D = NL \quad . \tag{4-6}$$

Substituting (4-6) into (4-3) makes

$$\sin\left(\frac{\pi nD}{L}\right) = 0 \quad \text{for all } n \quad , \tag{4-7}$$

thereby verifying that the homogeneous term in (4-1) is eliminated.

In practice, we cannot expect perfect elimination of the homogeneous substrate response solely due to the optimal placement of transducer boundaries. For example, any asymmetry of the transducer introduced during its fabrication would invalidate the precise stress cancellation midway between adjacent electrodes. Indeed, no cancellation at all would occur for the unidirectional transducers described in Section 2-6, which have intentionally asymmetrical electrical excitations. Therefore, it is advisable to utilize as well the second method for eliminating the homogeneous substrate waves produced at the transducer boundaries.

This second method could involve coating the entire back face of the transducer with a suitable acoustic energy absorbing material, a technique successfully applied to thickness-mode transducers.[6] Since the homogeneous waves are produced only at the substrate edges, such a procedure should cause them to decay exponentially with distance away from the transducer boundaries. But because the transducer driven response is generated

---

* This conclusion is strictly valid only if the electric field in the substrate is undisturbed by the cut, which is the case for a thin transducer under the approximation of no electrical fringing (see Fig. 4-2b).

throughout the substrate by the electric field, its amplitude will remain constant across the transducer, though somewhat reduced by the introduction of the substrate loss.

Since substrate loss restricts the homogeneous waves to the vicinity of the transducer edges, while the driven response extends over the entire radiating area, the amplitude of the spurious lobes will be reduced in comparison with the driven lobes. Extending this technique, the transducer radiating surface could also be coated near its edges with the lossy, energy absorbing material to increase the rate of the exponential decay of the homogeneous waves. This lossy coating may have the additional benefit of shielding the fluid from the localized region of the transducer surface where the homogeneous waves are most intense, further reducing the spurious radiation lobes.

One final comment about the homogeneous component of the substrate response concerns the denominator resonance factor in (4-3), $\sin\left(\frac{\omega D}{2v}\right)$. Physically, the resonances predicted by this factor result from homogeneous waves that are generated at one transducer boundary, travel across the transducer, reflect from the opposite boundary and then travel back across the transducer to arrive in phase at the original boundary. These resonances will obviously be highly damped by even quite small substrate propagation losses. Therefore, for a practical transducer in which loss mechanisms have been deliberately introduced, this resonance factor should be replaced by unity in Eq. (4-3).

4.2.2 Driven Substrate Response

Having thus considered the physical implications of the homogeneous component of the transducer substrate motion, and various means to eliminate

or reduce the spurious radiation from it, we shall ignore this term for the remainder of the section and concentrate instead on the driven substrate response. In particular, we are interested in the first term of the infinite summation in (4-1), because according to the discussions in Chapter 2, the temporal frequency, ω, of the transducer excitation will be restricted to a range over which only the acoustic radiation from this term can propagate.

In Chapter 2, the upper limit of the frequency range over which only the first term of the driven response can propagate was determined by the radiation cutoff frequency, $\frac{6\pi c}{L}$, of the third term of the driven response (see discussion leading to (2-18)). However, notice that the third spatial harmonic in (4-2) vanishes when the transducer finger width w is given by

$$w = \frac{L}{3} \quad . \tag{4-8}$$

With this specification for the electrode finger width, the upper limit of the frequency range over which only the first term of the driven response radiates will be determined by the cutoff frequency of the fifth term in the infinite summation in (4-1). Using Eq. (2-18), this frequency range becomes

$$\frac{2\pi c}{L} < \omega < \frac{10\pi c}{L} \quad . \tag{4-9}$$

From (2-20), the angular range corresponding to frequency range (4-9) is

$$90° > |\theta| > \sin^{-1}\left(\frac{1}{5}\right) \approx 11.5° \quad . \tag{4-10}$$

The finger width specified in (4-8) eliminates the third spatial harmonic of the electric field in the case of the thin transducer, for which electrical fringing is negligible. The consequence of fringing fields is to increase the effective width of the electrode fingers, so for thicker transducers the actual electrode width should be somewhat less than

specified in (4-8). It is shown in the literature[22] that the third spatial harmonic of the static electric field from an interdigitated electrode structure on an infinitely thick substrate (half space) is eliminated when

$$w = \frac{L}{4} \quad . \tag{4-11}$$

From the standpoint of electrical fringing, the breakpoint between thick and thin transducer substrates is

$$d < \frac{L}{2\pi}\sqrt{\frac{\varepsilon_{33}}{\varepsilon_{11}}} \quad , \quad \text{thin substrate;}$$

$$\tag{4-12}$$

$$d > \frac{L}{2\pi}\sqrt{\frac{\varepsilon_{33}}{\varepsilon_{11}}} \quad , \quad \text{thick substrate;}$$

where ε_{11} and ε_{33} are the substrate tensor dielectric constants. This criterion follows from the analysis in Ref. 22.

At first glance, the 8° increase in angular range (4-10) compared to the angular range (2-23) found in Chapter 2 may seem a trivial improvement. On the contrary, this increase may be quite useful for some applications, such as discussed in Section 1.1. The range resolution of an echo-location system using the transducer will be proportional to the characteristic time T discussed in Chapter 3, but from Eq. (3-30), T is proportional to sinθ, where θ is the direction of acoustic radiation. Consequently, frequency range (4-9) allows a 41% improvement in the best achievable range resolution compared to the best value possible over the frequency range (2-23).

If (4-8) is used to specify the electrode finger width w, Chapters 2, 3 and 4 have discussed criteria for the selection of all dimensions of the thin transducer with the exception of its thickness d. From Eqs. (4-1) to (4-3), we see that $\delta(y)$, and therefore the amplitude of the acoustic

radiation from the transducer, is independent of transducer thickness. At the same time, both the shunt capacitance, C_0, and the Q of the transducer driven response (determined from the energy loss due to acoustic radiation) are inversely proportional to transducer thickness.* Apparently, the thickness of the thin transducer should be made as great as possible; but beyond a certain thickness, which depends on the specific substrate material used, the thin transducer assumptions 3 and 4 from the beginning of this section cease to apply. Continued increase in transducer thickness no longer brings improvement, and in fact may result in some loss in performance.

4.3 Thick Transducers

In the preceding section we saw that the substrate motion of a thin transducer is the superposition of a driven response and a homogeneous response, and that the homogeneous response consists of free propagating waves moving with a characteristic substrate wave velocity. Furthermore, it is apparent from Eq. (4-2) that a resonance occurs in the driven response when the homogeneous wavenumber $\frac{\omega}{v}$ equals the wavenumber $\frac{2\pi}{L}$ of the first term of the driven response. (In fact a resonance occurs in (4-2) for each wavenumber $\frac{2\pi n}{L}$, but when the temporal frequency of excitation is so restricted that only the first term of the driven response can propagate, only the resonance of the first term will be observed.)

For thick transducers, the substrate motion again consists of a driven response and a homogeneous response, but while only one type of homogeneous

---

* Expressions for Q and the shunt capacitance, C_0, for a thin transducer are obtained in Appendix II. The shunt capacitance is the electrical capacitance that would be measured across the transducer terminals if the substrate could be clamped to prevent any lateral movement. This capacitance appears in parallel with any electrical loading resulting from actual substrate motions and subsequent acoustic radiation.

wave exists in thin transducers*, thick transducers may possess several propagating wave modes. In general, all natural wave modes of a thick transducer are excited at the substrate edges as by-products of the generation and reflection of the driven waves. Each mode therefore contributes a term to the homogeneous response of the substrate motion and results in a spurious radiation lobe. Each wave mode also accounts for a resonance in the driven response at the frequency for which its wavenumber equals the wavenumber $\frac{2\pi}{L}$ of the first term of the driven response.

A discussion of the multiple propagating wave modes in non-piezoelectric plates is presented in Ref. 23. From that discussion, we may surmise the following behavior for the wave modes in a transducer substrate.

1. The number of propagating wave modes in a substrate depends upon the product of the temporal frequency, ω, and the substrate thickness, d. For very low frequencies or very thin substrates, only two propagating wave modes exist; namely the mode discussed in Section 4-2.1, which is the extensional wave of Ref. 23, and a flexural wave (see footnote below).

2. For high frequencies or thick substrates, the flexural and extensional waves merge to form a surface wave, and additional wave modes appear. For a fixed temporal frequency, the number of additional propagating wave modes increases with increasing substrate thickness. For a fixed substrate thickness, each new wave mode has a cutoff frequency below

---

* It is not strictly true that only one homogeneous wave mode exists in thin transducers because a flexural wave can also occur (see Ref. 23). However, the flexural wave velocity is proportional to the square root of the substrate thickness, and for a very thin transducer the flexural wave will be too slow to radiate. In addition the flexural wave is poorly coupled to the z-component electric field of the thin transducer of Fig. 4-3, and will therefore be weakly excited, even at resonance.

which it cannot propagate. The various new wave modes are indexed in order of increasing cutoff frequency.

3. The phase velocity for a given mode is infinite at its cutoff frequency, but quickly decreases with increasing frequency and finally approaches a limiting value. This limiting value is characteristic of the particular mode, but is usually slightly faster than the material surface wave velocity.

The high order wave modes in thick substrates are analogous to the wave modes in a rectangular electromagnetic waveguide. Waves are reflected back and forth between the substrate surfaces as they propagate from one transducer edge to the other. In the rectangular electromagnetic waveguide, these wave modes cannot exist unless the waveguide height and width are each greater than one-half wavelength. By analogy, when the transducer substrate is oriented with its polarization axis parallel with the transducer normal, as in Fig. 4-3, the first high order substrate wave mode should result when the substrate thickness is approximately one-half wavelength for a compressional wave propagating in the thickness direction. This observation implies an upper limit on the substrate thickness for a thin transducer, because it suggests that thin transducer assumptions hold only so long as the substrate is less than one-half wavelength thick over the operating frequency range of the transducer.

One motive for considering thick transducers was presented at the conclusion of Section 4.2.2, where it was pointed out that improved performance results for a thin transducer as its thickness increases, at least to the point where the thin transducer assumptions break down. However, another motive for considering thick transducers is provided by their multiple resonances. These resonances may be advantageous if they can be strategically distributed through the transducer operating frequency range by careful

selection of the substrate thickness. By analogy with the radio engineering technique of stagger-tuning IF sections, such a procedure could result in strong electromechanical coupling over a broad angular range of transducer operation.

It was mentioned that each new substrate wave mode will contribute a component to the homogeneous response of the substrate motion, which will generate a spurious radiation lobe. From the earlier description of the variation of phase velocity with frequency, the spurious radiation lobe due to a high order substrate wave mode will be directed normal to the transducer surface ($\theta = 0$) when it first appears at the cutoff frequency of the mode. With increasing temporal frequency of excitation, the spurious lobe will quickly sweep through the transducer radiation field and then assymptotically approach a limiting direction, determined from the limiting phase velocity of the mode. This sudden appearance and subsequent steering with increasing frequency of the spurious radiation from a high order mode contrasts with the fixed location of the spurious lobe of the thin transducer. Clearly the spurious radiation of a high order mode is more injurious to the performance of the transducer than the single, fixed lobe of the thin transducer. Substantial damping of a thick transducer, along the lines discussed in Section 4.2.1 is therefore extremely important. This damping should also have the advantage of reducing the Q of the "staggered" resonances of the driven response discussed earlier, and should therefore smooth the transducer frequency response.

While many propagating modes exist in a very thick transducer, it is likely that strong electromechanical coupling will result with only a few modes. For example, in the limiting case of an infinitely thick transducer, the only candidate for resonant coupling is the surface wave. Moreover, it

is unlikely that significant damping of high order modes in a thick transducer could be achieved by the technique of coating the back surface of the transducer with lossy material as discussed in Section 4.2.1, because much of the energy in the high order modes will be concentrated inside the substrate. Therefore, if the transducer thickness is to be increased beyond the thin-transducer thickness limit in order to take advantage of the "stagger-tuning" of multiple substrate resonances, the transducer substrate should be made only thick enough to allow a very few modes in addition to the fundamental flexural and extensional modes of the thin transducer.

The mathematical analysis of the high order wave modes in piezoelectric substrates is very complicated, so the optimum thickness for any particular substrate material and transducer geometry is probably best determined experimentally using the qualitative discussion of this section as a guide. Fortunately, such an experimental study need only be conducted once for any particular combination of substrate material and transducer geometry, because the results can be scaled to arbitrary frequency ranges.

4.4 Electromechanical Coupling Factors

A great number of ferroelectric ceramic materials are available for use as transducer substrates, and when consideration is extended to crystalline piezoelectric materials as well, the number grows even greater.[7,19] A simple criterion for comparing the potential value of such materials as transducer substrates is clearly desirable, but even for the well-known case of compressional mode transducers, no single figure of merit seems to fully characterize a material for use as a transducer. However, experience has shown that materials of widely differing symmetry and material properties can be approximately compared in terms of their electromechanical coupling factors.[7,19,24]

The electromechanical coupling factor of a piezoelectric material is a function of both its material constants and the particular mode of mechanical vibration being considered; thus a material possesses not one, but many coupling factors. The coupling factor for a particular mode of vibration is a measure of the strength of the piezoelectric coupling to that mode provided by the material. The coupling factor is a dimensionless number between zero and unity; a value of zero indicates no piezoelectric coupling, and a value of unity perfect coupling. Ferroelectric ceramics generally possess the strongest electromechanical coupling factors, which exceed 0.7 for some vibration modes in strong-coupling materials such as PZT-5A. By comparison, coupling factors for quartz are typically less than 0.1.

For the extensional mode of vibration of the thin transducer in Fig. 4-3, the proper electromechanical coupling factor is k_{31}' (see chart on pp. 194-5 of Ref. 7). This material parameter is rarely tabulated, but it can be related to the generally available coupling factor k_{31} by

$$k_{31}' = \frac{k_{31}}{\sqrt{1 - k_{31}^2}} \sqrt{\frac{1 + \sigma^E}{1 - \sigma^E}} \approx \frac{1.36 \, k_{31}}{\sqrt{1 - k_{31}^2}} \quad . \qquad (4\text{-}13)^*$$

According to the analogy in Section 4.3, the high order substrate modes consist of waves reflecting back and forth between the transducer surfaces as they propagate from one transducer edge to the other. Therefore, intuition suggests that the compressional mode coupling factor k_{33} should indicate the relative strength of the electromechanical coupling to the first few high order substrate modes.

---

* Poisson's ratio for ferroelectric ceramics is typically[25]

$$0.28 < \sigma^E = -\frac{s_{12}^E}{s_{11}^E} < 0.32 \quad .$$

The available bandwidth of the electromechanical coupling to a particular vibration mode is approximately proportional to the material coupling factor.[7,26] Since the transducers considered in this report operate over a fairly broad band of frequencies, the coupling factors can be used to establish an approximate ordering of potentially desirable materials. For example, when the coupling factors of two potential substrate materials differ by a factor of three or more, the weak-coupling material should probably be rejected in favor of the strong-coupling material. However, when material coupling factors are comparable, other considerations such as characteristic acoustic impedance, material Q and the nature of spurious vibrational modes must strongly influence the material choice.

It should be emphasized that the analysis in Chapter 2, as well as the explicit solution for the thin transducer in Section 4.2, demonstrate that virtually any piezoelectric material will serve to some degree as a transducer substrate. The purpose of this section has been to provide a simple guideline for the preliminary selection of potentially superior substrate materials. Due to the variety of strong-coupling materials available, several good substrate materials likely exist. In the final analysis, a program of experimentation is probably the best way to select the substrate material for any particular application.

Chapter 5

EXPERIMENTAL DATA

This chapter reports the results of an experimental program involving the fabrication and testing of several transducers of the type described in Chapters 2 through 4. The most important demonstration of the experimental program is that the transducers indeed produce narrow beams of ultrasonic radiation that are electronically steered by varying their temporal frequency of excitation. In addition the program confirms various other aspects of transducer performance predicted theoretically in the preceding chapters. For example, we examine the sensitivity of the transducers as a function of frequency and verify that a single resonance is found in thin transducers, while multiple resonances occur in thick transducers. We also briefly examine the spurious radiation lobes in both thin and thick transducers caused by their homogeneous substrate responses.

This chapter begins by describing the experimental transducers to be studied in the remainder of the chapter and by diagramming the apparatus used in the testing procedure. Next we derive an explicit relation between the experimental measurements and the far-field acoustic intensity produced by the transducer. Finally, we present a summary of experimental results.

5.1 Experimental Transducers

Four experimental transducers are studied in detail in this chapter. Two of these transducers use PZT-5A as a substrate material and two use lead metaniobate; each substrate is poled in the thickness direction as discussed in Chapter 4. The PZT-5A substrate material was purchased from

Valpey-Fisher Corporation, Holliston, Massachusetts, in the form of thickness-mode transducers, and the lead metaniobate was similarly obtained from Keramos Incorporated, Lizton, Indiana. (Lead metaniobate is the Keramos material K-81.) In most cases, the materials were ordered as disc transducers in which the diameter and thickness (or the thickness-mode series resonant frequency) were specified. The rectangular substrate sections required for transducer fabrication (see Fig. 5-1) were cut from the disc transducers with a wire saw.

For each substrate material, one thin and one thick transducer is considered. In all cases the periodic transducer electrode spacing is such that a frequency of 2.5 MHz corresponds to radiation at 45° from the substrate normal according to Eq. (2-20). Figure 5-1 presents a sketch of the transducers and Table 5-1 lists the dimensions of the devices; the four transducers are referred to as A, B, C and D. Important constants of the two substrate materials are provided in Table 5-2. Photographs of a thin transducer, such as transducers A and C, appear in Fig. 5-2, and photographs of a thick transducer, similar to transducers B and D, are presented in Fig. 5-3.

The transducers were fabricated by the Microelectronics Group at the MIT Lincoln Laboratory using standard photolithographic techniques. A chrome-gold metal film was deposited upon the two surfaces of a ferroelectric ceramic substrate and coated with photo-resist. The resist was exposed on one side through a mask of the interdigitated electrode structure and on the reverse side through a mask of the ground plane. Next the gold film was selectively etched, leaving the interdigitated electrode pattern on one substrate surface and the ground plane on the other. Finally, the gold was electroplated to a thickness of one-to-three microns.
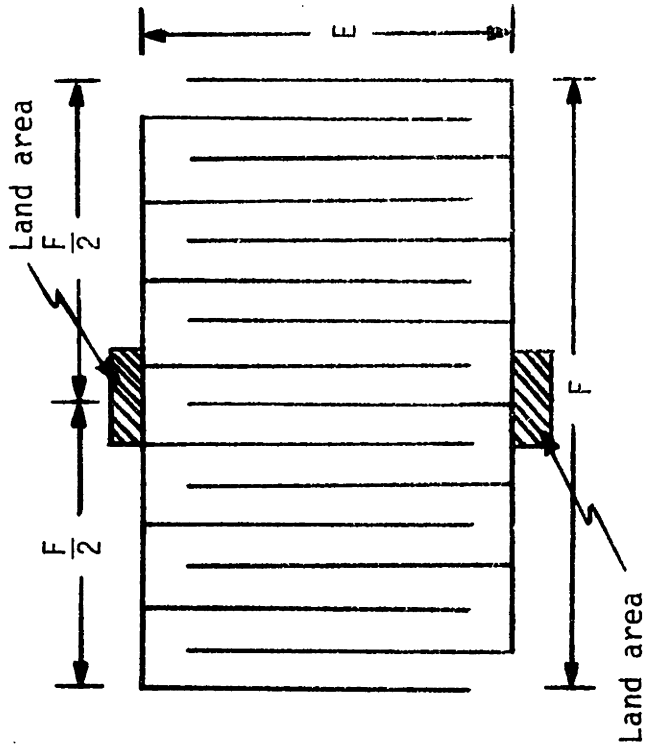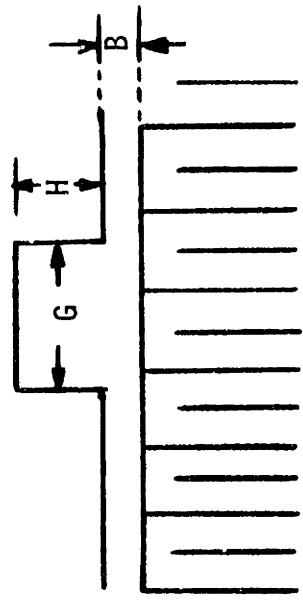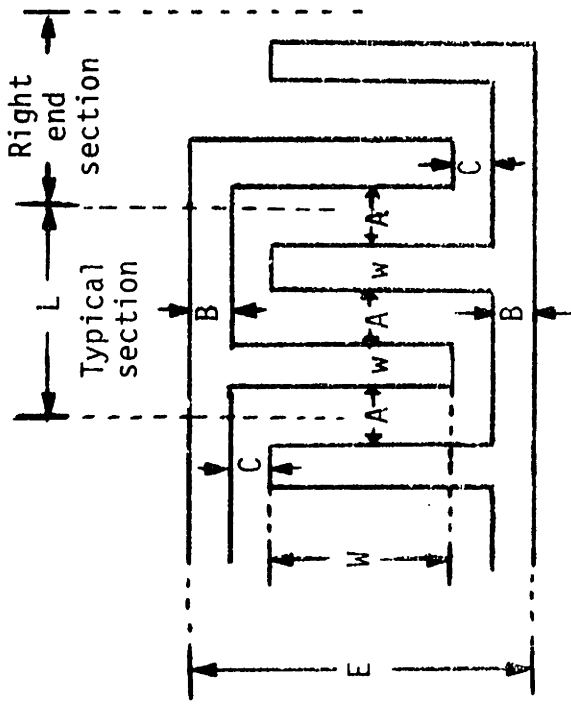
Figure 5-1b. Exploded view of typical section.

Figure 5-1d. Ground-plane metalization pattern
for back face of transducer.

Figure 5-1a. Overview of interdigitated
electrode structure.

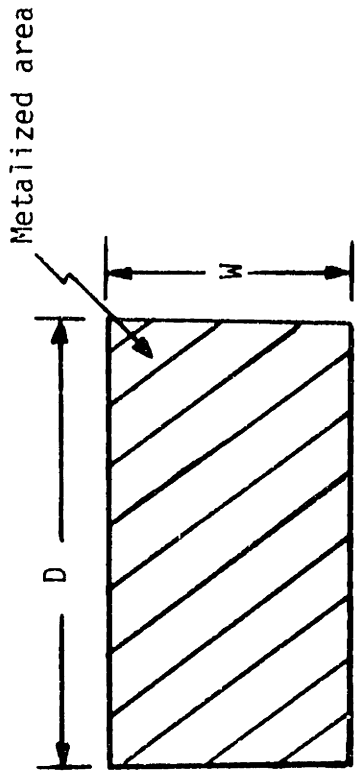Figure 5-1c. Exploded view of land area.

Figure 5-1. Sketch of transducer electrode patterns for front and back substrate surfaces. Dimensions
for the experimental transducers are specified in Table 5-1.

Table 5-1. Dimensions for experimental transducers*.

Substrate Specifications:

	Transducer A	Transducer B	Transducer C	Transducer D
material	PZT-5A	PZT-5A	Lead metaniobate	Lead metaniobate
length (inches)	0.675	0.675	0.675	0.675
width (inches)	0.550	0.360	0.550	0.360
thickness (inches)	0.005	0.026	0.007	0.021
compressional mode series resonant frequency (MHz)	16.8	3.25	10.25	3.5

Electrode-Pattern Dimensions (inches) for Fig. 5-1:

	Transducer A	Transducer B	Transducer C	Transducer D
L	0.033	0.033	0.033	0.033
w	0.0055	0.00825	0.0055	0.00825
W	0.315	0.315	0.315	0.315
D	0.510	0.350	0.510	0.350
A	0.011	0.00825	0.011	0.00825
B	0.0395	0.04	0.0395	0.04
C	0.07875	0.05	0.07875	0.05
E	0.5515	0.495	0.5515	0.495
F	0.495	0.495	0.495	0.495
G	0.118	0.100	0.118	0.100
H	0.07875	0.06	0.07875	0.06

* Thin transducers A and C have the same dimensions (except for thickness); similarly, thick transducers B and D have the same dimensions (except for thickness).

Table 5-2. Important substrate material properties.*

Electromechanical Coupling Factors:

	PZT-5A	Lead Metaniobate
K_{31}'	0.527	0.06
K_{33}	0.705	0.38

Intrinsic Mechanical Quality Factor:

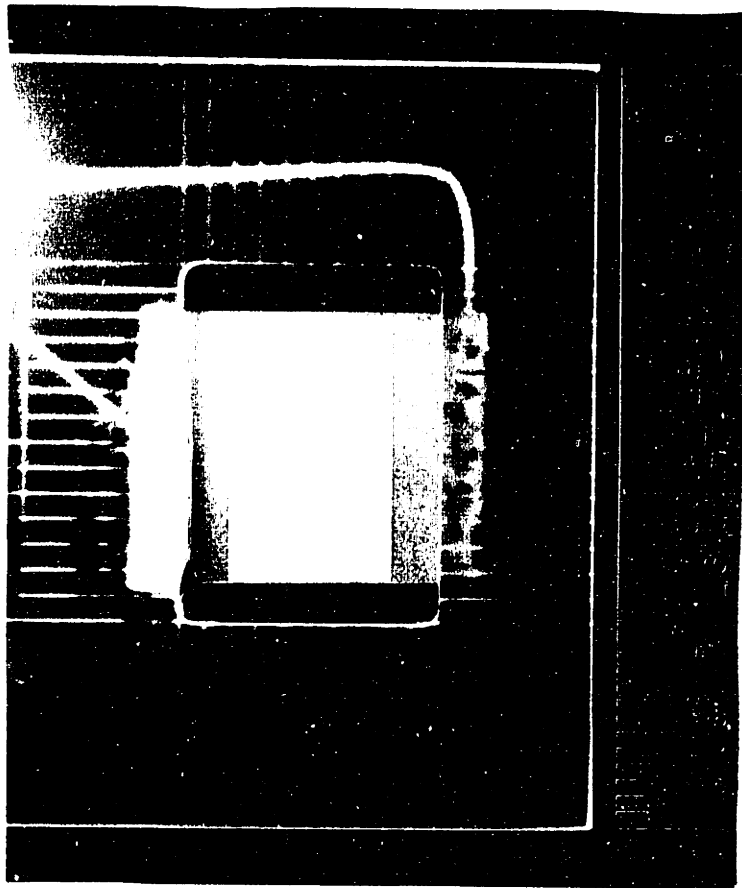|	PZT-5A	Lead Metaniobate
Q_m	75	10

* Data from Ref. 7.

Figure 5-2b. Back face.
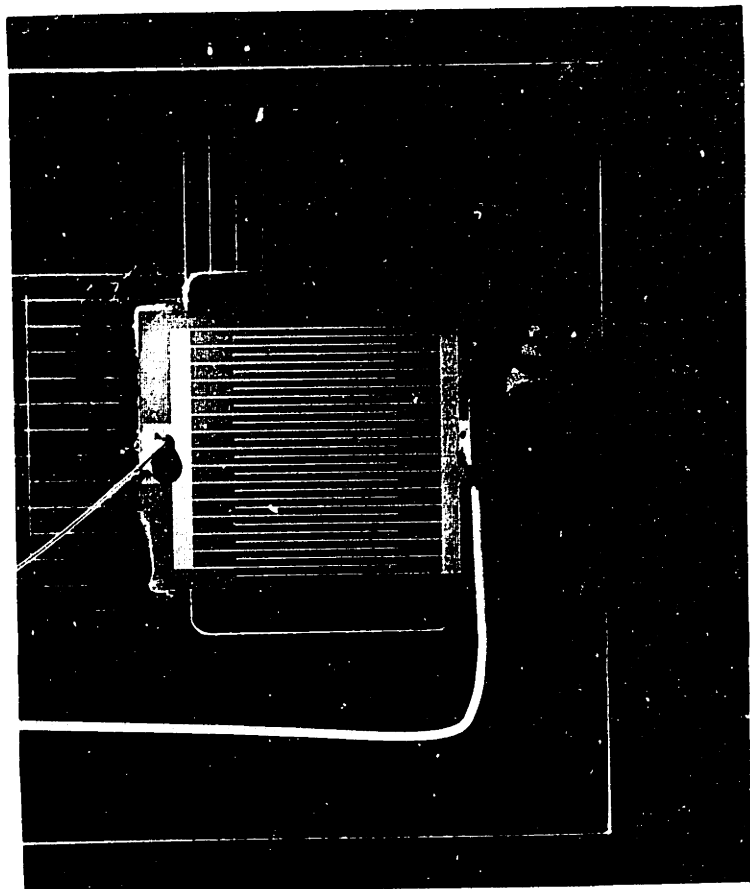
Figure 5-2a. Front face.
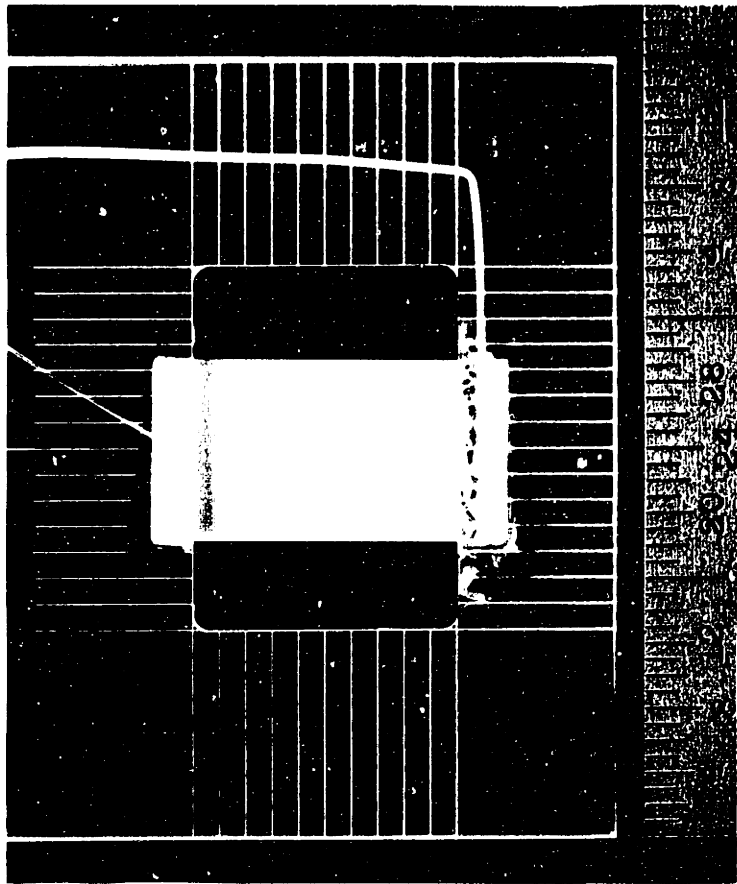
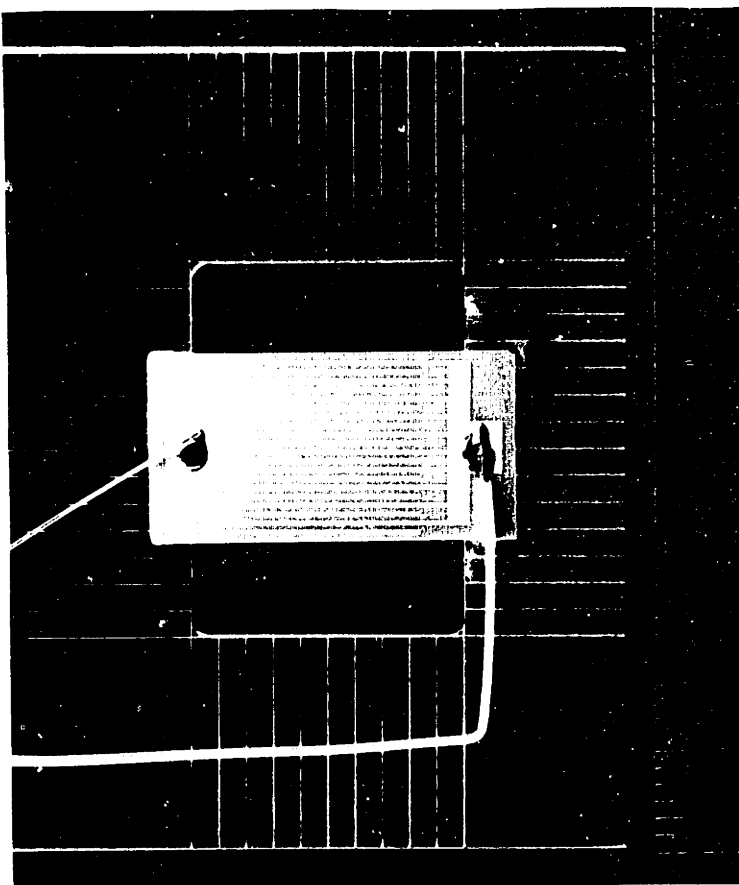Figure 5-2. Photographs of a thin transducer.

Figure 5-3a.   Front face.

Figure 5-3b.   Back face.

Figure 5-3.   Photographs of a thick transducer.

Since both the ground plane and the interdigitated electrode structure
are planar, having no need for one electrode to cross over another, only
two masks and one processing step (in addition to the electroplating) were
required for transducer fabrication. Furthermore, the requisite alignment
tolerances for the masks (± .001 inch) are quite lax by integrated circuit
standards. Except that the thin transducers were rather fragile, no sig-
nificant fabrication problems were encountered during construction, thereby
establishing the feasibility of constructing additional transducers and
demonstrating that this type of structure can indeed by reliably and
economically produced.

5.2 Experimental Apparatus

The experimental transducers were tested using a pulse-echo technique
in which the same transducer serves as both a transmitter and a receiver
of ultrasonic energy. A block diagram of the experimental apparatus is
presented in Fig. 5-4, and photographs appear in Figs. 5-5 and 5-6. In
principle, the transmitter is excited by a gated sine wave of fixed but
variable frequency, and an echo is obtained from a cylindrical rod located
in the far field of the transducer radiation field. Both the transducer
and target rod are immersed in a water bath. The rod is oriented normal
to the plane in which the radiation from the transducer is steered (i.e.,
normal to the yz-plane of Figs. 3-1 and 3-2) with the angle between the
transducer normal and the target rod an experimental parameter. We show
in Section 5-3 that for any given frequency of excitation and target
angle, the amplitude of the target echo is proportional to the square of
the transducer sensitivity; therefore, by rotating the transducer about
its axis while keeping the target rod fixed, a plot of the angular
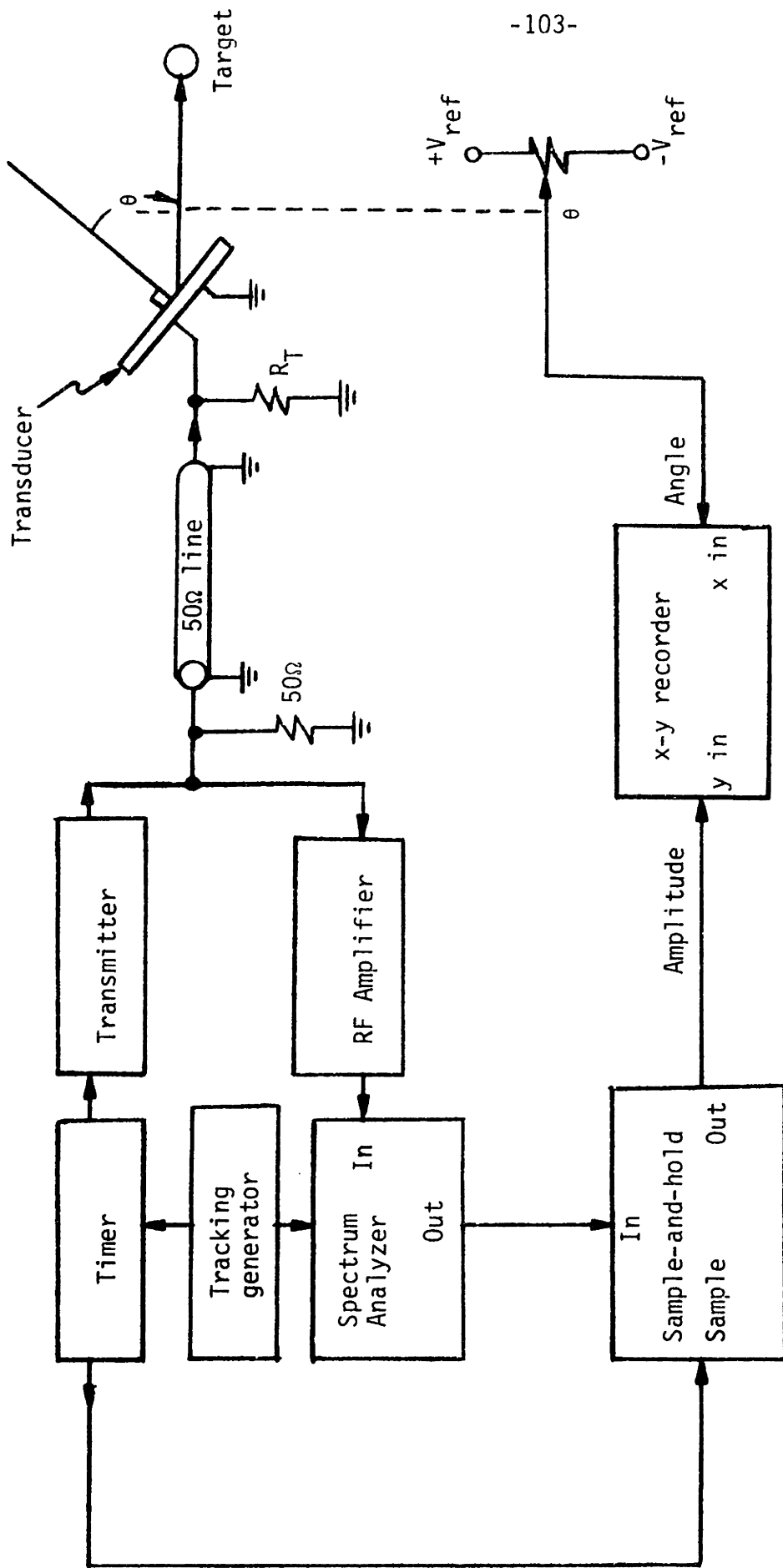
-103-

Figure 5-4. Block diagram of experimental apparatus.

Table 5-3. Specifications of experimental apparatus used for pulse-echo transducer measurements.

Fluid medium: tap water at room temperature

Target data:

    Target: stainless steel rod

    Target length   =   40 cm

    Target diameter   =   d   =   0.635 cm   (= 0.25 inch)

    Target range   =   R   =   25 cm ± 0.5 cm

Frequency range for measurements: 2 MHz to 8 MHz

Transmitted frequency accuracy   =   ± 0.005%

Transmitted waveform:

    Fundamental component of transmitter short-circuit output current:

        I_t =   100 mA zero to peak

    Pulse duration   =   250 μs

    Pulse repetition rate   =   100 Hz

Spectrum analyzer settings:

    RF bandwidth   =   100 kHz

    Video bandwidth   =   10 kHz

Amplitude measurements:

    Accuracy*   =   ± 0.1 dB from 1.5 MHz to 10 MHz

    Day-to-day repeatability   =   ± 0.5 dB

Angle measurements:

    Accuracy   =   ± 0.3 degree

    Day-to-day repeatability   =   ± 0.2 degree

---

* Accuracy of loop (see Fig. 5-4) consisting of tracking generator, timer, transmitter, attenuator (used for calibration only), 25 feet of coaxial cable, RF amplifier, spectrum analyzer and sample-and-hold. For small signal levels (less than − 90 dBm   =   10 μv zero to peak) referred to the RF-amplifier input, the accuracy of the spectrum analyzer must be derated - see instruction manual.

Table 5-3. (Cont'd.)

Terminating resistors and time constants:
 	
    Transducer A $= R_T = 5\Omega$, $R_T C_0 = 11$ ns
 	
    Transducer B $= R_T = 10\Omega$, $R_T C_0 = 11$ ns
 	
    Transducer C $= R_T = 30\Omega$, $R_T C_0 = 11.7$ ns
 	
    Transducer D $= R_T = 30\Omega$, $R_T C_0 = 9.3$ ns

dependence of transducer squared sensitivity for fixed frequency is obtained
on an x-y recorder.

Consider the block diagram of the experimental apparatus presented in
Fig. 5-4.* The spectrum analyzer (Hewlett-Packard 8552B mainframe with
8553L plug-in) serves as a tuned, narrowband receiver and precision ampli-
tude detector for the signals returned from the target. A calibrated out-
put proportional to either the input signal amplitude or to the logarithm
of the input signal amplitude is available from the spectrum analyzer.
The RF amplifier functions as a low-noise preamplifier for the spectrum
analyzer and isolates the sensitive input stage of the spectrum analyzer
from the transmitter output.

The tracking generator (Hewlett-Packard 8443A) provides the spectrum
analyzer in Fig. 5-4 with a clock operating at the transmitter frequency,
eliminating the need to re-tune the spectrum analyzer each time the trans-
mitter frequency is varied. The timer produces two outputs. One output is
a gated square wave to drive the the transmitter, as will be discussed
shortly; the other is a narrow pulse which is delayed by a fixed time inter-
val from the beginning of each square-wave burst. This narrow pulse con-
trols a sample-and-hold which provides a constant-amplitude signal to one
input to the x-y recorder by sampling the spectrum analyzer output after
the echo returned from the target has reached steady state. The other
input to the x-y recorder is derived from the center tap of a potentiometer,
and indicates the angle between the target and the transducer normal.

Physically, the transmitter and receiver are located within a few
inches of one another. The transmitter output is connected to both the

---

*
 Schematic diagrams of the transmitter, receiver and timer are pre-
sented in Appendix III.

receiver input and to one end of a 50 ohm coaxial cable. The cable is terminated at the "transmitter" end in a 50 ohm resistor, and at the other "transducer" end, which may be several feet away, in a resistor R_t. The transmitter has a high-impedance "current source" output stage; therefore the Norton equivalent circuit seen by the transducer looking back into the coaxial line consists of a current source in parallel with resistor R_T, where R_T is the parallel combination of R_t and the 50 ohm characteristic impedance of the coaxial line. The amplitude of the current source is equal to the short-circuit transmitter output current delayed by a time equal to the transit time of the coaxial line.

The terminating resistor R_t is chosen such that R_T is small compared to the transducer input impedance at all frequencies of interest. Therefore, the transducer is in effect driven by a voltage source of value $I_t R_T$. Furthermore, the voltage measured at the transducer end of the coaxial line in response to a target echo is equal to the product $I_r R_T$, where I_r is the short-circuit transducer output current due to the target echo. Since the transmitter/receiver end of the coaxial line is terminated in the characteristic impedance of the line, no reflections occur in the line, and the same voltage $I_r R_T$ will be applied to the input of the RF amplifier after a time delay equal to the transit time of the coaxial line. An important advantage of this transmission line arrangement is that the pulse-echo transducer measurements are independent of the length of the coaxial line, except for a time delay equal to the two-way transit time of the line. In the next section we shall relate the target-echo voltage,

$$V_r = I_r R_T \quad , \qquad (5\text{-}1)$$

to the acoustic intensity radiated by the transducer.

It was stated earlier that in principle the transmitter short-circuit output current, I_t, is a gated sine wave. In fact, the actual output current from the transmitter is a gated square wave, which is a far easier type of waveform to generate. But since the transducer is a linear device, and since the spectrum analyzer functions as a narrowband receiver, the output of the spectrum analyzer responds to only the fundamental component of the square wave drive.

Specifications of the experimental apparatus used for the pulse-echo transducer measurements are listed in Table 5-3. Notice that target-echo amplitude measurements are accurate to within $\pm$ 0.1 dB, and that measurements repeated from day to day (which thus involve experimental variables such as target alignment) agree within $\pm$ 0.5 dB. Angular measurements are accurate to $\pm$ 0.3 degree and repeatable to $\pm$ 0.2 degree.

Photographs of the mechanical apparatus for holding a transducer under test and positioning it with respect to its target are presented in Figs. 5-5 and 5-6. As shown in Fig. 5-6, the transducer is mounted (using Duco cement) on a plexiglass slide which fits into an aluminum transducer holder. Figure 5-5 illustrates that the transducer holder is secured to the underside of a motor-driven turntable, and that the shaft of a precision potentiometer is fastened to the upper side of the turntable.*

The transducer target is a stainless steel rod 0.25 inch in diameter. This target is positioned in the far field of the transducer radiation field and remains fixed as the transducer is rotated about its axis. Since the characteristic impedance of stainless steel is more than 30
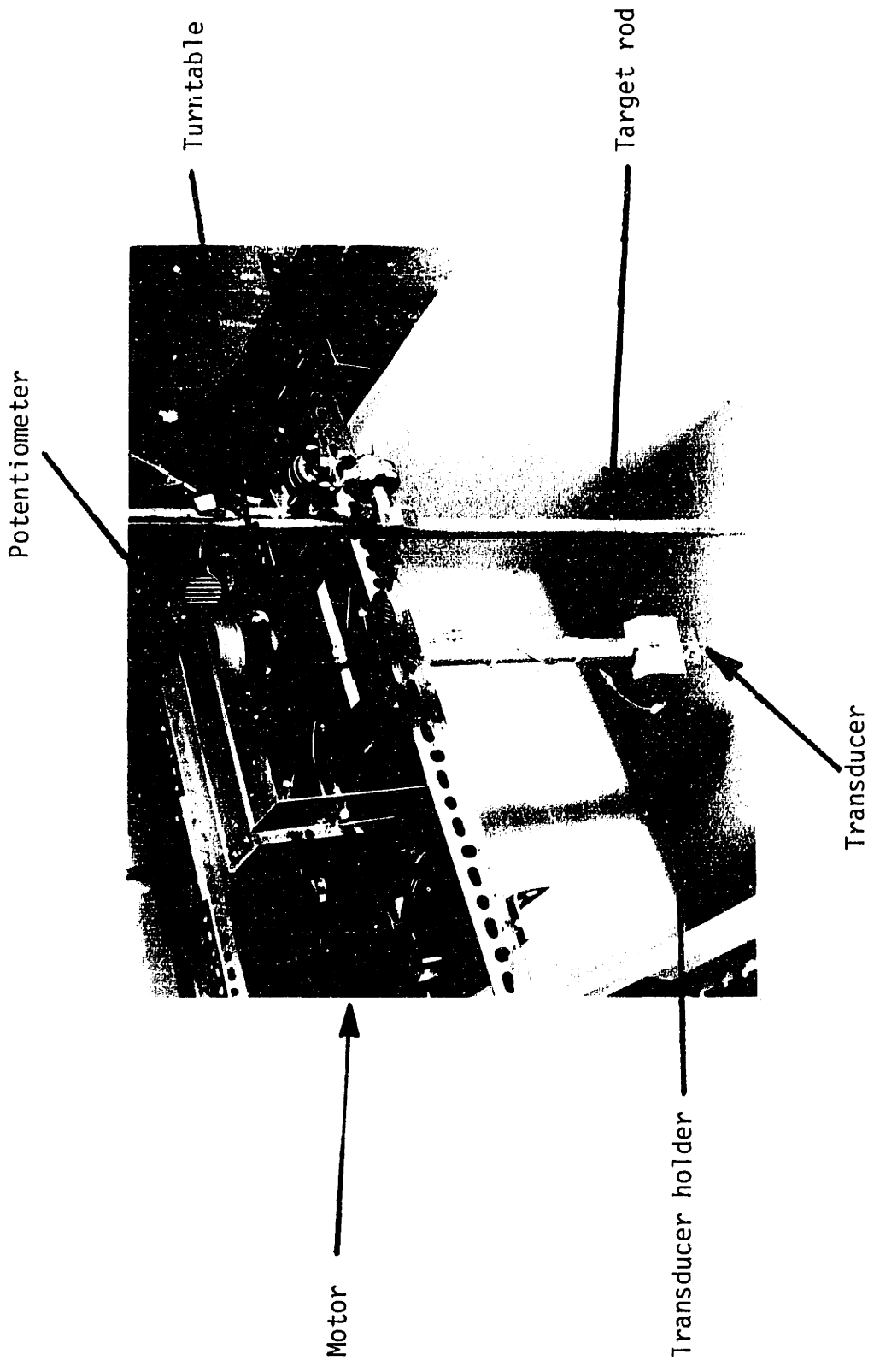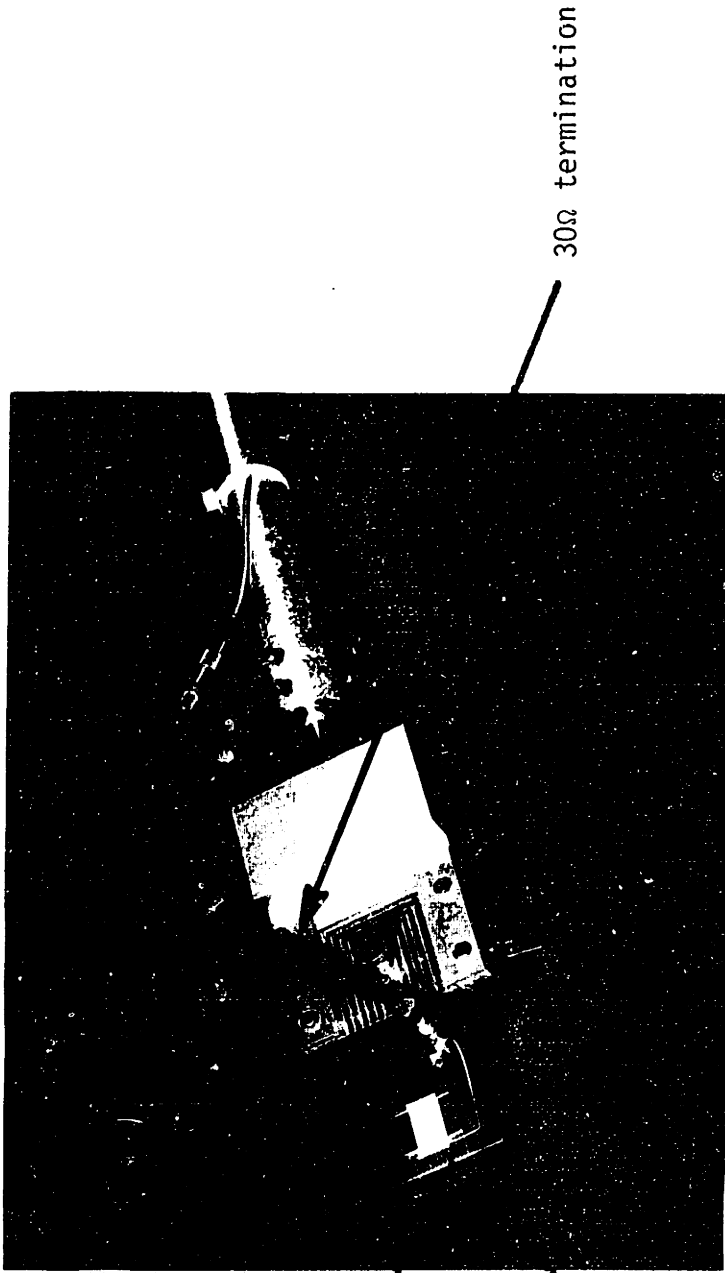

Figure 5-5. Photograph of mechanical apparatus for transducer testing.

30Ω termination

Plexiglass slide

Transducer

Figure 5-6.   Photograph of transducer holder.

times greater than that of water, the target rod serves as a rigid reflector of ultrasound.

If a set of rectangular coordinate axes is assigned to the transducer under test as shown in Fig. 3-1, the turntable rotates the transducer about its x-axis. Moreover, the target rod is aligned normal to the yz-plane defined by the transducer axes of Fig. 3-1, so that the potentiometer indicates the angle, θ, measured in the yz-plane between the transducer z-axis and the center of the target rod. Thus, the experimental apparatus permits measurement of transducer sensitivity in the directions ($\phi_x=0$, $\phi_y=0$), θ variable, where ϕ_x and ϕ_y are defined in Fig. 3-2.

Two general comments concerning the transducer testing procedure are appropriate. The first concerns the practical reasons for using a cylindrical rod as a target, rather than a sphere which might seem the more natural choice. The rod has a larger radar cross section than a sphere of the same diameter, and therefore returns a larger fraction of the incident ultrasonic energy to the transducer. Furthermore, though the transducers described in this report steer in only one dimension, they produce beams which are narrow in two dimensions (see Fig. 3-3). Therefore, a rod is easier to align experimentally than a sphere, since the latter must be aligned in both dimensions.

The second comment concerns the fact that the measurements of transducer performance are made in the far field of the transducer radiation field, while many potential applications, such as those discussed in Chapter 1, involve operation in the transducer near field. The radiation intensity from the transducer is a relatively smooth function of position in the far field, compared to the near field in which quite rapid local variations in radiation intensity may occur because of Fresnel

diffraction. These variations make measurements in the near field highly dependent upon precise target size and shape; targets comparable to or larger than a wavelength tend to average the rapid variations in near-field intensity in complicated ways dependent upon the detailed target structure. Hence, the only reasonable transducer performance measure is the far-field directivity. Since Fresnel diffraction effects are not peculiar to the transducers described in this report but are common to all transducers used in their near fields (for example see Refs. 27 and 28), a study of these effects is worthwhile, although beyond the scope of this report.

5.3 Evaluating Transducer Performance

We have two main objectives in this section:

1. to discuss the normalization procedure used in obtaining the experimental data presented in the next section, and to argue that this procedure allows the data from different transducers to be directly compared, and

2. to derive an explicit relation between $V_r(\theta)$, the experimentally measured target-echo voltage versus angle, and the angular dependence of the far-field acoustic intensity produced by the transducer.

To illustrate the need for a normalization procedure in measuring transducer performance, consider the effect of terminating resistor R_T on target-echo voltage V_r. As discussed in Section 5-2, the experimental transducers are in effect driven from a voltage source of amplitude $I_t R_T$, where I_r is the short-circuit transducer output current due to the target echo. Since the transducer is linear, it follows that the target-echo

voltage is proportional to R_T^2 (providing, of course, that R_T remains small compared to the transducer input impedance as required in the preceding section).

Since V_r is proportional to the square of the terminating resistor, it is important to choose R_T carefully if the target-echo voltages from different transducers are to be directly compared. Experimental measurements have determined that the input admittances of the transducers described in Section 5.1 are dominated by their shunt capacitances, C_0*. Therefore, one reasonable procedure for testing transducers is to insert a transformer between the coaxial cable and the transducer under test; the transformer turns ratio would be selected to convert the transducer shunt capacitance C_0 to a standard value for all measurements, and a standard value of R_T would also be used for all measurements. This technique amounts to approximately normalizing the input impedances of the transducers before measuring their sensitivities. An equivalent procedure, which is the one we have actually followed, is to select R_T such that the product $R_T C_0$

---

* C_0 is the electrical capacitance that would be measured across the trans-- ducer terminals if the substrate could be clamped to prevent any lateral movement (see Appendix II). This capacitance appears in parallel with any electrical loading due to actual substrate motion and subsequent acoustic radiation.

The dominance of the transducer input admittance by C_0 is illustrated for the transducers C and D by observing that their input-admittance phase angle, $\angle Y$, satisfies

$$75° < \angle Y < 90°$$

over the frequency range extending from 1 MHz to 10 MHz. Transducers A and B exhibit somewhat greater phase-angle variations near their frequencies of strong resonance, but their input admittances, too, are dominated by C_0.

is the same constant, eleven nanoseconds, for each transducer. The values of R_T and $R_T C_0$ applicable to each transducer are provided in Table 5-3.

Our second task in this section is to obtain a relation between V_r and the far-field acoustic intensity radiated by the transducer. In the process of this derivation, we shall define two new measures of transducer sensitivity, namely the transducer far-field transmitting and receiving factors, which may be useful in their own right. Naturally, each of these quantities, namely the target-echo voltage V_r, the radiated acoustic intensity and the transmitting and receiving factors, are functions of the angle between the transducer normal and the direction of measurement.

Figure 5-7 illustrates a transducer having one electrical port and located at the origin of a coordinate system. The transducer produces acoustic radiation incident upon an infinitesimal, acoustically hard spherical target located at point P in the fluid medium. We assume the transducer is oriented with respect to the axes of a rectangular coordinate system as shown in Fig. 3-1, and that the point P has the spherical coordinate angles defined relative to the rectangular coordinate axes as shown in Fig. 3-2. In general, the point P may be located in either the near field or the far field of the transducer.

Assume the transducer is excited by a sinusoidal steady-state voltage of amplitude V_t, and let p_t be the resultant acoustic pressure amplitude measured at the point P. Since the sphere at P is infinitesimal, the pressure p_t is the same pressure that would be measured as the point P in the absence of the sphere. Let $T(r,\theta,\varphi)$ be the ratio of acoustic pressure at P to the transmitting voltage,

$$T(r,\theta,\varphi) = \frac{p_t(r,\theta,\varphi)}{V_t} \qquad . \qquad (5-2)$$
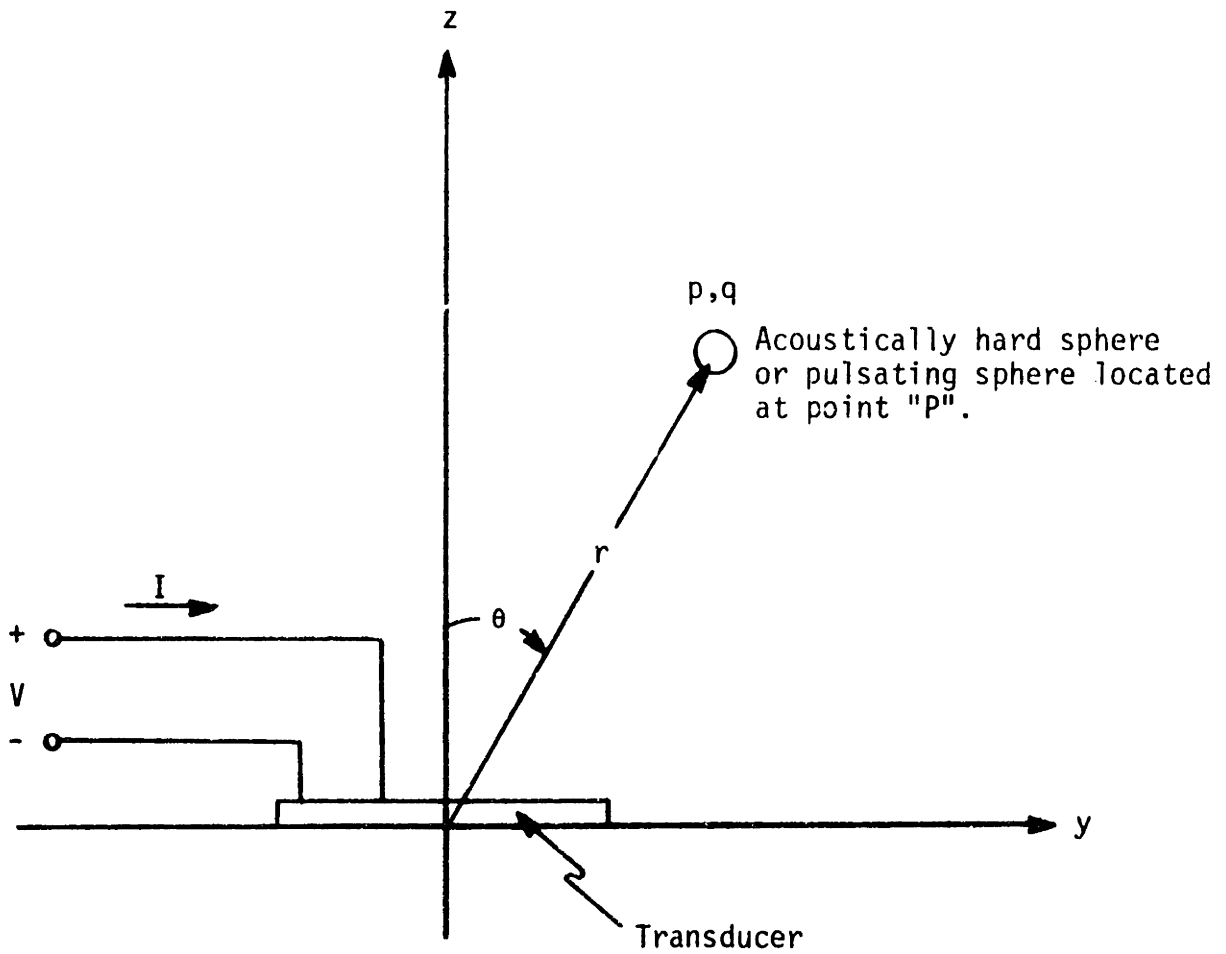
Figure 5-7. Transducer having one electrical port and located at the origin of a coordinate system.

Since the acoustic pressure varies as $\frac{1}{r}$ in the transducer far field, the product $rT(r,\theta,\varphi)$ approaches a limiting value for large r,

$$T_f(\theta,\varphi) = \lim_{r \to \infty} rT(r,\theta,\varphi) \quad , \tag{5-3}$$

where $T_f(\theta,\varphi)$ is the normalized far-field transmitting factor.

Now assume that the transducer is used as a receiver of acoustic energy produced by sinusoidal pulsations of the infinitesimal sphere located at the point P. If v_r denotes the amplitude of the radial component of particle velocity on the surface of the sphere, and if a is the radius of the sphere, the volume velocity q_r of the spherical source is given by

$$q_r = 4\pi a^2 v_r \quad . \tag{5-4}$$

Therefore the pulsating sphere radiates a spherical wave with acoustic pressure amplitude

$$p_r = \frac{\omega \rho q_r}{4\pi r} \tag{5-5}$$

at distance r from the sphere[23]. Let $U_f(r,\theta,\varphi)$ of the transducer be the quotient of the transducer short-circuit output current divided by the incident acoustic spherical wave pressure amplitude measured at the transducer,

$$U(r,\theta,\varphi) = \frac{I_r}{p_r} \quad . \tag{5-6}$$

When the distance, r, between the transducer and the point P is large, the spherical acoustic wave incident on the transducer approximates a plane wave. Therefore, the receiving factor approaches a limiting value,

$$U_f(\theta,\varphi) = \lim_{r \to \infty} U(r,\theta,\varphi) \quad , \tag{5-7}$$

where $U_f(\theta,\varphi)$ is the far-field receiving factor.

To obtain the relationship between the transducer transmitting and receiving factors, the system consisting of the transducer, the fluid medium and the infinitesimal sphere is considered as a linear passive two-port network. As shown in Fig. 5-8, the input parameters are the transducer voltage and current, and the output parameters are the acoustic pressure and volume velcotiy on the surface of the infinitesimal sphere. Since mechanical and piezoelectric systems obey reciprocity[29], it follows that

$$\left(\frac{p_t}{V_t}\right)_{q_t=0} = \left(\frac{I_r}{q_r}\right)_{v_r=0} \quad , \tag{5-8}$$

where the "t" subscripts refer to the case where the transducer is transmitting and the sphere is passive, and the "r" subscripts refer to the case of the sphere pulsating and the transducer passive. Using Eqs. (5-2), (5-5), (5-6) and (5-8), we find

$$\frac{T(r,\theta,\varphi)}{U(r,\theta,\varphi)} = \frac{\rho\omega}{4\pi r} \quad . \tag{5-9}$$

From Eqs. (5-3) and (5-7), the far-field transmitting and receiving factors are related by

$$\frac{T_f(\theta,\varphi)}{U_f(\theta,\varphi)} = \frac{\rho\omega}{4\pi} \quad . \tag{5-10}$$

We are now in a position to relate the normalized far-field transmitting factor, $T_f\left(\theta,\frac{\pi}{2}\right)$, of an experimental transducer directly to the pulse-echo measurements obtained from the apparatus described in the preceding section. According to that section, the transducer is driven by a voltage source of amplitude $I_t R_T$; therefore the acoustic pressure amplitude at a point $\left(R,\theta,\frac{\pi}{2}\right)^*$ in the transducer far field is

---

* Note that $\left(R,\theta,\frac{\pi}{2}\right)$ is the location, in spherical coordinates, of the center of the target rod in the yz-plane of Fig. 3-2.
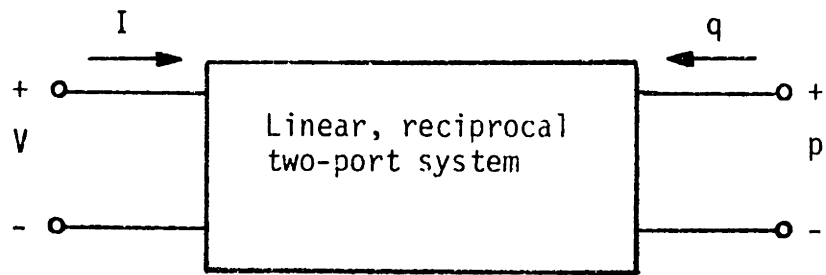
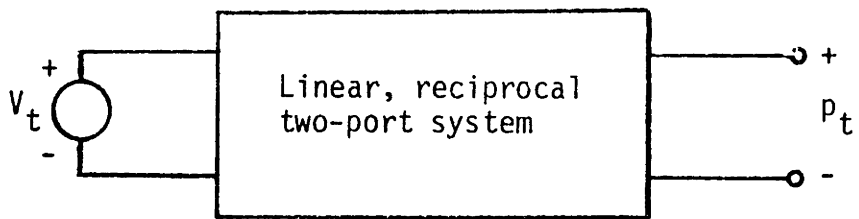Figure 5-8a. The system in Figure 5-7 is linear and reciprocal[29].

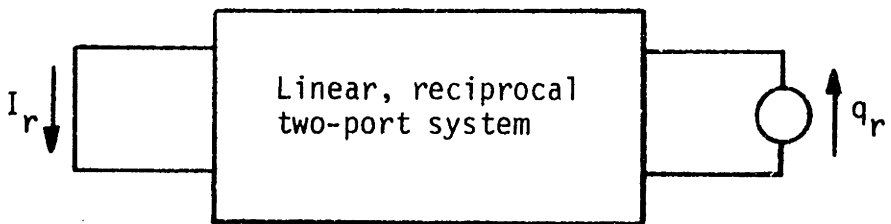Figure 5-8b. "Voltage" transfer ratio $= \dfrac{p_t}{V_t}$.

Figure 5-8c. "Current" transfer ratio $= \dfrac{I_r}{q_r}$.

Figure 5-8. According to reciprocity[35], the "voltage-" and "current-" transfer ratios are equal for the system in Figure 5-8a.

transmitted pressure at $\left(R,\theta,\frac{\pi}{2}\right)$ = $\dfrac{I_t R_T T_f\left(\theta,\frac{\pi}{2}\right)}{R}$. (5-11)

The target rod intercepts a portion of the radiated power and re-radiates it in the direction of the transducer. When the target diameter d is sufficiently large that

$$\frac{\pi d}{\lambda} = \frac{\omega d}{2c} >> 1 \quad , \tag{5-12}$$

the fraction of incident power backscattered to the transducer can be determined by the techniques of geometrical optics (see Ref. 13, Section 2.7). The minimum frequency for which the transducers were tested was 2 MHz. For this frequency,

$$\frac{\omega d}{2c} \approx 27 \quad , \tag{5-13}$$

so geometrical techniques for backscatter calculations are indeed applicable. It follows that if γ_t is the acoustic intensity incident on the target rod, the backscattered intensity γ_r measured at the transducer is

$$\gamma_r = \left(\frac{1}{2}\right)\left(\frac{d}{4R}\right)\gamma_t \quad . \tag{5-14}$$

The factor $\frac{1}{2}$ in (5-14) results from the spreading of acoustic radiation in the plane containing the transducer and the axis of the target rod. Radiation in this plane suffers a mirror-like reflection and appears to return from an image transducer located at $\left(2R,\theta,\frac{\pi}{2}\right)$; that is, from a distance twice that separating the transducer and the target rod. In any plane perpendicular to the target axis, incident radiation is scattered in all directions by the circular rod; the fraction of the incident intensity backscattered in the direction of the target is $\frac{d}{4R}$ (see Ref. 30).

Since acoustic pressure is proportional to the square root of intensity, the backscattered pressure incident on the transducer can be obtained

from (5-11) and (5-14),

$$P_r = \frac{I_t R_T T_f\left(\theta,\frac{\pi}{2}\right)}{R} \sqrt{\frac{d}{8R}} \quad . \tag{5-15}$$

Using definitions (5-6) and (5-7) for the far-field receiving factor, the short-circuit transducer output current due to the backscattered acoustic energy is

$$I_r = \frac{U_f\left(\theta,\frac{\pi}{2}\right) T_f\left(\theta,\frac{\pi}{2}\right) I_t R_T}{R} \sqrt{\frac{d}{8R}} \quad . \tag{5-16}$$

Combining Eqs. (5-1), (5-10) and (5-16), the ratio of the received voltage V_r to the transmitter short-circuit output current I_t is

$$\frac{V_r}{I_t} = T_f^2\left(\theta,\frac{\pi}{2}\right) R_T^2\left(\frac{\pi}{\rho\omega}\right)\sqrt{\frac{2d}{R^3}} \quad . \tag{5-17}$$

For our final step, we use Eq. (5-17) to express the far-field acoustic intensity in terms of the experimentally measured target-echo voltage, V_r. Since the time-averaged intensity γ of an acoustic plane wave is related to the zero-to-peak pressure amplitude p according to[23] the zero-to-peak pressure amplitude p according to[23]

$$\gamma = \frac{|p|^2}{2\rho c} \quad , \tag{5-18}$$

it follows from the definition of $T_f\ \theta,\frac{\pi}{2}$ that

$$\gamma\left(r,\theta,\frac{\pi}{2}\right) = \frac{V_t^2 T_f^2\left(\theta,\frac{\pi}{2}\right)}{2\rho c r^2}$$

$$= \frac{I_t^2 R_T^2 T_f^2\left(\theta,\frac{\pi}{2}\right)}{2\rho c r^2} \quad . \tag{5-19}$$

Combining Eqs. (5-17) and (5-19) and substituting parameters specified in Tables 5-1 and 5-3,

$$\gamma\left(r,\theta,\frac{\pi}{2}\right) = \frac{136\ V_r(\theta)}{r^2\ \sin\theta_0} \quad . \tag{5-20}$$

Here $\sin\theta_0$ is defined in terms of the frequency of excitation according to (2-20),

$$\sin\theta_0 = \frac{2\pi c}{L\omega} \quad . \tag{2-20}$$

Equation (5-20) provides an explicit relation between $V_r(\theta)$ and the far-field acoustic intensity produced by the transducer when driven by a voltage of amplitude $I_t R_T$. If the distance r from the transducer is measured in centimeters, Eq. (5-20) gives the radiated intensity in units of watts/cm^2.

Since no independent experimental measurements have been performed to test Eq. (5-20), it is worthwhile to estimate the accuracy of this relation. The use of Eq. (5-20) is an example of a self-reciprocity transducer calibration; this type of calibration is generally considered to be the most accurate calibration technique available (see Ref. 23, Section 6.6). However, our experimental procedure introduced at least three important sources of error which limit the accuracy of Eq. (5-20). The error from each source increases with increasing frequency of measurement; the three error sources are described below:

1. Our measurements were conducted in the transducer far field in the sense that the target was located beyond the Fresnel-diffraction region. But especially at the higher measurement frequencies, the target distance was insufficient for precise application of the far-field self-reciprocity calculation.[31] Error introduced by this source is approximately 1 dB at 5 MHz for the thick transducers.*

2. No allowance has been made for attenuation losses in the water bath; at 5 MHz, these losses may amount to 2.5 dB.**

---

* This error source may be compensated for by use of a correction factor such as developed in Ref. 31.

** See Table 1-2.

3. It was assumed in deriving (5-20) that R_T is much smaller than the transducer input impedance over the frequency range of interest. If $R_T C_0$ = 11 ns, and if the transducer input admittance is dominated by C_0, the error due to non-zero R_T is approximately 1 dB at 5 MHz.

We see that several factors contribute to the uncertainty of the scale factor relating V_r and γ in Eq. (5-20). Nonetheless, Eq. (5-20) is certainly accurate enough for order-of-magnitude intensity calculations, which are sufficient for our analysis of transducer performance. Moreover, none of the three error sources listed above affect the conclusion from (5-20) that for any given frequency of excitation and any distance r, the radiated acoustic intensity $\gamma\left(r,\theta,\frac{\pi}{2}\right)$ is directly proportional to $V_r(\theta)$. Therefore, even though the constant of proportionality may be somewhat uncertain in (5-20), the experimental measurements of $V_r(\theta)$ presented in the next section do possess the correct angular dependence of the radiated acoustic intensity. Knowledge of the angular dependence of the radiated acoustic intensity permits investigation of transducer side-lobe levels, which is generally far more important than the precise determination of the intensity scale factor.

5.4 Experimental Data

In this section we present data illustrating the performance of the four experimental transducers described in Section 5-1. In nearly all cases the experimental quantity considered is $V_r(\theta)$, the received voltage due to target echos, as a function of target angle θ. As discussed in Sections 5-2 and 5-3, $V_r(\theta)$ is directly proportional to the intensity of the acoustic radiation produced by the transducer in direction θ. In view of the normalization procedure for selecting R_T, the sensitivity of different transducers can be directly compared in terms of measured values of $V_r(\theta)$.

The performance of the four transducers has been studied over the frequency range from 2 MHz to 8 MHz. As a point of reference, the frequency range (2-19) for radiation from only the first term in the summation (2-11) for $\delta(y)$ extends from 1.8 MHz to 5.3 MHz; moreover, it is only over this frequency range that the substrates for transducers A and C can be considered "thin". The thick transducers B and D satisfy conditions (4-9) and (4-10) for the elimination of the third harmonic in the summation (2-11) for $\delta(y)$; for these transducers the range for radiation from only the first term of (2-11) extends from 1.8 MHz to 8.8 MHz.

Figure 5-9 is a plot of $V_r(\theta)$ for thick transducer D over the full 360° angular range; the zero-degree reference direction is normal to the ground-plane side of the transducer. This plot illustrates several features characteristic of all transducers tested:

1. While side lobes are evident in Fig. 5-9, most of the radiated energy is confined to four well-defined beams.

2. The four primary beams produced by the transducer are symmetrically located with respect to the transducer normal at the angles $\pm\,\theta$ and $180° \pm \theta$, where $\theta \approx 36°$ as predicted by Eq. (2-20). Two of the beams, numbers 1 and 4, are expected from the analysis of Chapter 2; the other two beams arise because even the "thick" transducers are sufficiently thin that similar substrate surface deformations result for both substrate surfaces.

3. Beams 1 and 2 are of approximately equal amplitude even though they are produced by opposite transducer surfaces, and a similar observation applies to beams 3 and 4. However, beams 3 and 4 are each of higher amplitude than the beams 1 and 2. This behavior is probably caused by a linear component in the variation of the ferroelectric ceramic material properties across the substrate. Such a linear grading of material properties would cause the preferential generation of traveling substrate waves in one direction, and would
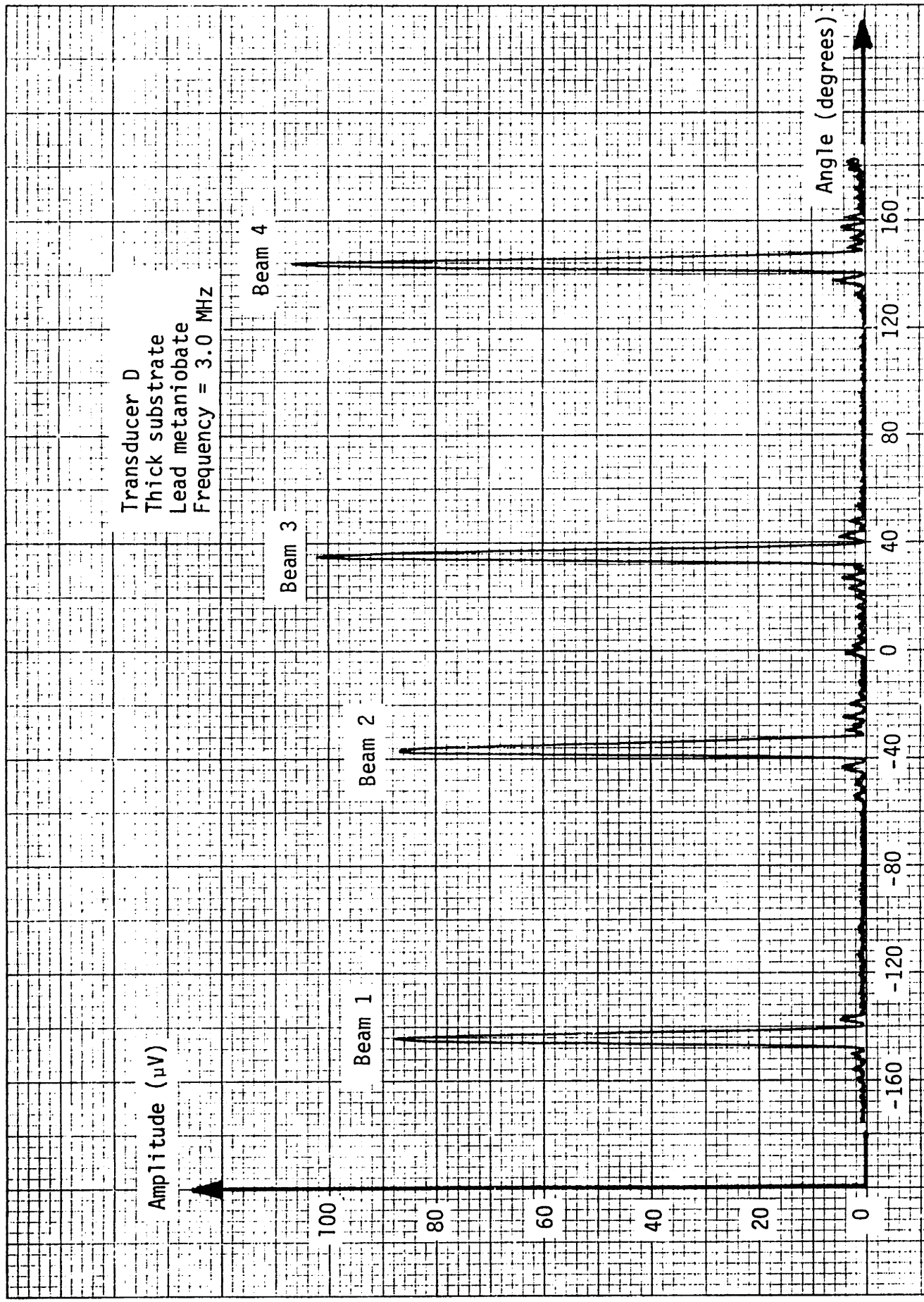
Figure 5-9. Target-echo voltage versus angle.

account for the observed behavior. For other experimental
transducers, beams 1 and 2 were of equal but greater ampli-
tude than beams 3 and 4. The linear grading of material
properties apparently sloped in the opposite direction for
these transducer substrates.

In the remainder of this section we shall evaluate the performance of
each transducer over one quadrant of its radiation field. The measurement
quadrant assigned to each transducer was chosen after examining the four-
quadrant transducer performance for a small sampling of frequencies of
excitation; the quadrant selected for all subsequent measurements was the
one with the "best-behaved" side lobes over the sample frequencies. No
major differences were found among the four quadrants for any specific
transducer, but it is interesting that radiation from the ground-plane
surface was selected for both thick transducers, while radiation from the
interdigitated-electrode-structure surface seemed preferable for both thin
transducers. In the case of the thick transducers, the radiation from the
electrode surface decreased relative to the radiation from the ground-plane
surface at high operating frequencies. This may be due to non-negligible
mass loading from the interdigitated electrode stripes. However, the
small number of transducers tested and the slight differences found among
their four radiation quadrants precludes drawing any firm conclusions.

Figures 5-10 and 5-11 present a sequence of one-quadrant plots of
$V_r(\theta)$ for the two thick transducers, B and D respectively, with frequency
as a parameter. The frequencies were selected such that Eq. (2-20) pre-
dicts an approximately equiangular spacing of 6° between adjacent radi-
ation lobes. Resonances (evidenced by amplitude peaking of the primary
radiation lobe) and side lobes are apparent in Figs. 5-10 and 5-11, al-
though both phenomena are more pronounced in Fig. 5-11. From Table 5-2,
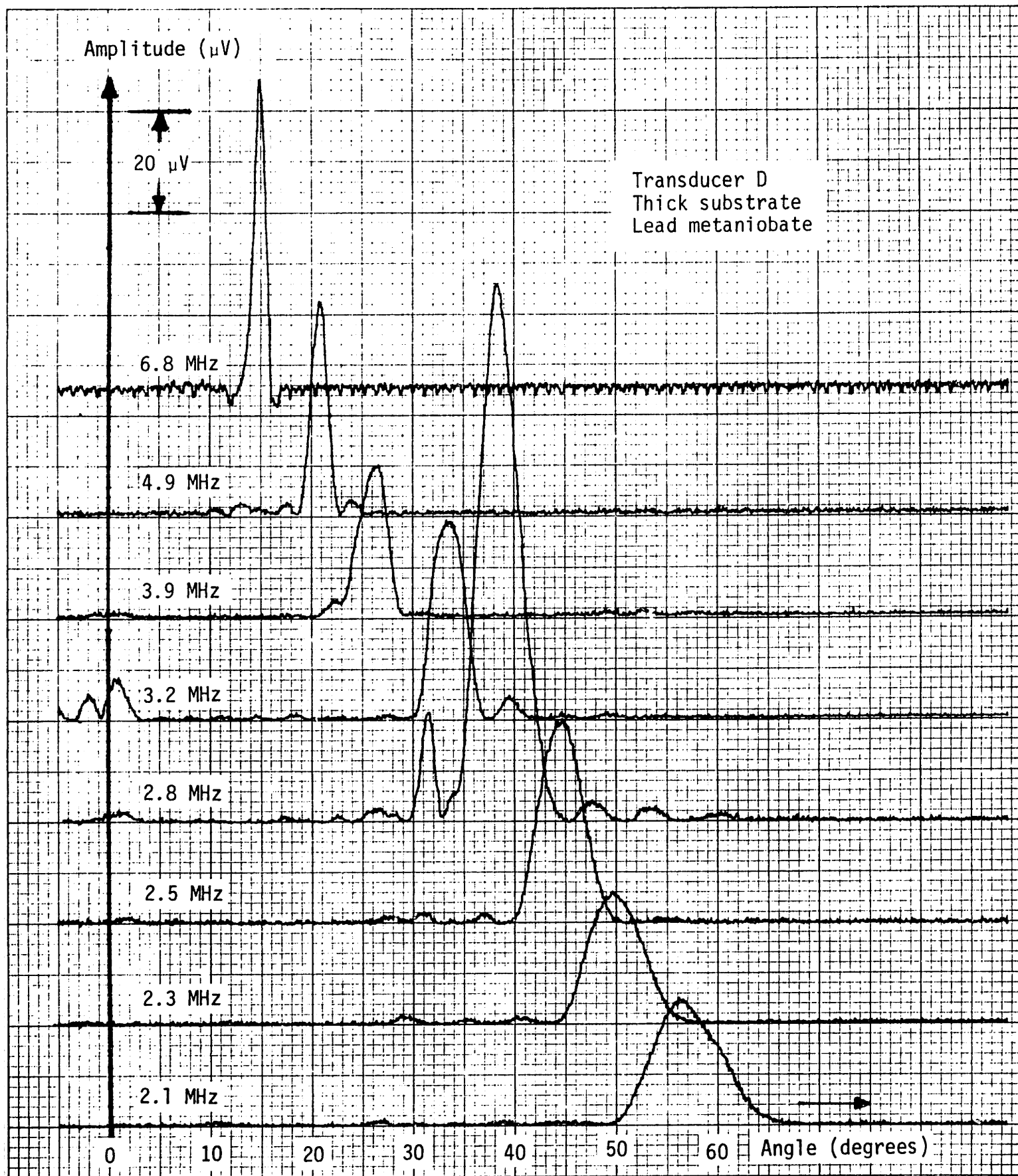we see that the intrinsic Q_m of PZT-5A is $Q_m = 75$, compared with $Q_m = 10$

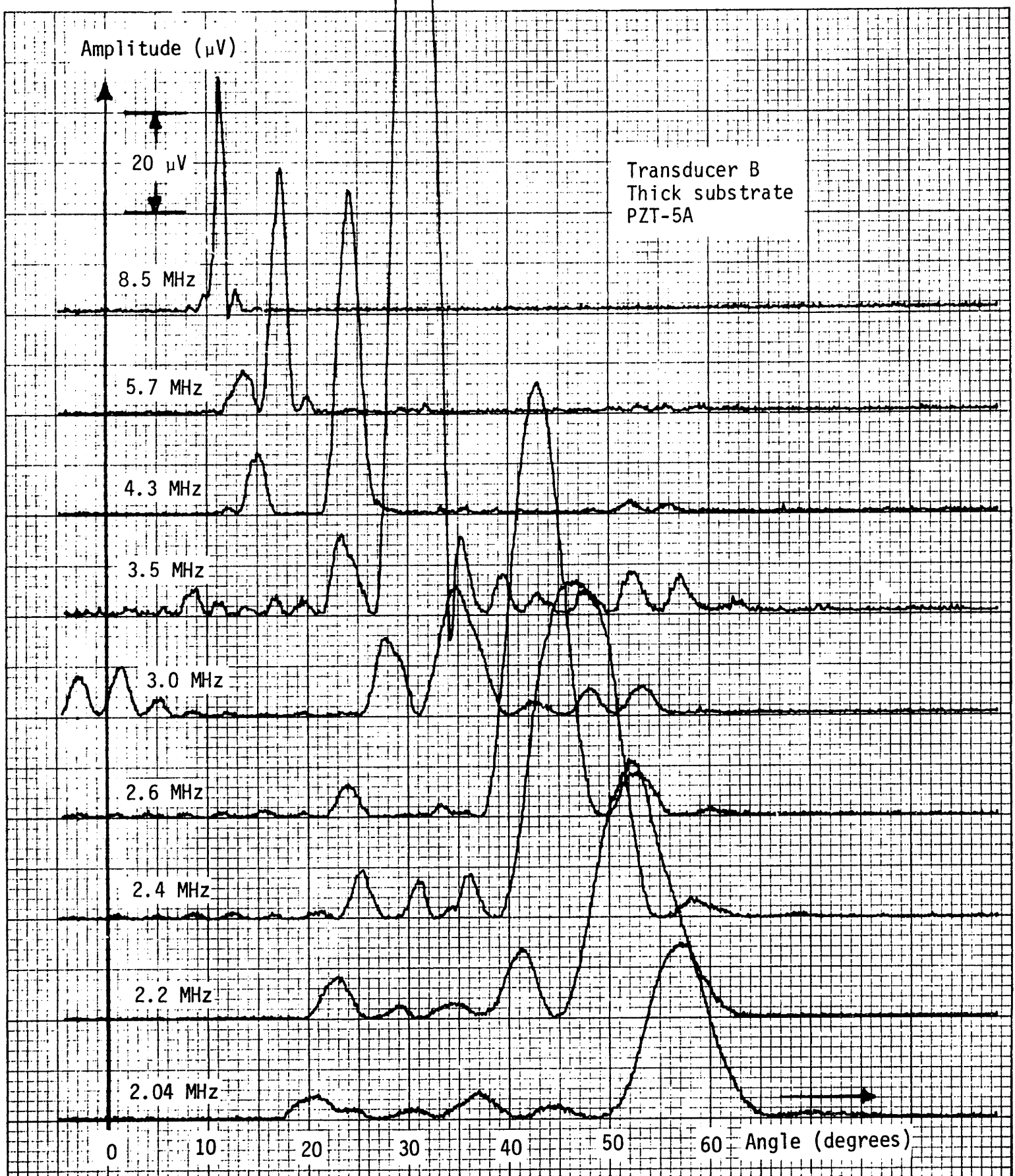Figure 5-10.   Superimposed plots of target-echo voltage versus angle for a sequence of frequencies.

Figure 5-11. Superimposed plots of target-echo voltage versus angle for a sequence of frequencies.

for lead metaniobate. In line with the discussion of Section 4.2.1, the lower Q_m of the lead metaniobate substrate may account for the reduced side lobes and smoother frequency response in Fig. 5-10 compared to Fig. 5-11.

The most important observations concerning Figs. 5-10 and 5-11 are:

1. For any given frequency of excitation, a unique "primary" radiation lobe is clearly evident, although one or more substantial side lobes also occur at some frequencies.

2. The radiation from the transducers indeed steers with frequency, and in view of the nearly equiangular spacing of the primary radiation lobes for sequential frequencies, the direction of the primary transducer radiation is in at least approximate agreement with Eq. (2-20).

These observations apply generally to all of the transducers tested. Therefore, it is possible to summarize a great deal of experimental data concerning transducer performance by plotting various parameters of their primary radiation lobe versus frequency of excitation, or versus the center angle of the radiation lobes.

Figure 5-12 presents graphs of this type intended to illustrate the agreement between the experimentally-measured center angle of the transducer radiation and the angle predicted from Eq. (2-20). Evidently the agreement with theory is excellent; the rms angular deviation of 0.4° is comparable to the precision of the angular measurements specified in Table 5-3, although the measurements in Fig. 5-12 contain additional uncertainty in measuring the radiation center angle due to non-zero beamwidth.

Figure 5-13 demonstrates the frequency dependence of the radiated acoustic intensity at the center angle of the primary lobe. It was stated earlier that the substrates for transducers A and C could only be considered "thin" over the frequency range 2 MHz to 5 MHz. Notice that
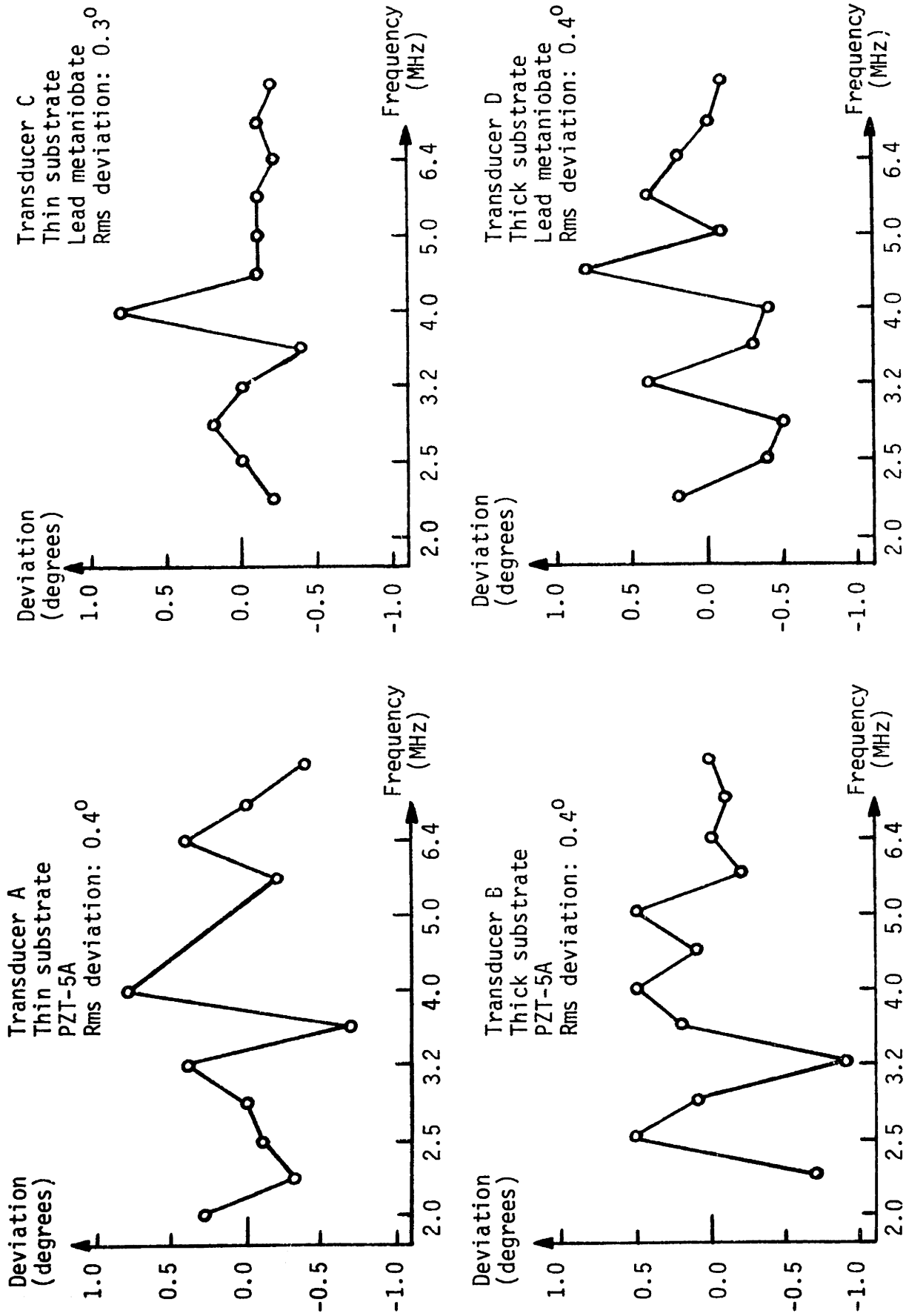
Figure 5-12. Angular deviation (measured angle minus predicted angle) of peak transducer radiation versus frequency.

only a single resonance occurs over that frequency range for these trans-
ducers, just as predicted in Section 4-2. Moreover, transducer A is far
more sensitive than transducer C over this frquency range. Once again this
difference in sensitivity is expected from Chapter 4 because the electro-
mechanical coupling factor applicable to the thin transducer resonances,
k_{31}', is much smaller for lead metaniobate than for PZT-5A (see Table 5-2).

The sensitivity of thick transducers B and D exhibits multiple reson-
ances in Fig. 5-13. These resonances are probably due to high order sub-
strate modes, as discussed in Section 4-3. From Table 5-2, both PZT-5A and
lead metaniobate have comparable (and high) values of k_{33}, the electromech-
anical coupling factor applicable to the high order substrate modes; there-
fore the comparable sensitivity of transducers B and D evident in Fig. 5-13
is also expected.

Figure 5-14 presents the same data as Fig. 5-13 but Eq. (2-20) has been
used to transform the frequency coordinate of Fig. 5-13 to the primary-
lobe center-angle coordinate in Fig. 5-14.

The geometry of the primary transducer radiation lobe obtained from
theoretical considerations is given in Fig. 3-3. The angular beamwidth,
$2\Delta\theta$, shown in Fig. 3-3b, was obtained using the angles of the first zeros
of the directivity function (3-16) to define the beam edges. For experi-
mental purposes, the half-amplitude (6 dB) beamwidth is more prartical
because this measure is less sensitive to nearby spurious radiation lobes.
From the analysis of Section 3-1, the half-amplitude beamwidth is approxi-
mately one-half of the full beamwidth defined in Fig. 3-3b; that is, the
half-amplitude beamwidth is just $\Delta\theta$ from Fig. 3-3b.

Figure 5-15 compares theoretical and experimental values of the
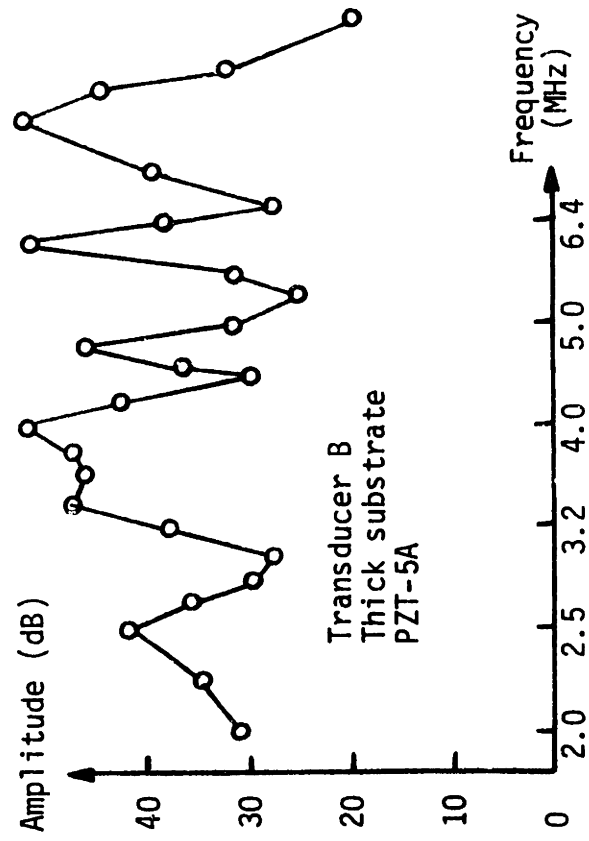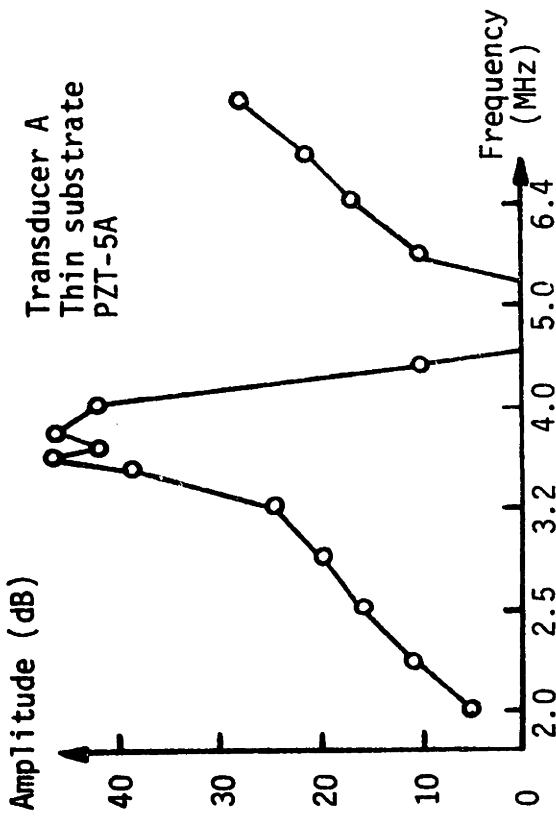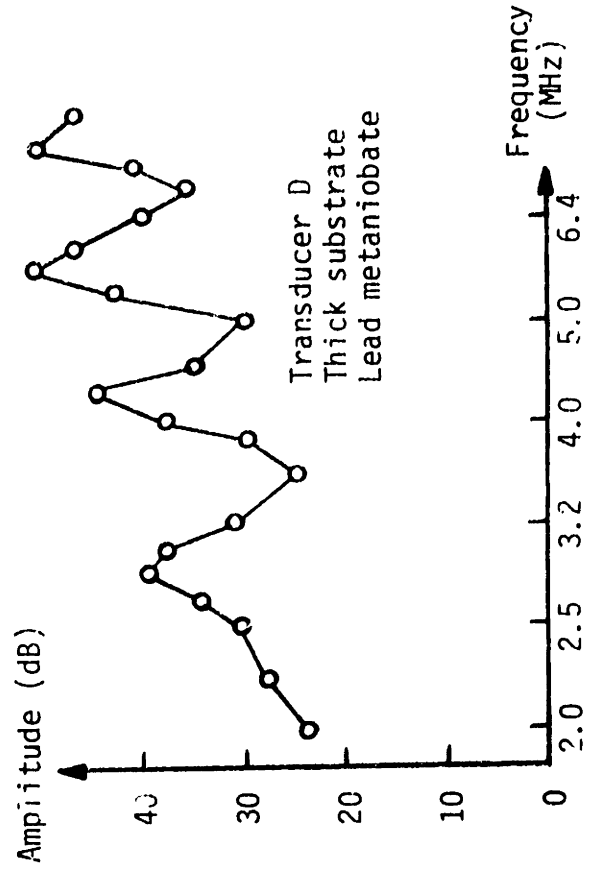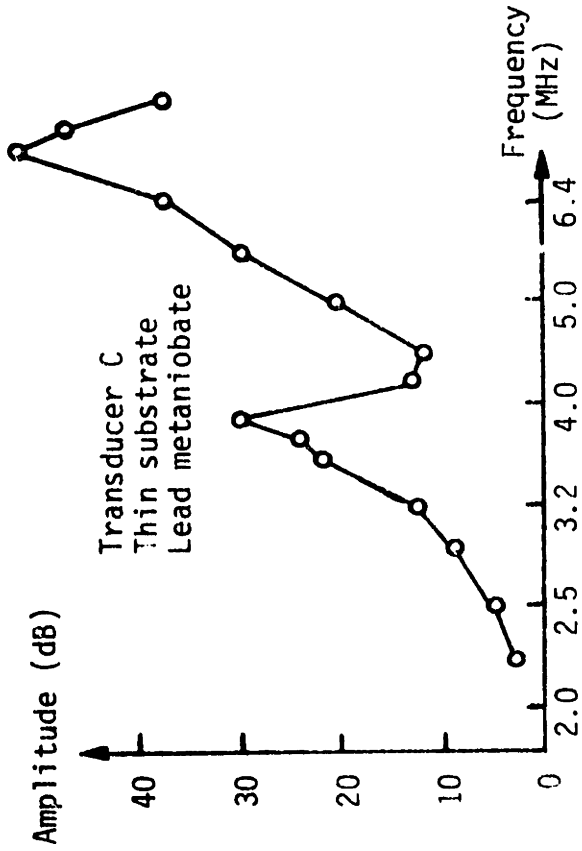half-amplitude beamwidth of the primary transducer radiation lobe at

Figure 5-13. Peak amplitude of target-echo voltage versus frequency; 0 dB = 1 µV zero-to-peak amplitude.
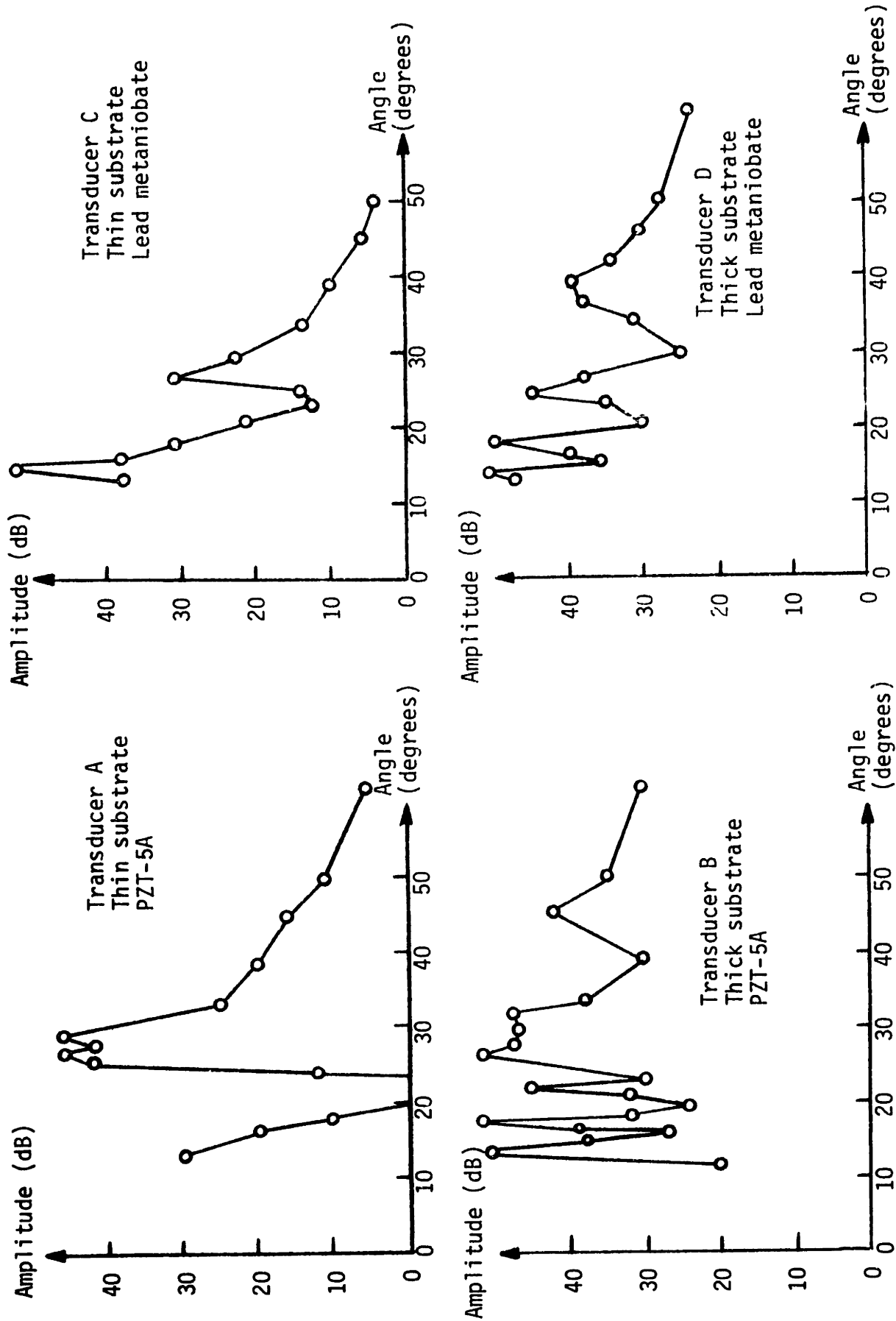
Figure 5-14. Peak amplitude of target-echo voltage versus angle of peak amplitude; 0 dB = 1 µV zero-to-peak amplitude.

6 dB beamwidth
(degrees)
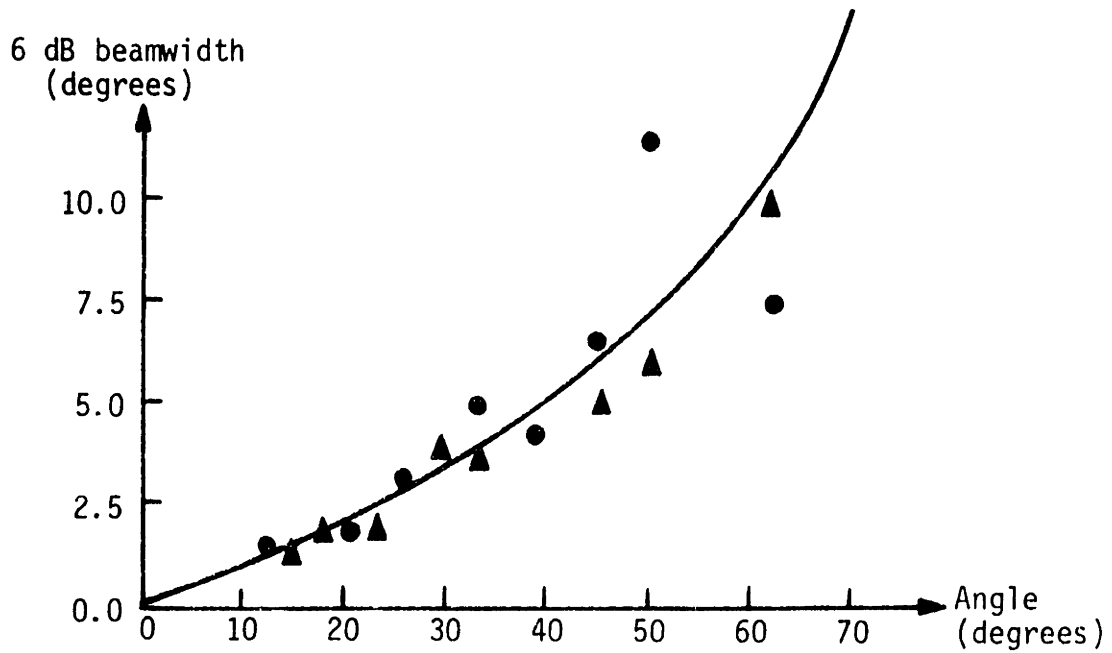

Figure 5-15a. Thick transducers. Theoretical curve: solid line; Experimental data: ● transducer B (PZT-5A), ▲ transducer D (lead metaniobate).
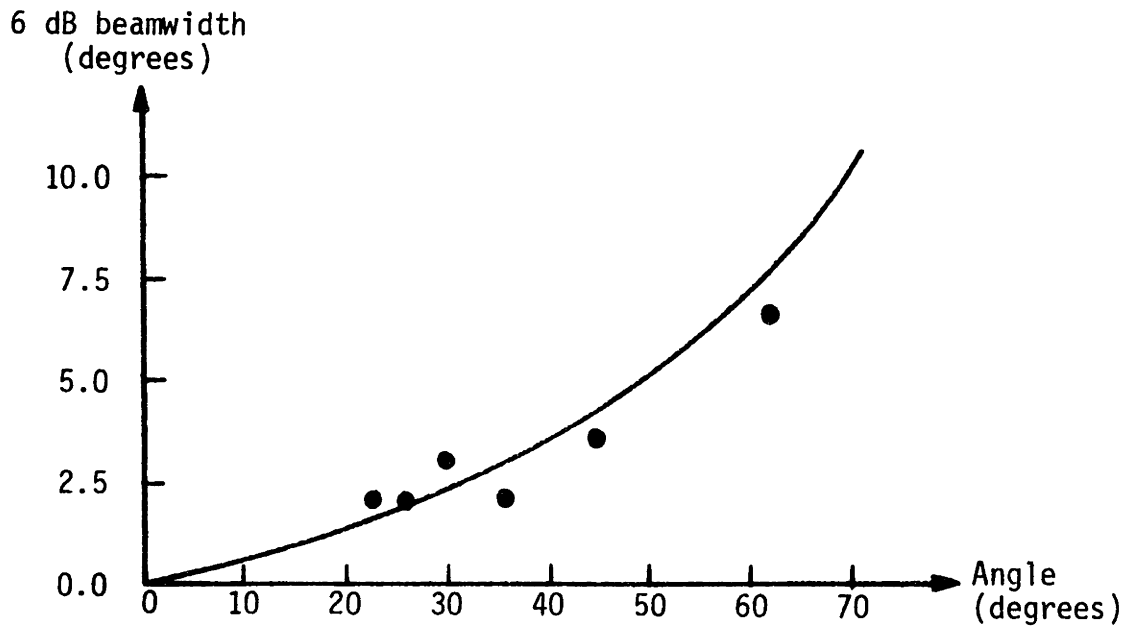
6 dB beamwidth
(degrees)

Figure 5-15b. Thin transducers. Theoretical curve: solid line; Experimental data: ● transducer A (PZT-5A).

Figure 5-15. Half-amplitude beamwidth versus center angle of transducer primary radiation lobe.

several frequencies. Note that the thick and thin transducers require separate theoretical curves because these transducers have different radiating surface areas (see Table 5-1).

Figures 5-12 and 5-15 demonstrate that the beamwidth and beam direction of the primary radiation lobe of the experimental transducers is accurately predicted by the theory of Chapters 2 and 3. To test the qualitative discussion of substrate dynamics presented in Chapter 4, we consider the spurious transducer radiation lobes. For this study it proves useful to plot the amplitude of the target echo, $V_r(\theta)$, on logarithmic coordinates in order that both large and small radiation lobes will be clearly visible.

In Section 4-2.1 we predicted that the homogeneous substrate response of a thin transducer would produce a single spurious radiation lobe located at a frequency-independent angle. We also predicted a resonance for this homogeneous radiation lobe at the same frequency as the primary-lobe resonance; from Eqs. (4-1), (4-5) and (2-20), these resonances occur precisely as the primary lobe "steers through" the spurious lobe. These predictions are supported by the sequence of plots of Figs. 5-16a, 5-16b and 5-16c, which show $V_r(\theta)$ for thin transducer A at three successive frequencies. Notice the simultaneous resonant peaking of the primary and spurious lobes as the two lobes merge.

Figures 5-17a, 5-17b and 5-17c are plots of $V_r(\theta)$ for thick transducer D at three successive frequencies. The spurious lobes indicated in Fig. 5-17a appear to have moved to the right in Fig. 5-17b, where they remain with increasing frequency as shown in Fig. 5-17c. This behavior is consistent with the discussion in Section 4-3 of the spurious lobes from high-order substrate wave modes in thick transducers.
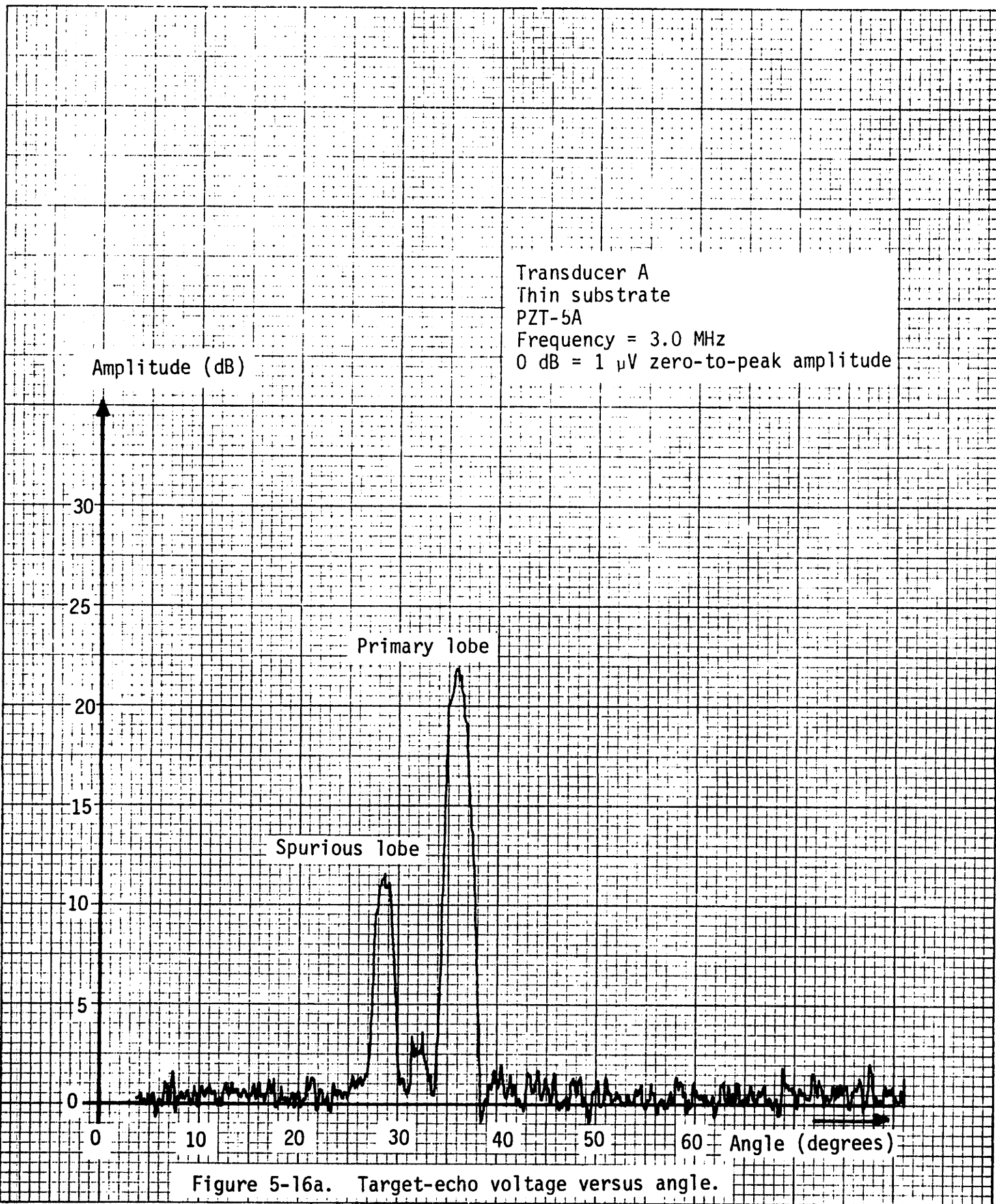
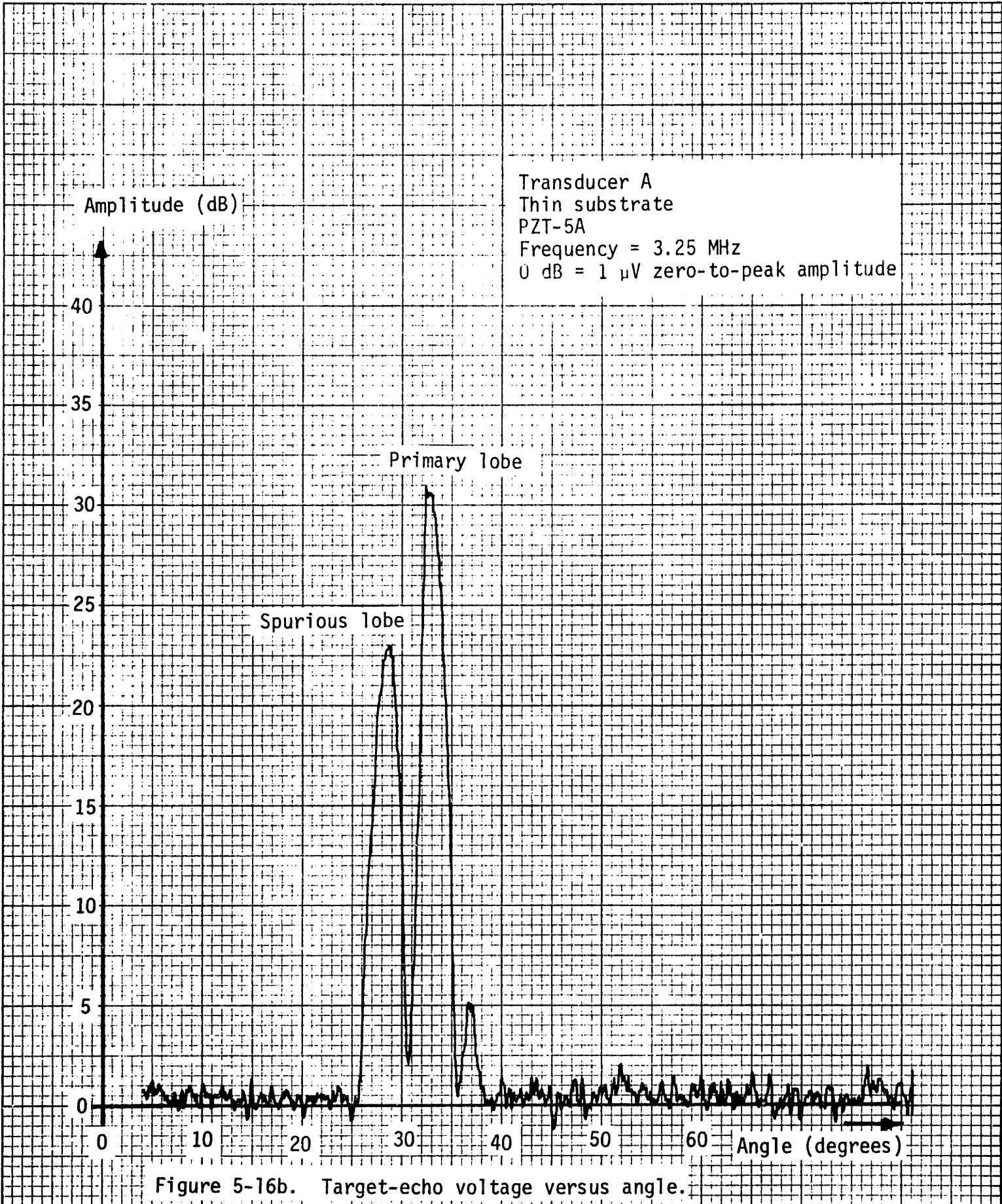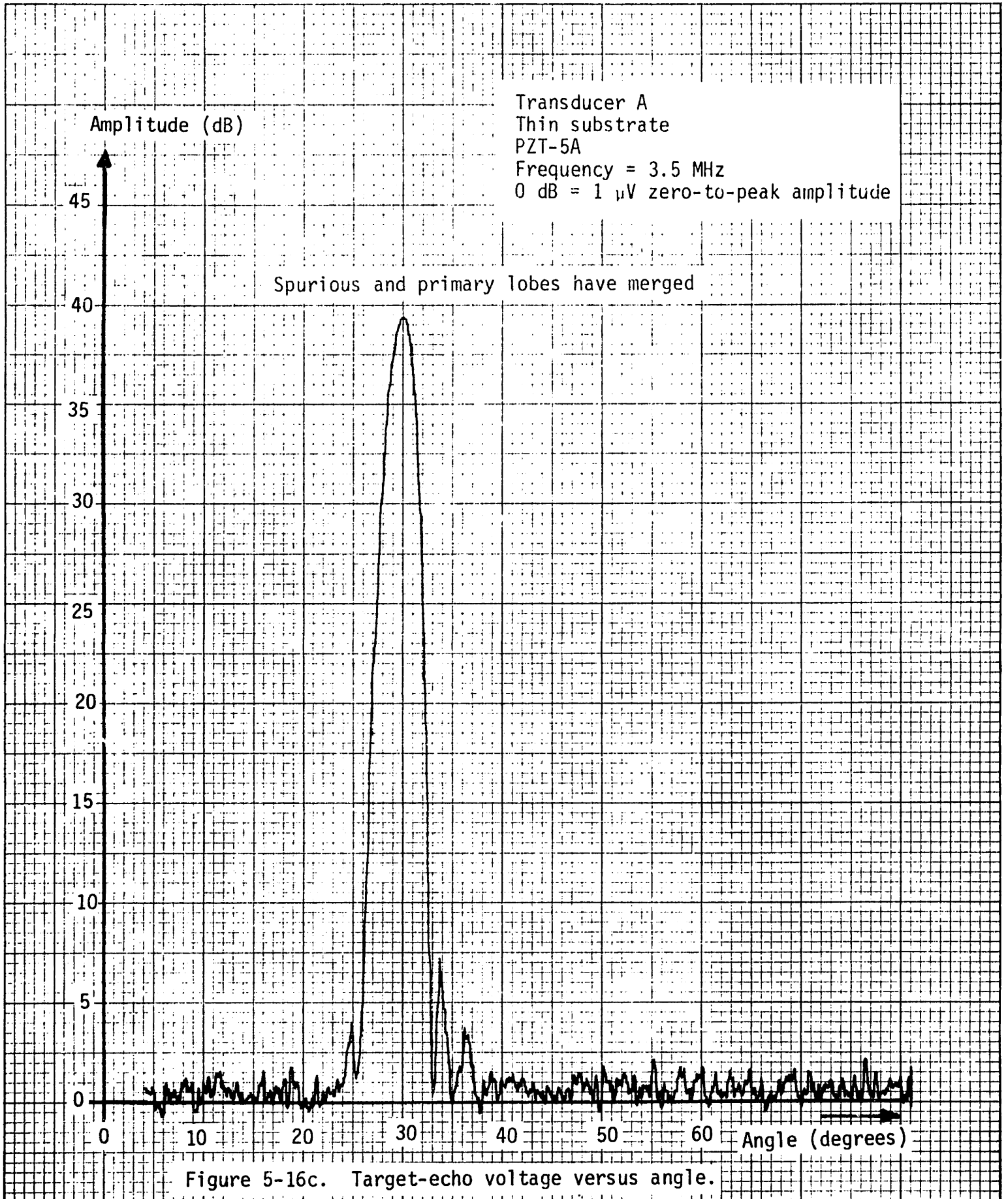Figure 5-16a. Target-echo voltage versus angle.

Figure 5-16b.   Target-echo voltage versus angle.

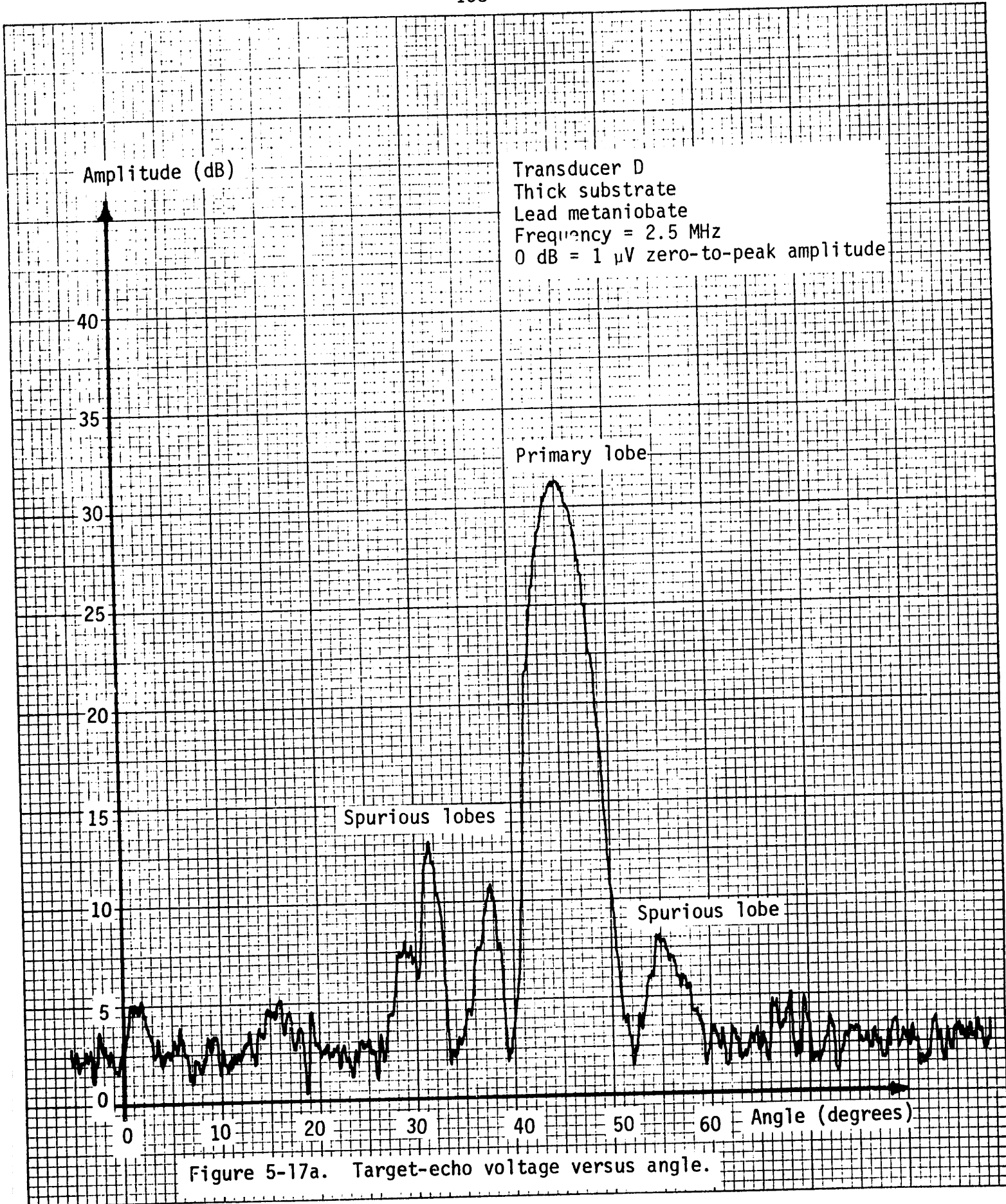Figure 5-16c.   Target-echo voltage versus angle.

Figure 5-17a. Target-echo voltage versus angle.

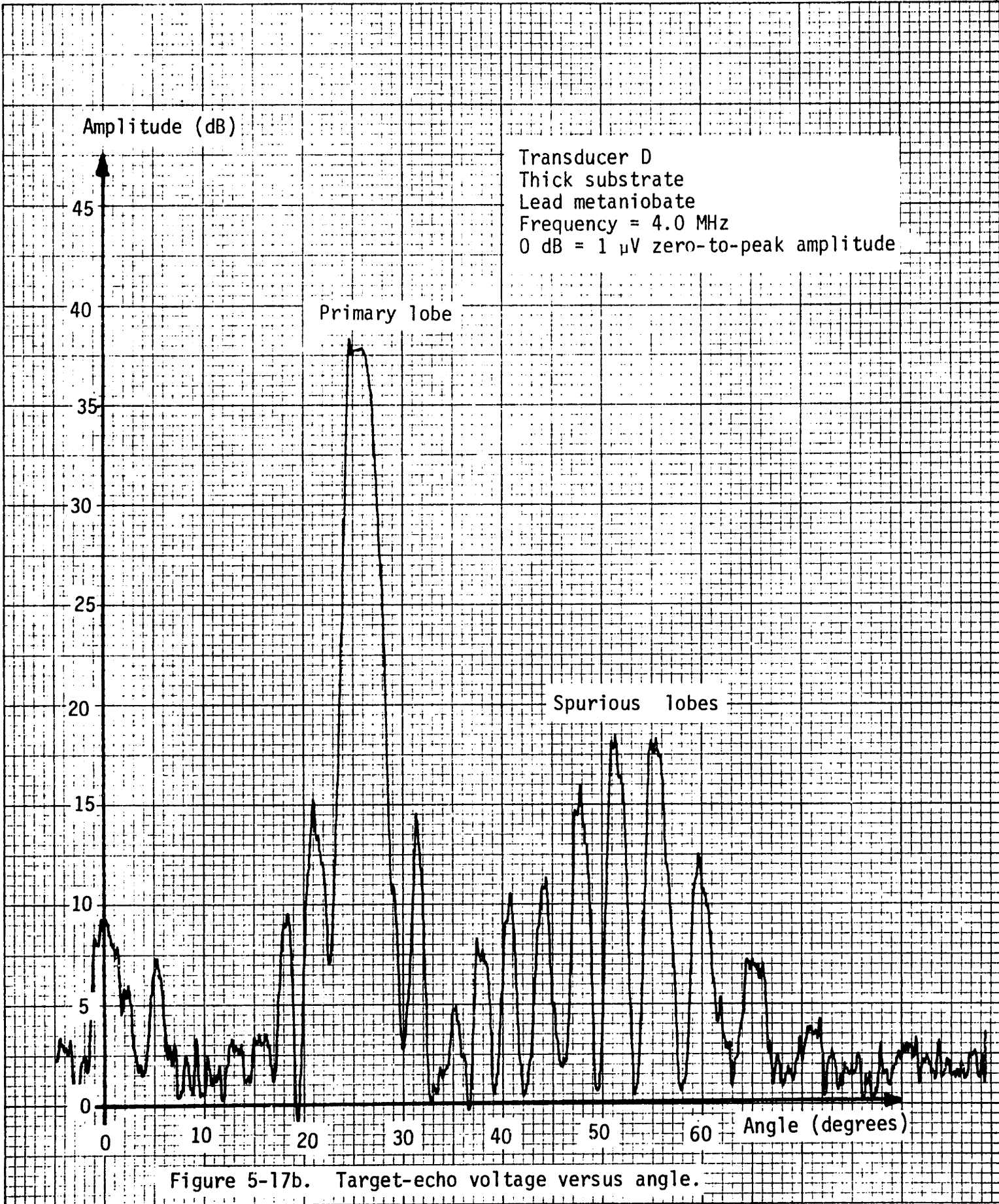Figure 5-17b.   Target-echo voltage versus angle.

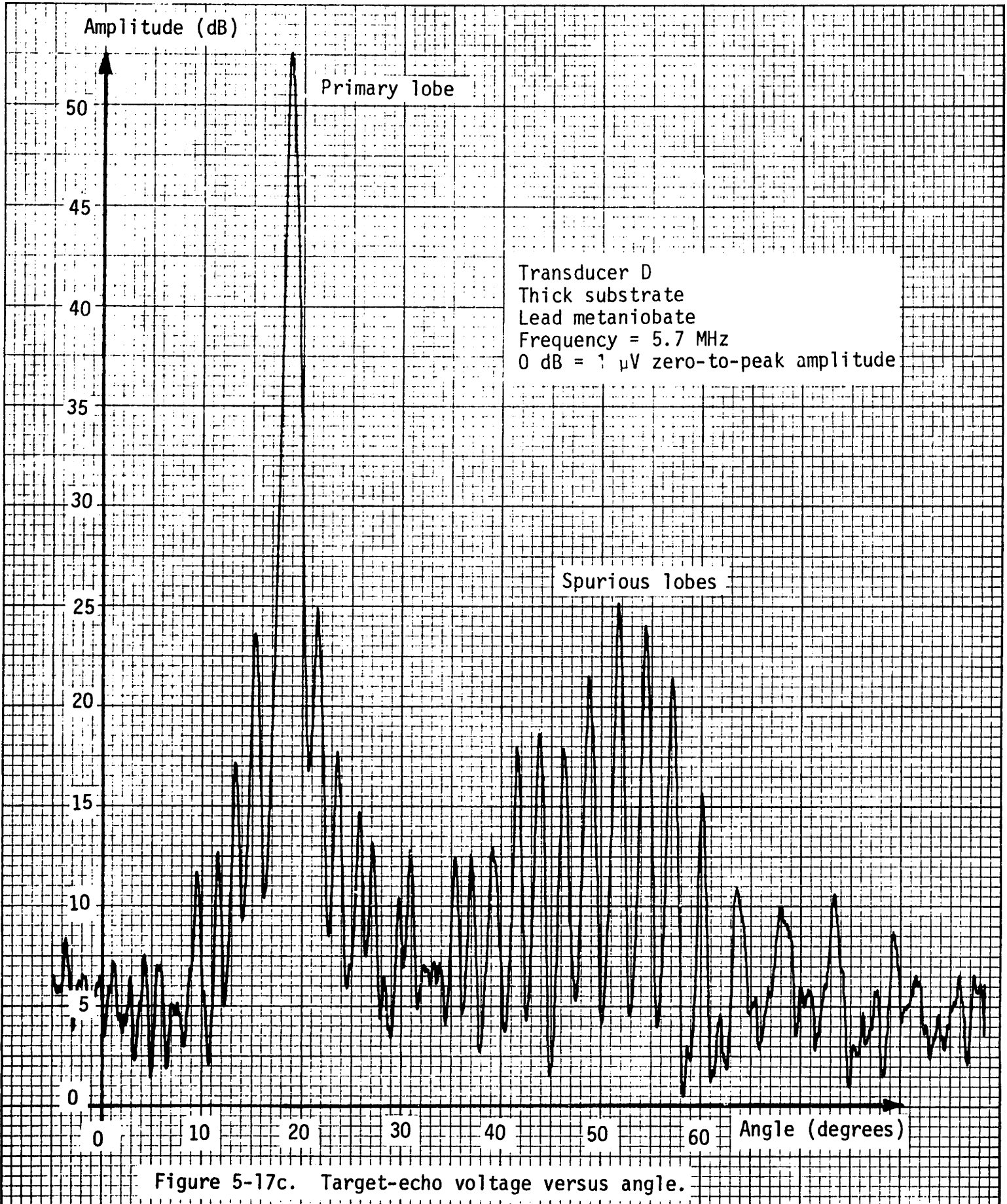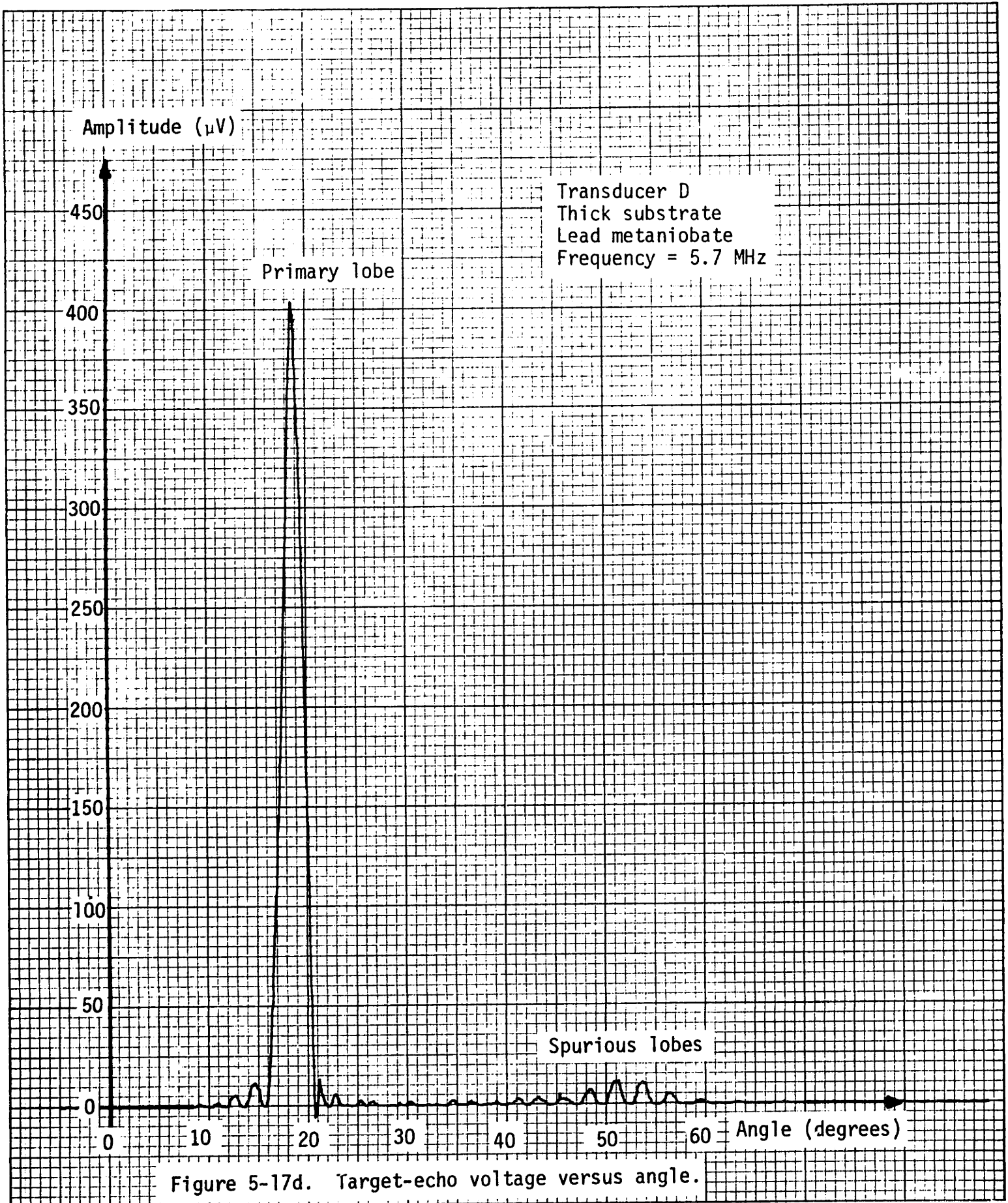Figure 5-17c. Target-echo voltage versus angle.

Figure 5-17d. Target-echo voltage versus angle.

The multiple side lobes immediately adjacent to the primary radiation lobe in Fig. 5-17c should not be confused with spurious radiation lobes due to homogeneous substrate wave modes. The side lobes are due to the finite aperture of the transducer as discussed in Section 3-1. Notice that the first pair of side lobes are down 28 dB from the primary lobe maximum, compared to 26 dB from the $\left(\frac{\sin x}{x}\right)^2$ intensity distribution calculated in Section 3-1. Finite aperture also accounts for the periodic structure superimposed on the spurious radiation lobes in Fig. 5-17c, where multiple spurious lobes and their side lobes appear together.

Figure 5-17d is a plot of the same data as shown in Fig. 5-17c, except Fig. 5-17d provides a linear scale for the target echo, $V_r(\theta)$. This plot is included to illustrate the side-lobe enhancement provided by the logarithmic scale of Fig. 5-17c compared to Fig. 5-17d.

In Chapter 2 we discuss spurious radiation lobes produced by spatial harmonics in the expansion (2-11) for $\delta(y)$. The frequency range (2-19), over which radiation can occur from only the first term in the expansion for $\delta(y)$, extends from 1.8 MHz to 5.3 MHz. Therefore at frequencies greater than 5.3 MHz, we may find spurious radiation from the third term in the expansion (2-11) for $\delta(y)$. Figures 5-18a and 5-18b are plots of $V_r(\theta)$ for thin transducer C at 6.0 MHz and 9.0 MHz respectively. According to Eq. (2-22), radiation from the third term in (2-11) should occur at 62.1° and 36.1° respectively, and inspection of Fig. 5-18 indeed reveals spurious radiation lobes at these frequencies.

Thick transducers B and D satisfy condition (4-10) for the elimination of the third harmonic in the summation (2-11) for $\delta(y)$; for these transducers the range for radiation from only the first term of (2-11) should extend from 1.8 MHz to 8.8 MHz. The experimental study of these
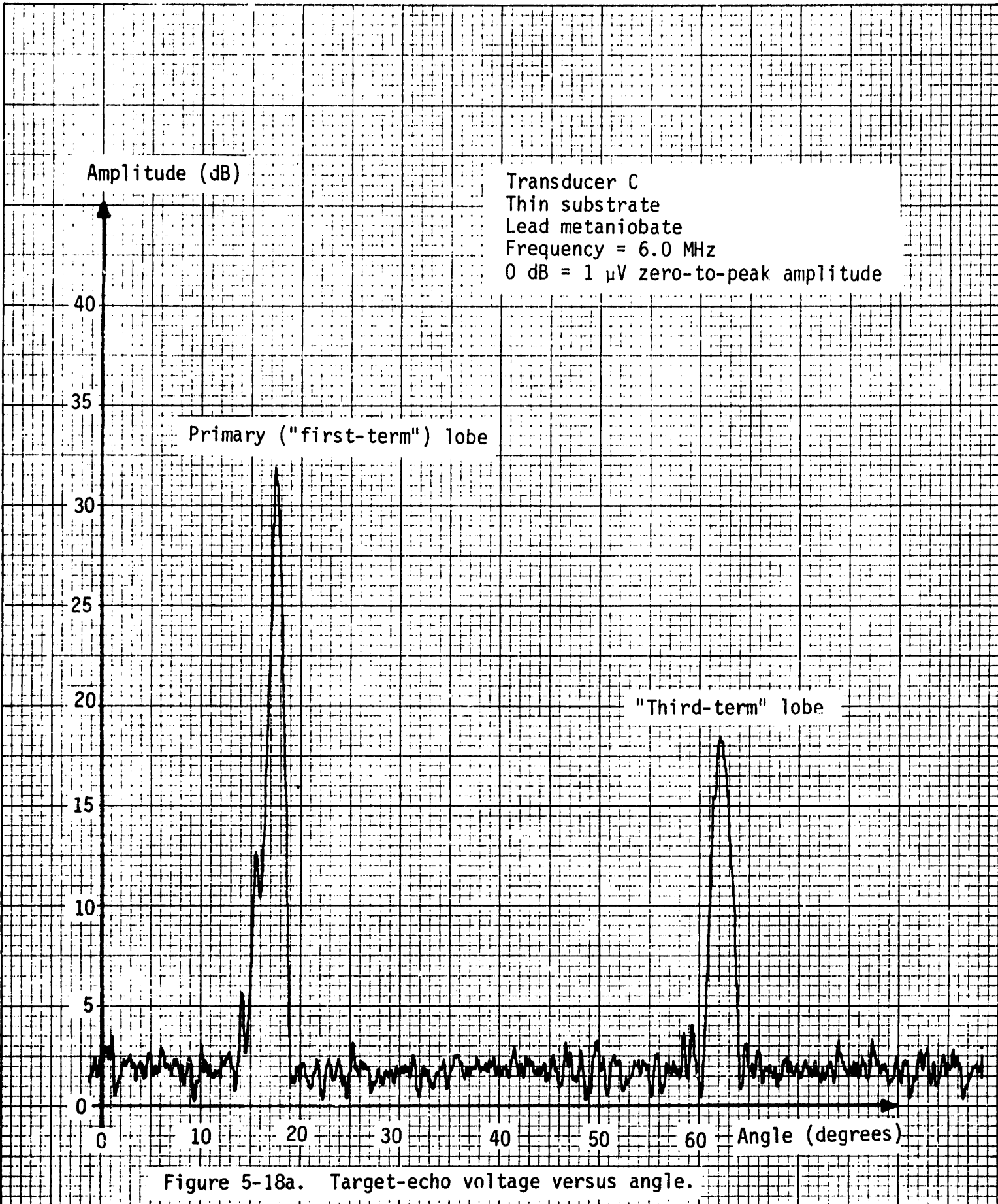
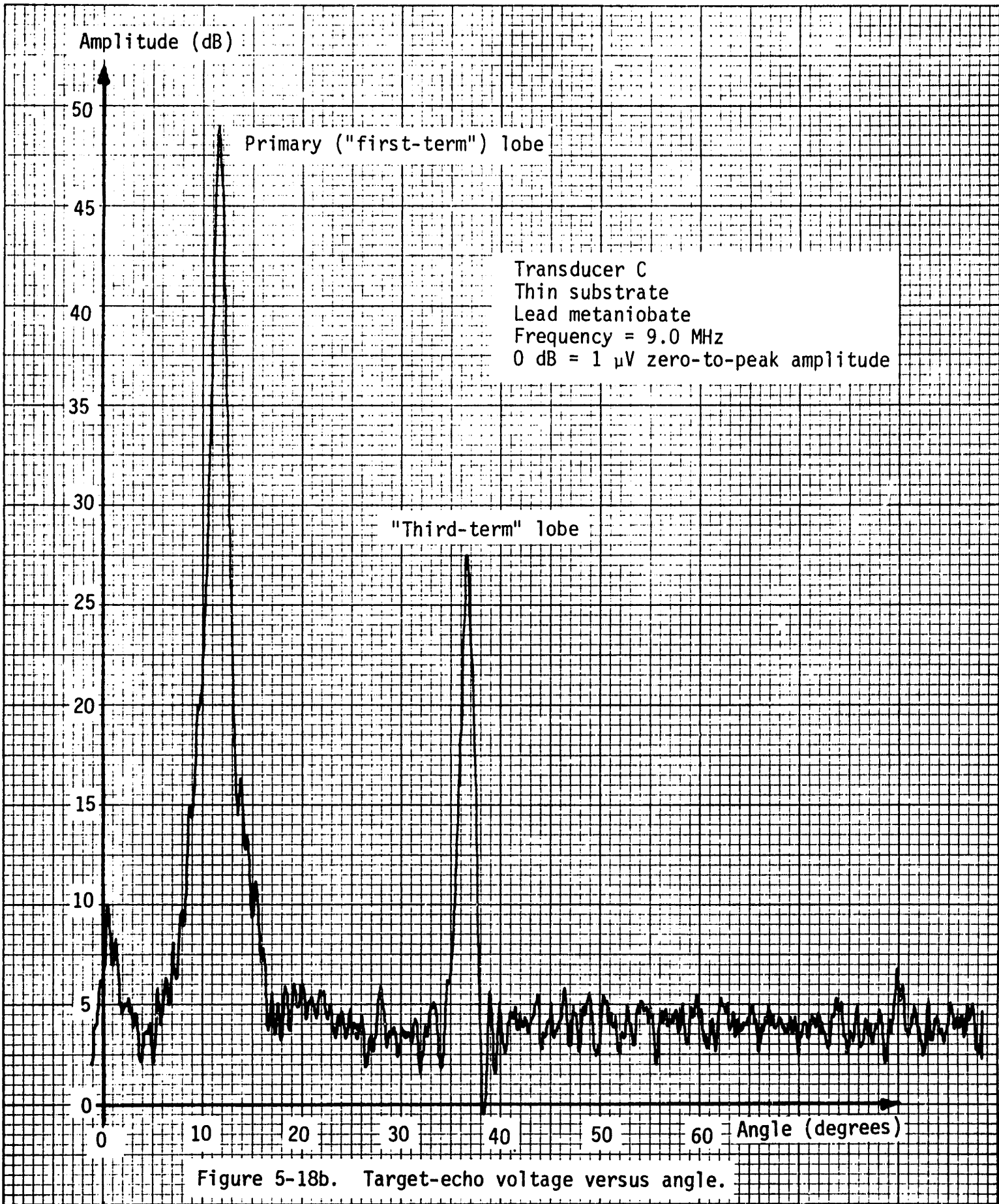Figure 5-18a. Target-echo voltage versus angle.

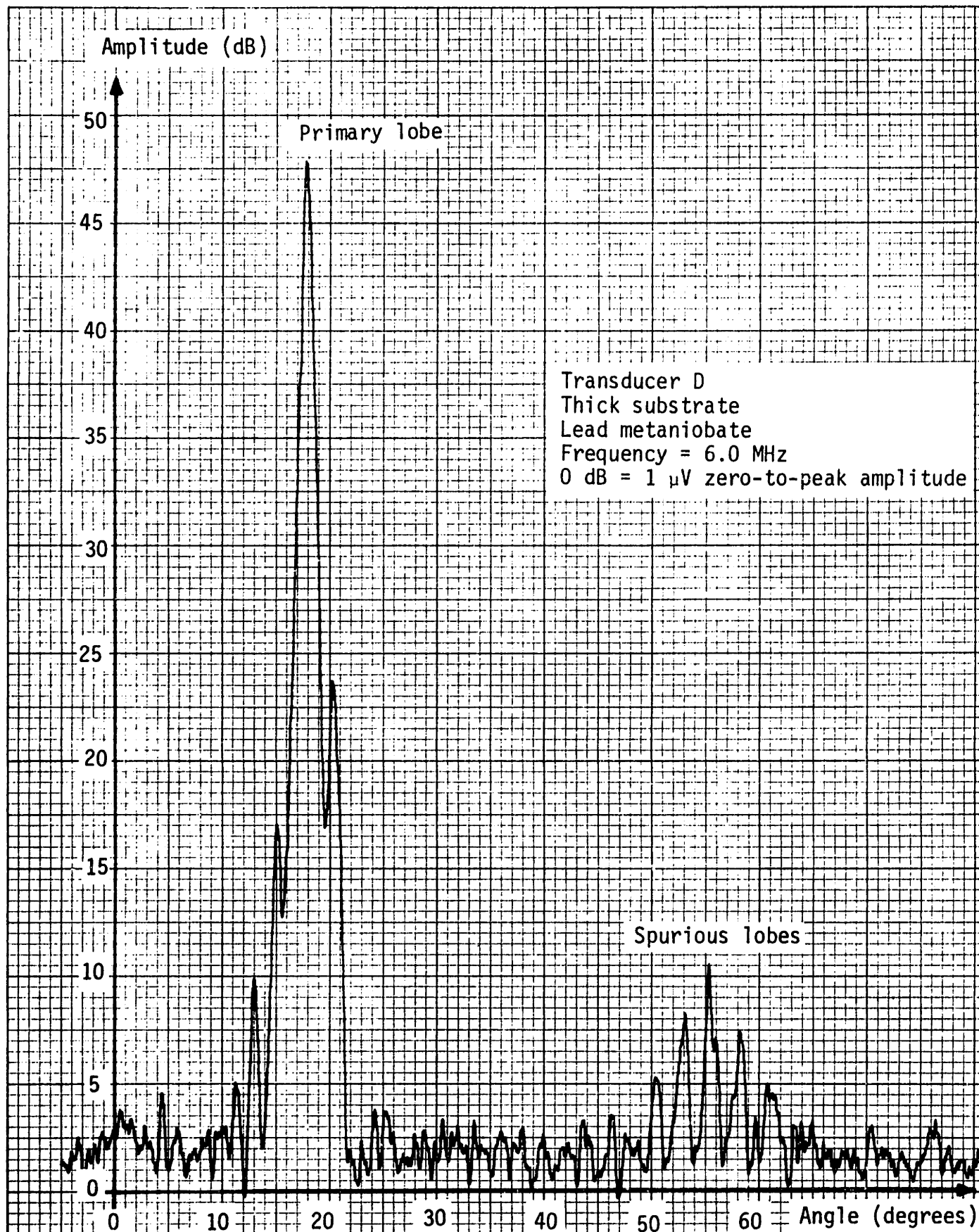Figure 5-18b. Target-echo voltage versus angle.

transducers revealed no sign of spurious radiation from the third harmonic of (2-11). For example, Figs. 5-19a and 5-19b contain plots of $V_r(\theta)$ for thick transducer D at 6.0 MHz and 9.0 MHz respectively, and no third-term spurious radiation lobes appear, although spurious lobes due to the substrate homogeneous response do occur in Fig. 5-19a in the vicinity of $\theta = 55°$.

The absence of third-term spurious radiation lobes in Fig. 5-19 may be contrasted with the situation in Fig. 5-18. However, while transducers C and D used to obtain Figs. 5-18 and 5-19 respectively were both fabricated on lead metaniobate substrates, the comparison of Figs. 5-18 and 5-19 does not constitute a controlled experiment for verifying Eq. (4-9) because transducers C and D differ in substrate thickness and in total number of finger pairs in addition to their differences in the ratio of finger width to electrode spacing. Nonetheless, the comparison of Figs. 5-18 and 5-19 provides strong support for the elimination of third-term spurious radiation lobes through optimum selection of the ratio of electrode finger width to periodic electrode spacing as specified in Eq. (4-9).

We argued in Chapter 4 that by introducing substrate loss, the amplitude of spurious radiation lobes due to homogeneous substrate modes should be reduced compared to the primary radiation lobe. We also suggested that substrate loss would smooth the sharp resonant peaks in the frequency response of the primary radiation lobe. No serious experimental study of these phenomena has been conducted, but one preliminary result is available.

A transducer, which we shall call B´, was fabricated on a PZT-5A substrate having the same dimensions as transducer B and using the same electrode mask as transducer B. In fact, the substrates for transducers B and B´ were cut from the same compressional-mode disc transducer, but

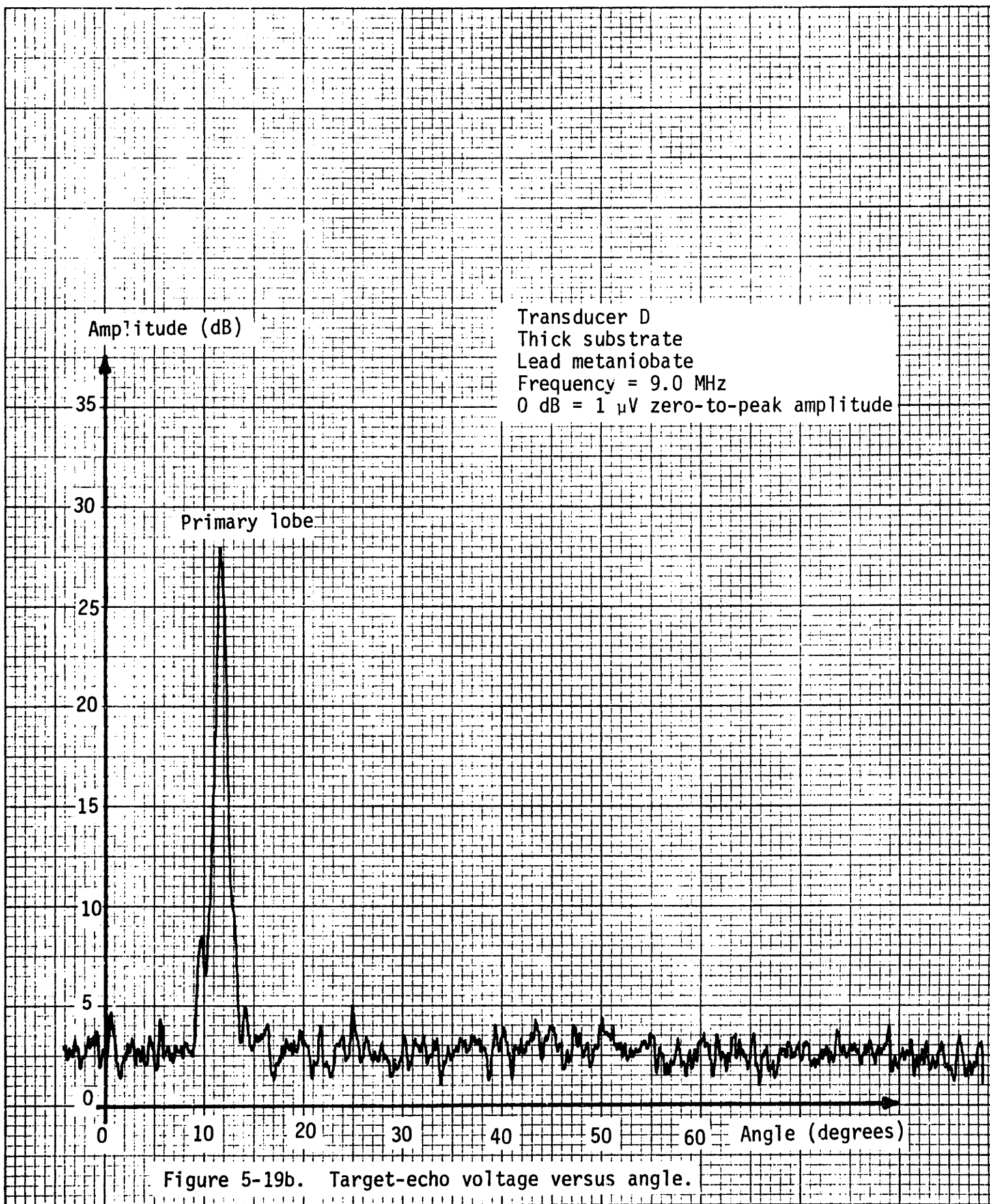Figure 5-19a. Target-echo voltage versus angle.

Figure 5-19b. Target-echo voltage versus angle.

after fabrication, the back face of transducer B´ was coated with a 0.5 inch-thick coating of tungsten-loaded epoxy.* Such coatings have been applied to conventional thickness mode transducers to provide mechanical damping[6]. By extrapolating data provided by Lutsch[32], the characteristic impedance of the coating was estimated at 7.5×10^3 kg/m^{2}s. This impedance compares with 1.5×10^3 kg/m^{2}s for water and 28 kg/m^{2}s for the compressional mode in PZT-5A. Thus, the lossy coating provides a load five times greater than water, but the coating must still be considered only "light-to-moderate" loading for PZT-5A.

Figure 5-20 presents a sequence of one-quadrant plots of $V_r(\theta)$ for transducer B´ with frequency as a parameter. A comparison of Fig. 5-20 with Fig. 5-11 (for transducer B) reveals reduced resonant peaking of the primary lobes in Fig. 5-20 and reduced spurious-lobe levels relative to the primary-lobe levels in Fig. 5-20 compared to Fig. 5-11. Indeed, the ratio of spurious-to-primary lobe amplitudes and the amount of resonant peaking in Fig. 5-20 are comparable to the levels found in Fig. 5-10 for lead metaniobate, a material with low intrinsic mechanical Q_m.

Transducers B and B´ both experienced their strongest resonances at 4.0 MHz, which is not unexpected due to their similarity in construction. However, Figs. 5-21a and 5-21b show drastic differences in the levels of spurious radiation lobes for the two transducers, especially considering that $V_r(\theta)$ is plotted on logarithmic coordinates in these figures.

---

* This coating was prepared by Theodore L. Rhyne, currently a graduate student in the Department of Electrical Engineering at M.I.T. The coating is a mixture with the following proportions (supplied by T. L. Rhyne):

> 3 cc (packed) ... powdered tungsten
> 6 cc ... Araldite epoxy 502 (Ciba-Geigy Corporation, Ardsley, New
> York)
> 0.6 cc Araldite hardener 951 (Ciba-Geigy Corporation, Ardsley,
> New York).
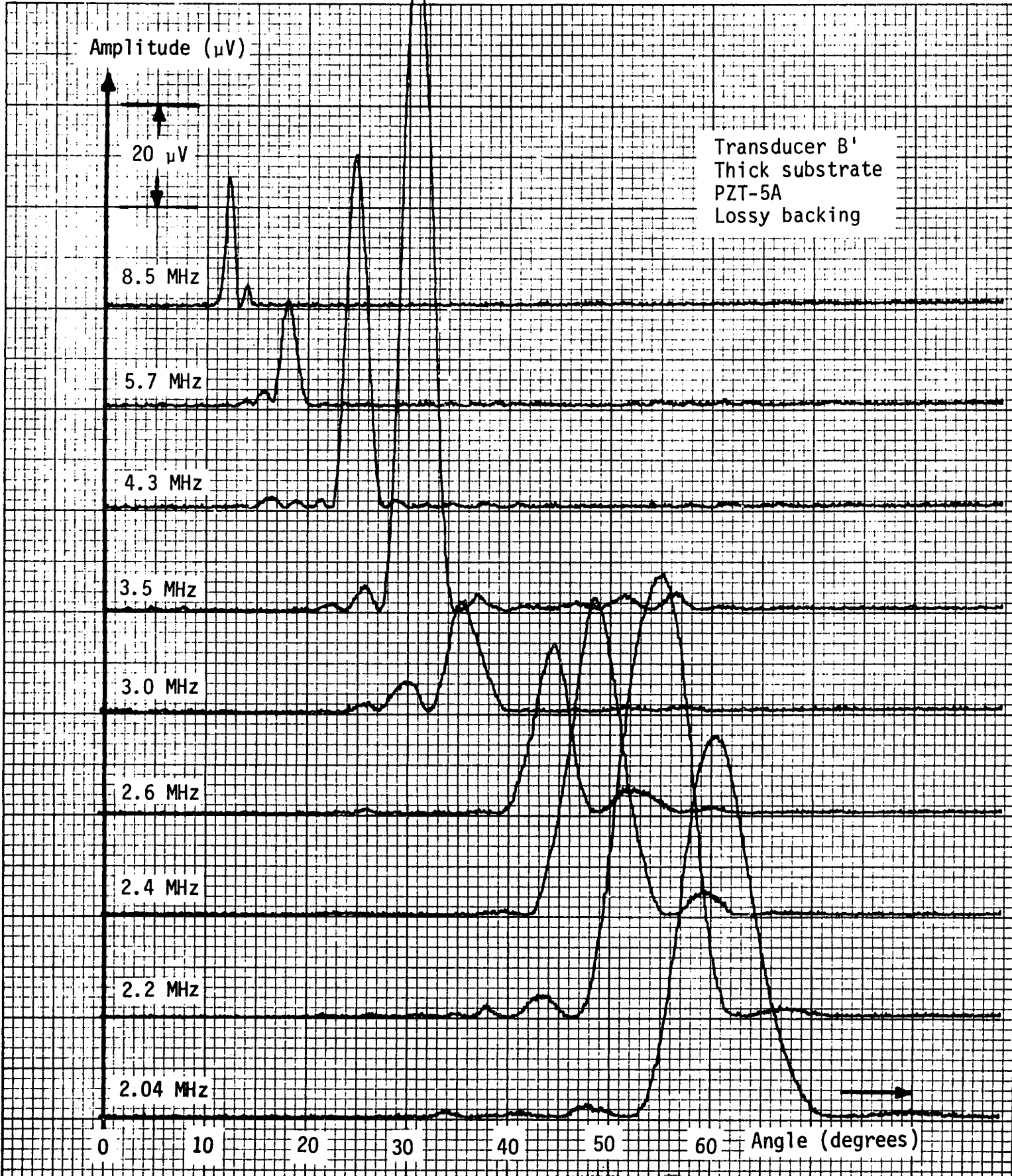
Figure 5-20. Superimposed plots of target-echo voltage versus angle for a sequence of frequencies.

Figure 5-21a.   Target-echo voltage versus angle.
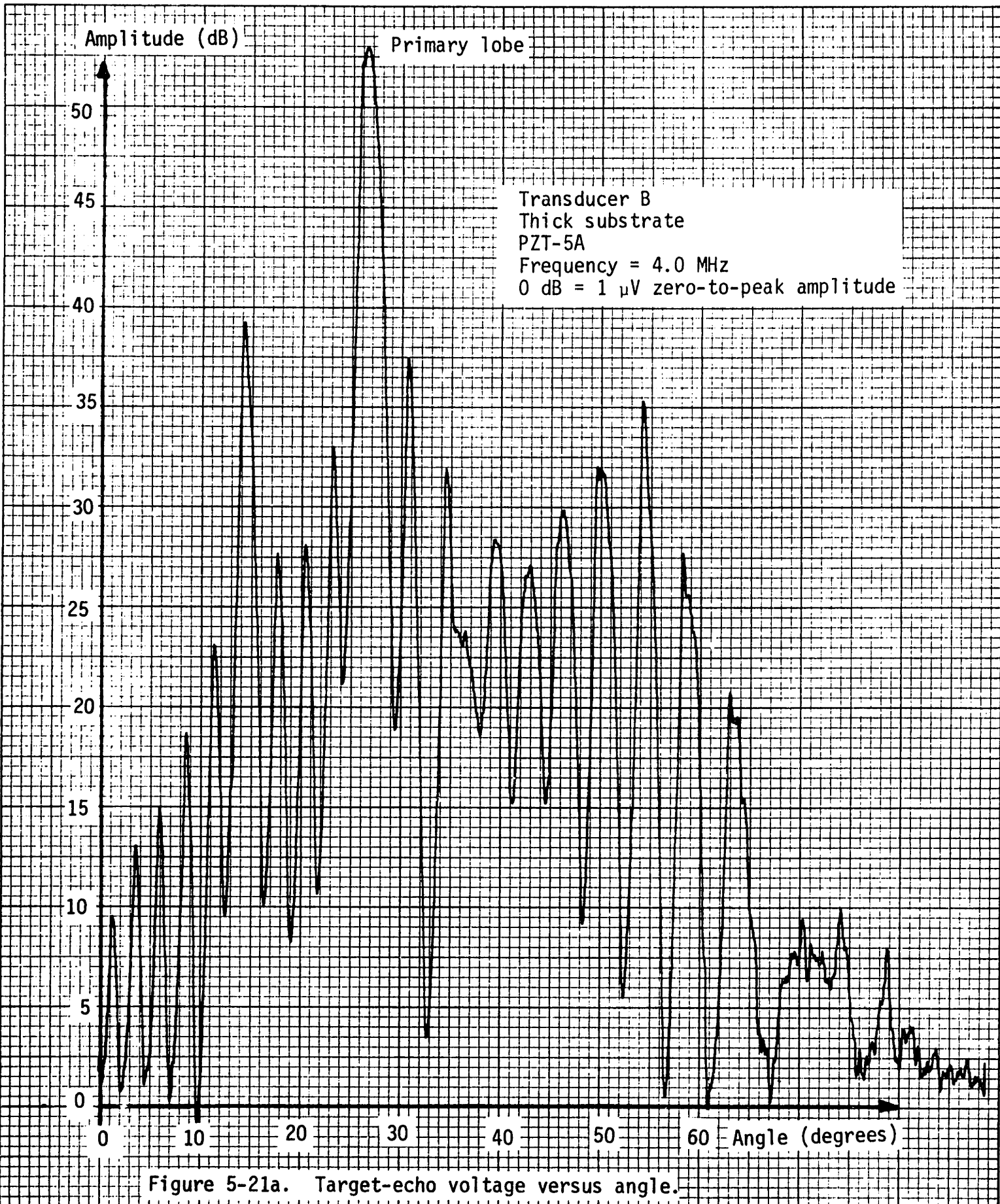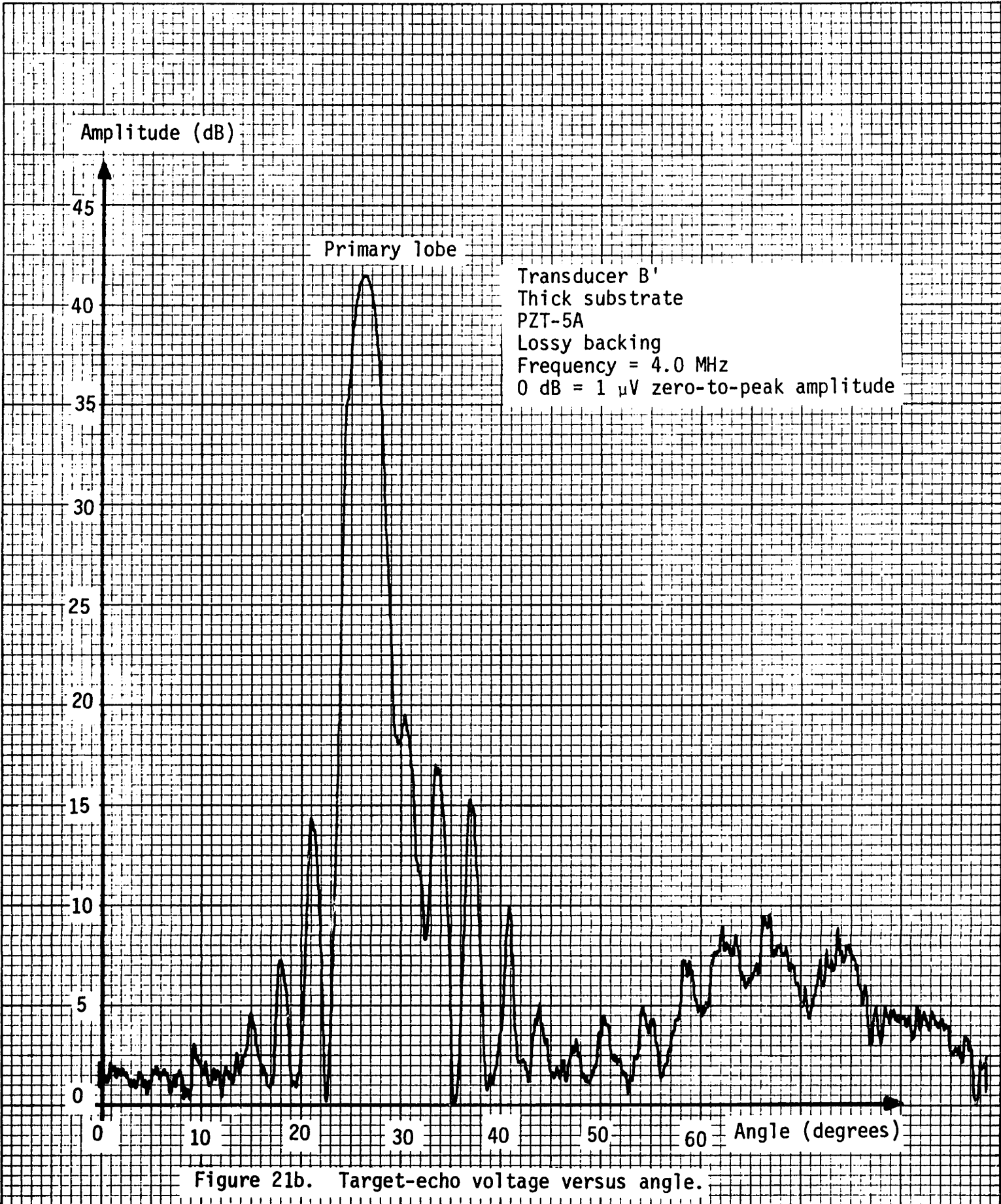
Figure 21b.   Target-echo voltage versus angle.

It is tempting to conclude that the difference in spurious-lobe levels in Figs. 5-21a and 5-21b is due in large part to the introduction of substrate loss to transducer B´ by the application of the lossy backing, and that the improvement in Fig. 5-20 compared to 5-11 is similarly due to the substrate loss of transducer B´. Unfortunately, the comparison of transducers B and B´ is not a controlled experiment such as would be accomplished, for example, by the comparison of the performance of transducer B´ before and after the application of its lossy coating. Nonetheless, the comparison of transducers B and B´ constitutes strong preliminary evidence for the effectiveness of substrate loss in improving transducer performance as described in Chapter 4.

Chapter 6

SUMMARY AND SUGGESTIONS FOR FUTURE RESEARCH

This report has described a new type of electronically steered ultrasonic transducer that is well-suited for operation at submillimeter wavelengths such as used in medical ultrasonic applications. Experimental transducers have been constructed and tested; their measured performance is in good agreement with the theory developed in this report.

The most important practical advantages of the new type of transducer are:

1. The transducer is easy to drive and steer because it is a frequency-scanned device possessing only a single pair of electrical terminals.

2. The transducer is fabricated by depositing an interdigitated electrode structure on a continuum piezoelectric substrate. Standard photo-lithographic techniques developed for integrated circuits are used for transducer construction; no grooving, etching or machining of the substrate is required. This fabrication procedure results in a transducer which can be reliably and economically produced.

3. The directivity of the transducer radiation is essentially diffraction limited, just as is true of the piston transducers commonly used in ultrasonics. Therefore, the transducer can be made as directive as desired simply by increasing its size.

The most important topics for future research involve continued study of substrate dynamics, a subject considered in Chapter 4 of this report. The object of continued research would be to find effective ways to attenuate the "natural" substrate wave modes which are excited at the transducer boundaries. These wave modes can produce spurious acoustic radiation, and they account for resonant peaks in the frequency response of the primary transducer radiation lobe.

Several proposals for future investigation of substrate dynamics are presented in Chapter 4, and a technique for introducing substrate loss by coating the back face of the transducers with acoustically lossy material is suggested for attenuating the natural substrate wave modes. Preliminary experimental results of this technique discussed in Chapter 5 are highly encouraging. Two additional suggestions for dealing with "natural" substrate wave modes are:

1. Transducers could be fabricated on circular, rather than rectangular, substrates in an attempt to "defocus" the natural substrate waves produced at the transducer edges. While this procedure would not attenuate the waves, it might spread any spurious radiation from them over a broad area, and therefore reduce the amplitude of the spurious radiation compared to the primary lobe radiation.

2. Techniques might be found to modify the production of ferroelectric ceramic materials in order to introduce intrinsic mechanical loss. For example, lead metaniobate has an intrinsic mechanical Q_m on the order of ten. Experimental measurements concerning transducer D presented in Chapter 5 suggest that this amount of intrinsic loss is already sufficient to produce transducers of practical value. However, even better performance might be forthcoming if the mechanical Q_m could be reduced to the range $3 < Q_m < 5$.

The experimental transducers evaluated in Chapter 5 were not designed for use in any clinical system, rather they were prototypes constructed to test the theory of operation developed in this report. Nonetheless, the measured performance of two of these devices (transducers B' and D) suggests that they could find immediate practical use in many of the pulse-echo medical applications discussed in Chapter 1. Both transducers used "thick" substrates, in the sense that the compressional mode resonance

frequency of the substrates were within the range specified in Eq. (2-19). Both transducer substrates also possessed moderate amounts of mechanical loss (which was deliberately introduced in the case of transducer B'). These features apparently account for the observed good performance of the two transducers. But independent of any immediate practical value of these specific transducers, it seems clear that the new electronically steered ultrasonic transducer is a device which deserves further investigation and development.

REFERENCES

1. P.N.T. Wells, _Physical Principles of Ultrasonic Diagnosis_. New York: Academic Press, 1969.

2. D. L. Franklin, W. Schlegel, R. F. Rushmer, "Blood Flow Measured by Doppler Frequency Shift of Back-Scattered Ultrasound," _Science_, Vol. 134, pp. 564-565, Aug. 1961.

3. D. W. Baker, "Pulsed Ultrasonic Doppler Blood-Flow Sensing," _IEEE Trans. Sonics Ultrason._, Vol. SU-17, pp. 170-185, July 1970.

4. W. R. Brody, _Theoretical Analysis of the Ultrasonic Blood Flowmeter_, Technical Report No. 4953-1, Stanford Electronics Laboratories, Stanford, Calif., Oct. 1971.

5. M. P. Fraser, _Transcutaneous Spectral Blood-Flowmeter_, Technical Note 1970-7, M.I.T. Lincoln Laboratory, Lexington, Mass., Mar. 1970.

6. G. Kossoff, "The Effects of Backing and Matching on the Performance of Piezoelectric Transducers," _IEEE Trans. Sonics Ultrason._, Vol. SU-13, pp. 20-30, Mar. 1966.

7. D. A. Berlincourt, D. R. Curran, and H. Jaffe, "Piezoelectric and Piezomagnetic Materials and Their Function in Transducers," in _Physical Acoustics_, _Part IA_, W. P. Mason ed. New York: Academic Press, 1964.

8. J. C. Somer, "Electronic Sector Scanning for Ultrasonic Diagnosis," _Ultrasonics_, pp. 153-159, July 1968.

9. R. L. Cook, "Experimental Investigation of Acoustic Imaging Sensors," _IEEE Trans. Sonics Ultrason._, Vol. SU-19, pp. 444-447, Oct. 1972.

10. M. Pappalardo, "Transducer Line-Arrays in the High-Frequency Range," _Ultrasonics_, pp. 77-82, Mar. 1973.

11. O. T. Von Ramm, _A Real Time Digitally Controlled Ultrasound Imaging System_, Ph.D. Dissertation, Duke University, 1973.

12. W. H. Von Aulock, "Properties of Phased Arrays," _Proc. IRE_, pp. 1715-1727, Oct. 1960.

13. M. Skolnik, _Radar Systems_. New York: McGraw-Hill Book Co., 1962, Chapter 7.

14. C. Hartmann, W. Jones, and H. Vollers, "Wideband Unidirectional Interdigital Surface Wave Transducers," _IEEE Trans. Sonics Ultrason._, Vol. SU-19, pp. 378-381, July 1972.

15. B. Gold and C. Rader, _Digital Processing of Signals_. New York: McGraw-Hill Book Co., 1969, Chapter 6.

16. J. F. Nye, _Physical Properties of Crystals_. Oxford: Clarendon Press, 1957.

17. R. Holland and E. EerNisse, _Design of Resonant Piezoelectric Devices_. Cambridge, Mass.: The MIT Press, 1969, Chapters 1 and 2.

18. "Standards on Piezoelectric Crystals, 1949," _Proc. IRE_, Vol. 37, pp. 1378-1395, Dec. 1949.

19. D. A. Berlincourt, "Piezoelectric Crystals and Ceramics," in _Ultrasonic Transducer Materials_, O. E. Mattiat ed. New York: Plenum Press, 1971.

20. J. J. Campbell and W. R. Jones, "A Method for Estimating Optimal Crystal Cuts and Propagation Directions for Excitation of Piezoelectric Surface Waves," _IEEE Trans. Sonics Ultrason._, Vol. SU-15, pp. 209-217, Oct. 1968.

21. W. Smith, H. Gerard, J. Collins, T. Reeder, and H. Shaw, "Analysis of Interdigital Surface Wave Transducers by Use of an Equivalent Circuit Model," _IEEE Trans. Microwave Theory Tech._, Vol. MTT-17, pp. 856-864 Nov. 1969, Appendix I.

22. H. Engan, "Excitation of Elastic Surface Waves by Spatial Harmonics of Interdigital Transducers," _IEEE Trans. Electron Devices_, Vol. ED-16, pp. 1014-1017, Dec. 1969.

23. E. Meyer and E. Neumann, _Physical and Applied Acoustics_. New York: Academic Press, 1972, Chapter I.

24. "IRE Standards on Piezoelectric Crystals: Determination of the Elastic, Piezoelectric, and Dielectric Constants -- The Electromechanical Coupling Factor, 1958," _Proc. IRE_, Vol. 46, pp. 764-778, April 1958.

25. "IRE Standards on Piezoelectric Crystals: Measurements of Piezoelectric Ceramics, 1961," _Proc. IRE_, Vol. 49, pp. 1161-1169, July 1961.

26. R. N. Thurston, "Effect of Electrical and Mechanical Terminating Resistances on Loss and Bandwidth According to the Conventional Equivalent Circuit of a Piezoelectric Transducer," _IRE Trans. on Ultrasonic Engineering_, pp. 16-25, Feb. 1960.

27. F. L. Thurstone, "Acoustical Imaging of Biological Tissue," _IEEE Trans. Sonics Ultrason._, Vol. SU-17, pp. 154-157, July 1970.

28. H. Seki, A. Granato and R. Truell, "Diffraction Effects in the Ultrasonic Field of a Piston Source and Their Importance in the Accurate Measurement of Attenuation," _J. Acoust. Soc. Am._, Vol. 28, pp. 230-238, Mar. 1956.

29. B. Auld, "Application of Microwave Concepts to the Theory of Acoustic Fields and Wave in Solids," _IEEE Trans. Microwave Theory Tech._, Vol. MTT-17, pp. 800-811.

30. P. Morse, Vibration and Sound. New York: McGraw-Hill Book Co., 1948, pp. 350-351.

31. G. Sabin, "Calibration of Piston Transducers at Marginal Test Distances," J. Acoustc. Soc. Am., Vol. 36, pp. 168-173, Jan. 1964.

32. A. Lutsch, "Solid Mixtures with Specified Impedances and High Attenuation for Ultrasonic Waves," J. Acoust. Soc. Am., Vol. 34, pp. 131-132, 1962.

33. R. Beyer and S. Letcher, Physical Ultrasonics. New York: Academic Press, 1969, pp. 12-16.

34. S. Rschevkin, The Theory of Sound. New York: Pergamon Press, 1963, pp. 419-426.

35. A. Bose and K. Stevens, Network Theory. New York: Harper and Row, 1965, pp. 312-316 and p. 349.

Appendix I

ACOUSTIC RADIATION FROM A PLANE "BOUNDARY WAVE"
OF SURFACE DEFORMATION

In this appendix we derive the acoustic radiation into a fluid generated by a plane boundary wave of surface deformation. The physical arrangement is shown in Fig. Al-1 where a half-space is filled with an ideal inviscid fluid and bounded by the infinite xy- plane at z=0. We assume that the normal component of displacement of the plane boundary, $\delta(y,t)$, is given by

$$\delta(y,t) = \Delta e^{j(\omega t - \beta y)} \tag{A1-1}$$

where Δ, β and ω are parameters. The tangential components of the boundary displacement are arbitrary.

It can be shown that the radiation into a fluid produced by an infinite plane boundary is uniquely determined by the normal component of displacement along that boundary.[33,34] Therefore, if we can present a solution for the acoustic radiation into the fluid that satisfies Eq. (A1-1) and the acoustic laws of the fluid, this solution must be the unique solution.

The acoustic laws for propagation in a fluid are[23]

$$\nabla p = -\rho \frac{\partial \vec{t}}{\partial t} \tag{A1-2}$$

and

$$\nabla \cdot \vec{v} = -\frac{1}{\rho c^2} \frac{\partial p}{\partial t} \tag{A1-3}$$

where p and $\vec{v}$ are respectively the acoustic pressure and particle velocity. Both fluid density ρ and sonic velocity c are constituent properties of the fluid medium. The only boundary condition is the requirement of continuity of the normal component of the particle velocity at the fluid boundary,
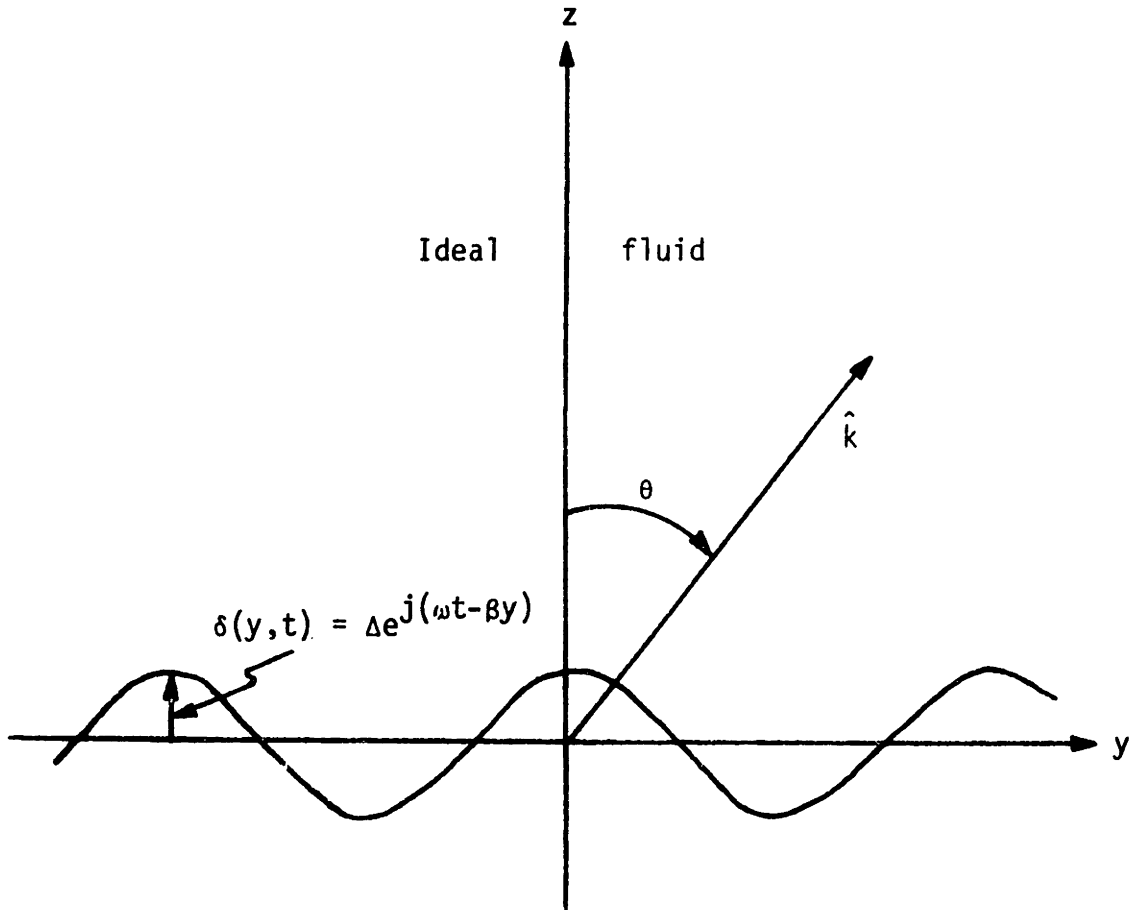
Figure A1-1. Half-space filled with ideal fluid and bounded by infinite plane boundary at z = 0.

$$\vec{v} \cdot \tau_z = \frac{\partial \delta(y,t)}{\partial t} \quad \text{at} \quad z = 0 \quad . \qquad \text{(A1-4)}^*$$

We present solutions for the radiation into the fluid for two cases. The reader may verify by direct substitution that the solutions satisfy Eqs. (A1-1) through (A1-4).

CASE 1: $\quad |\beta| < \frac{\omega}{c} \quad .$

Choose $\quad \theta , \quad -\frac{\pi}{2} < \theta < \frac{\pi}{2} , \quad$ such that

$$\beta = \frac{\omega}{c} \sin \theta \quad . \qquad \text{(A1-5)}$$

Then:

$$\vec{v} = j\omega\Delta(\tan\theta \ \tau_y + \tau_z) \ e^{j\left[\omega t - \frac{\omega}{c}(y \ \sin\theta + z \ \cos\theta)\right]} \qquad \text{(A1-6)}$$

$$p = \frac{j\omega\rho c\Delta}{\cos\theta} \ e^{j\left[\omega t - \frac{\omega}{c}(y \ \sin\theta + z \ \cos\theta)\right]} \quad . \qquad \text{(A1-7)}$$

Equations (A1-5), (A1-6) and (A1-7) define a longitudinal acoustic plane wave with pressure amplitude

$$p = \frac{j\omega\rho c\Delta}{\cos\theta} \qquad \text{(A1-8)}$$

and radiating in the direction $\hat{k}$

$$\hat{k} = \tau_y \ \sin\theta + \tau_z \ \cos\theta \quad . \qquad \text{(A1-9)}$$

The angle θ and unit propagation vector $\hat{k}$ are shown in Fig. (A1-1).

_____

*The symbols "τ_y" and "τ_z" are unit coordinate vectors in the y- and z-directions respectively.

CASE 2: $|\beta| > \frac{\omega}{c}$

Define $\alpha = \sqrt{\beta^2 - \frac{\omega^2}{c^2}}$ (A1-10)

Then:

$$\vec{v} = j\omega\Delta\left(j\frac{\beta}{\alpha}\tau_y + \tau_z\right) e^{-\alpha z} e^{j(\omega t-\beta y)} \qquad (A1-11)$$

and

$$p = -\frac{\rho\omega^2\Delta}{\alpha} e^{-\alpha z} e^{j(\omega t-\beta y)} \qquad . \qquad (A1-12)$$

Equations (A1-10), (A1-11) and (A1-12) describe an evanescent wave that decays exponentially with distance away from the boundary.

Notice that by not requiring continuity of tangential particle velocity at the fluid boundary, tangential "slip" of the boundary with respect to the fluid is allowed. However, for the practical case of a low (but non-zero) viscosity fluid, tangential slip is not possible. For this case, tangential boundary conditions may be satisfied by the generation of fluid shear waves in addition to the waves described above. These shear waves are analogous to the waves generated on the surface of a metal by high frequency electric currents. For frequencies in the range 1-10 MHz, the "skin depth" of a fluid shear wave in water is on the order of 10^{-6} meters. Such waves clearly have no significance in the radiation field of a medical ultrasonic transducer; this reasoning justifies our model of the transducer radiating into an ideal inviscid fluid.

Appendix II

DETAILED ANALYSIS OF THIN TRANSDUCER

The purpose of this appendix is to analyze the substrate dynamics of the thin transducer discussed in Section 4.2. Specifically, we consider the finite aperture thin transducer of Fig. A2-1, fabricated using a thin ferro-electric ceramic substrate with its axis of polarization parallel to the x_3-axis, and excited by sinusoidal steady-state voltage $V_0 e^{j\omega t}$. We derive analytic expressions for:

1. the normal component of substrate surface deformation, $\delta(y)$

2. the transducer terminal current, I

3. the Q of the fundamental resonance of the transducer (determined from energy loss due to acoustic radiation).

Due to the mathematical complexity in this appendix, we shall modify our notation to conform as closely as possible with the conventions set forth in the 1949 IRE Standards on Piezoelectric Crystals.[18] In particular, the following definitions apply:

$$u_i \ (i=1,2,3) \ = \ \text{material particle displacement} \tag{A2-1}$$

$$E_i \ (i=1,2,3) \ = \ \text{electric field} \tag{A2-2}$$

$$D_i \ (i=1,2,3) \ = \ \text{electric displacement} \tag{A2-3}$$

$$S_i \ (i=1...6) \ = \ \text{elastic strain} \tag{A2-4}*$$

$$T_i \ (i=1...6) \ = \ \text{elastic stress} \tag{A2-5}$$

$$\varepsilon_{ij}^T \ (i,j=1,2,3) \ = \ \text{dielectric permitivity at constant stress} \tag{A2-6}$$

---

* The strain components for i=1,2,3 are $S_i = \dfrac{u_i}{x_i}$, where x_i is the ith position coordinate.

$$d_{ij} \ (i=1,2,3; \ j=1\ldots6) \ = \ \text{piezoelectric strain constant} \quad (A2\text{-}7)$$

$$s_{ij}^E \ (i,j=1\ldots6) \ = \ \text{elastic compliance at constant electric field} \quad (A2\text{-}8)$$

The above quantities are related by the piezoelectric equations of state, given below in matrix form[16,17]

$$S \ = \ s^E T + d_t E \tag{A2-9}$$

$$D \ = \ dT + \epsilon^T E \tag{A2-10}$$

Consider the finite aperture "thin transducer" of Fig. A2-1, which radiates into an inviscid fluid. We make the following assumptions:

1. The width W of the substrate is so great that no appreciable substrate motion takes place in the $\pm \ x_1$ direction.

2. Stress-free boundary conditions exist at the substrate edges, $x_2 = \pm \frac{D}{2}$.

3. The substrate is sufficiently thin that electrical fringing fields can be neglected.

4. The transducer is so thin that mechanical stresses and strains in the substrate are independent of x_3.

5. The fluid is a light mechanical load for the substrate, so all stress components except T_1 and T_2 are zero.

Assumption 5 is motivated by the observation that the characteristic acoustic impedances of ferroelectric ceramics are more than ten times greater than that of water; the stress-free boundary conditions of assumption 2 are perhaps the easiest conditions to implement in practice.

Using the preceding assumptiosn and the symmetry properties of ferroelectric ceramics, the matrix piezoelectric equations (A2-9) and (A2-10) reduce to
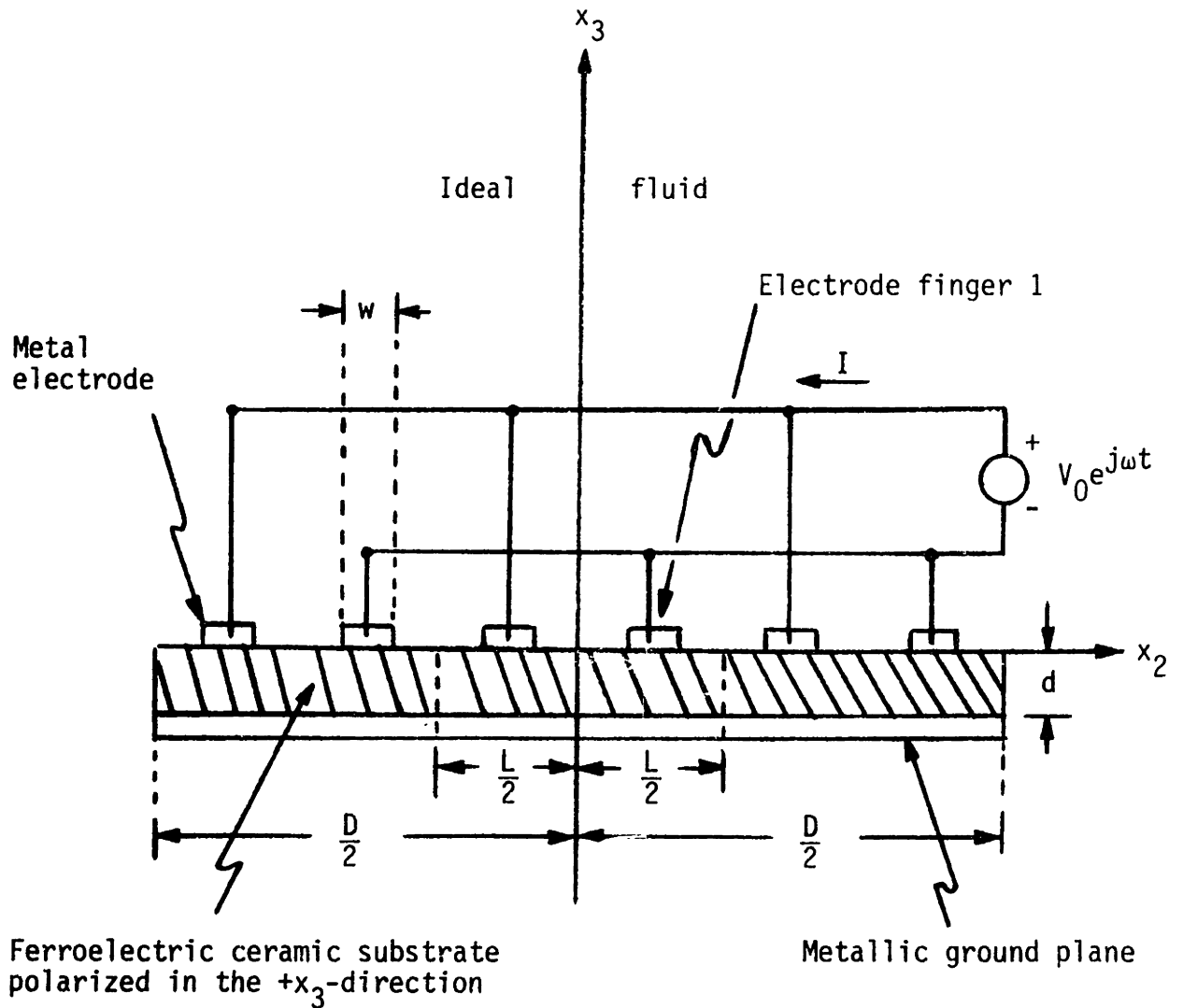
Figure A2-1. Side view of finite aperture thin transducer. The transducer extends a distance $\frac{W}{2}$ in the $\pm x_1$-directions.

$$S_1 = 0 = s_{11}^E T_1 + s_{12}^E T_2 + d_{31} E_3 \qquad (A2\text{-}11)$$

$$S_2 = s_{12}^E T_1 + s_{11}^E T_2 + d_{31} E_3 \qquad (A2\text{-}12)$$

$$S_3 = s_{13}^E T_1 + s_{13}^E T_2 + d_{33} E_3 \qquad (A2\text{-}13)$$

$$D_3 = d_{31} T_1 + d_{31} T_2 + \varepsilon_{33}^T E_3 \qquad (A2\text{-}14)$$

Equation (A2-11) can be used to eliminate T_1,

$$S_2 = s_{11}^E \left[1 - (\sigma^E)^2\right] T_2 + d_{31} (1 + \sigma^E) E_3 \qquad (A2\text{-}15)$$

$$D_3 = d_{31} (1 + \sigma^E) T_2 + \left(\varepsilon_{33}^T - \frac{d_{31}^2}{s_{11}^E}\right) E_3 \qquad (A2\text{-}16)$$

$$S_3 = s_{13}^E (1 + \sigma^E) T_2 + \left(d_{33} - \frac{d_{31} s_{13}^E}{s_{11}^E}\right) E_3 \qquad (A2\text{-}17)$$

where

$$\sigma^E = -\frac{s_{12}^E}{s_{11}^E} \quad . \qquad (A2\text{-}18)$$

For regions of the piezoelectric substrate not under an interdigitated finger, D_3 must be zero because no free charge can come or go in the absence of an electrode. For these regions, Eqs. (A2-15) and (A2-16) become

$$S_2 = s_{11}^D \left[1 - (\sigma^D)^2\right] T_2 \qquad (A2\text{-}19)$$

$$S_3 = s_{13}^D \left[1 + \sigma^D\right] T_2 \qquad (A2\text{-}20)$$

with

$$\sigma^D = -\frac{s_{12}^D}{s_{11}^D} \quad . \qquad (A2\text{-}21)$$

Here s_{ij}^D is the elastic compliance evaluated at constant D.

The parameters s_{ij}^E and s_{ij}^D may differ by as much as 50%; nonetheless, following Holland and EerNisse (ref. 17, pp. 44-53), Eqs. (A2-15) through (A2-21) can be combined into a single set of equations approximately valid over the entire substrate except perhaps near the edges,

$$S_2 = \hat{s}_{11}T_2 + \hat{d}_{31}\hat{E}_3 \tag{A2-22}$$

$$D_3 = \hat{d}_{31}T_2 + \hat{\epsilon}_{33}\hat{E}_3 \tag{A2-23}$$

$$S_3 = \hat{s}_{13}T_2 + \hat{d}_{33}\hat{E}_3 \tag{A2-24}$$

where

$$\hat{E}_3 = \begin{cases} \pm \dfrac{V_0 e^{j\omega t}}{d} & \text{under an electrode finger} \\ \\ 0 & \text{elsewhere} \end{cases} \tag{A2-25}$$

$$\hat{d}_{31} = d_{31}\left(1 + \sigma^E\right) \tag{A2-26}$$

$$\hat{\epsilon}_{33} = \epsilon_{33}^T - \frac{d_{31}^2}{s_{11}^E} \tag{A2-27}$$

$$\hat{s}_{11} = \frac{2w}{L} s_{11}^E\left[1 - (\sigma^E)^2\right] + \left(1 - \frac{2w}{L}\right) s_{11}^D\left[1 - (\sigma^D)^2\right] \tag{A2-28}$$

$$\hat{s}_{13} = \frac{2w}{L} s_{13}^E\left(1 + \sigma^E\right) + \left(1 - \frac{2w}{L}\right) s_{13}^D\left(1 + \sigma^D\right) \quad . \tag{A2-29}$$

The averaged constants $\hat{s}_{11}$ and $\hat{s}_{22}$ can be specified along the lines suggested by Holland and EerNisse (ref. 17, p. 45), but we have simply weighted the averages according to the fractions of electroded and unelectroded substrate areas.

By differentiating Eq. (A2-22),

$$\frac{\partial S_2}{\partial X_2} = \frac{\partial^2 u_2}{\partial X_2^2} = \hat{s}_{11} \frac{\partial T_2}{\partial X_2} + \hat{d}_{31} \frac{\partial \hat{E}_3}{\partial X_2} \quad , \tag{A2-30}$$

and using Newton's law,

$$\frac{\partial T_2}{\partial X_2} = \rho_s \frac{\partial^2 u_2}{\partial t^2} \quad , \tag{A2-31}$$

we obtain

$$\frac{\partial^2 u_2}{\partial X_2^2} - \frac{1}{v^2} \frac{\partial^2 u_2}{\partial t^2} = \hat{d}_{31} \frac{\partial \hat{E}_3}{\partial X_2} \quad , \tag{A2-32}$$

where

$$v^2 = \frac{1}{\rho_s \hat{s}_{11}} \quad . \tag{A2-33}$$

Here ρ_s is the substrate density.

Equation (A2-32) is a wave equation for material particle displacement u_2 with the driving function $\hat{d}_{31} \frac{\partial \hat{E}_3}{\partial X_2}$. In order to solve (A2-32) for a given driving function, it is necessary to specify the substrate boundary conditions at $x_2 = \pm \frac{D}{2}$. According to thin transducer assumption 2, stress-free conditions exist at the substrate edges,

$$T_2 = 0 \quad \text{for} \quad x_2 = \pm \frac{D}{2} \quad . \tag{A2-34}$$

Using (A2-22), the conditions (A2-34) become

$$\frac{\partial u_2}{\partial X_2} - d_{31} E_3 = 0 \quad \text{at} \quad X_2 = \pm \frac{D}{2} \quad . \tag{A2-35}$$

We solve (A2-32) under sinusoidal steady-state conditions; therefore all relevant variables are to be regarded as containing a suppressed $e^{j\omega t}$ time dependence. Equation (A2-32) becomes

$$\frac{\partial^2 u_2}{\partial X_2^2} + \left(\frac{\omega}{v}\right)^2 u_2 = \hat{d}_{31} \frac{\partial \hat{E}_3}{\partial X_2} \tag{A2-36}$$

with boundary conditions (A2-35). From Eq. (A2-25) and Fig. A2-1, we observe that over the region $|x_2| < \frac{D}{2}$, $\hat{E}_3$ is periodic in x_2 with period L, as shown in Fig. A2-2. We may therefore express $\hat{E}_3$ in terms of its Fourier transform,

$$\hat{E}_3(x_2) = \sum_{\substack{n=1 \\ n \text{ odd}}}^{\infty} e_n \sin\left(\frac{2\pi n x_2}{L}\right) \tag{A2-37}$$

where

$$e_n = \left(\frac{2V_0}{n\pi d}\right)(-1)^{\left(\frac{n-1}{2}\right)} \sin\left(\frac{n\pi w}{L}\right) \quad . \tag{A2-38}$$

Only sine terms and odd harmonics appear in Eq. (A2-37) because of the symmetry of $\hat{E}_3(x_2)$ evident in Fig. A2-2.

The solution for material particle displacement $u_2(x_2)$ can be obtained by first solving (A2-36) and the homogeneous boundary conditions (A2-35) for each driving function,

$$\hat{d}_{31} \frac{\partial \hat{E}_3}{\partial x_2} = \left(\frac{2\pi n}{L}\right) \hat{d}_{31} e_n \cos\left(\frac{2\pi n x_2}{L}\right) \quad . \tag{A2-39}$$

These results may then be summed to obtain the total solution, namely

$$u_2(x_2) = \sum_{\substack{n=1 \\ n \text{ odd}}}^{\infty} \left[\frac{e_n \hat{d}_{31}}{\left(\frac{\omega}{\nu}\right)^2 - \left(\frac{2\pi n}{L}\right)^2}\right]\left[\left(\frac{2\pi n}{L}\right) \cos\left(\frac{2\pi n x_2}{L}\right)\right.$$

$$\left. - \frac{\left(\frac{\omega}{\nu}\right) \sin\left(\frac{n\pi D}{L}\right) \cos\left(\frac{\omega x_2}{\nu}\right)}{\sin\left(\frac{\omega D}{2\nu}\right)}\right] \quad \text{for} \quad |x_2| < \frac{D}{2} \quad . \tag{A2-40}$$

If this solution for $u_2(x_2)$, along with (A2-37) for $\hat{E}_3(x_2)$, is substituted into (A2-22), we can solve for stress T_2; in turn T_2 can be used in (A2-24) to find strain component S_3. Since the transducer is thin, knowledge of S_3 allows us to determine $u_3(x_1,x_2,0)$, the normal component
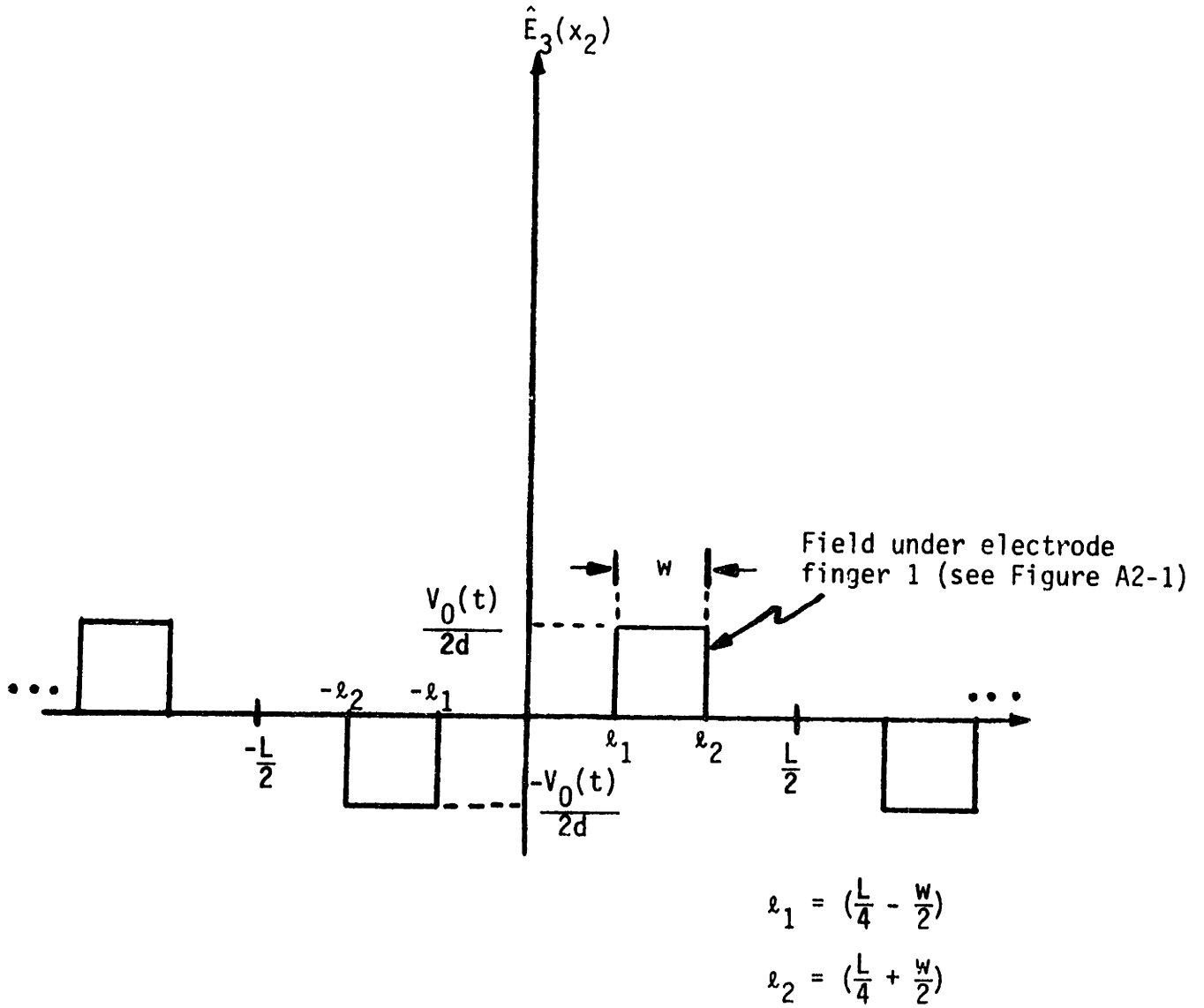
Figure A2-2. Plot of $\hat{E}_3(x_2)$ versus x_2.

$$\ell_1 = \left(\frac{L}{4} - \frac{W}{2}\right)$$

$$\ell_2 = \left(\frac{L}{4} + \frac{W}{2}\right)$$

of substrate surface deformation, as follows. According to thin transducer assumption 4 and the definition of mechanical strain,

$$S_3 = \frac{\partial u_3}{\partial x_3}$$

$$\approx \frac{u_3(x_1,x_2,0) - u_3\left(x_1,x_2,-\frac{d}{2}\right)}{\left(\frac{d}{2}\right)} \qquad . \qquad (A2-41)$$

The center of mass of the transducer must remain fixed for the case of light mechanical loading (thin transducer assumption 5), so

$$u_3\left(x_1,x_2,-\frac{d}{2}\right) = 0 \qquad . \qquad (A2-42)$$

Combining Eqs. (A2-41) and (A2-42),

$$u_3(x_1,x_2,x_3)\Big|_{x_3=0} = \left(\frac{d}{2}\right) S_3(x_2) \qquad . \qquad (A2-43)$$

Therefore, after finding S_3 as discussed above, Eq. (A2-43) can be used to determine the normal component of substrate surface deformation considered extensively in Chapters 2, 3 and 4 where we used the notation

$$\delta(y) = u_3(x_1,x_2,x_3)\Big|_{x_3=0} \qquad . \qquad (A2-44)$$

The final result is

$$u_3(x_1,x_2,0) = \delta(y) = V_0 \sum_{\substack{n=1 \\ n \text{ odd}}}^{\infty} \Delta_n \sin\left(\frac{2\pi n x_2}{L}\right) + V_0 H \sin\left(\frac{\omega x_2}{v}\right) , \qquad (A2-45)$$

where

$$\Delta_n = \left[\frac{(-1)^{\left(\frac{n-1}{2}\right)} \sin\left(\frac{n\pi w}{L}\right)}{n\pi} \right] \left[\hat{d}_{33} - \hat{\hat{d}}_{31} - \frac{\hat{\hat{d}}_{31}\left(\frac{2\pi n}{L}\right)^2}{\left(\frac{\omega}{v}\right)^2 - \left(\frac{2\pi n}{L}\right)^2} \right] \qquad (A2-46)$$

$$H = \sum_{\substack{n=1 \\ n \text{ odd}}}^{\infty} \left[\frac{(-1)^{\left(\frac{n-1}{2}\right)} \sin\left(\frac{n\pi w}{L}\right)}{n\pi} \right] \left[\hat{d}_{31} + \frac{\hat{\hat{d}}_{31}\left(\frac{2\pi n}{L}\right)^2}{\left(\frac{\omega}{v}\right)^2 - \left(\frac{2\pi n}{L}\right)^2} \frac{\sin\left(\frac{n\pi D}{L}\right)}{\sin\left(\frac{\omega D}{2v}\right)} \right] \quad \text{(A2-47)}$$

$$\hat{\hat{d}}_{31} = \hat{d}_{31}\left(\frac{\hat{S}_{13}}{\hat{S}_{11}}\right) \quad . \quad \text{(A2-48)}$$

The derivation of Eq. (A2-45) completes the first of the three objectives stated at the beginning of this appendix. Next, we determine the transducer terminal current 1 (see Fig. A2-1).

The electric current into an electrode finger is the negative of the time derivative of the electric displacement, D_3, integrated over that electrode. Using Eq. (A2-22) in (A2-23), we find

$$D_3 = \left(\frac{\hat{d}_{31}}{\hat{S}_{11}}\right) S_2 + \left[\hat{\epsilon}_{33} - \frac{(\hat{d}_{31})^2}{\hat{S}_{11}} \right] \hat{E}_3$$

$$= \left(\frac{\hat{d}_{31}}{\hat{S}_{11}}\right) \frac{\partial u_2}{\partial x_2} + \left[\hat{\epsilon}_{33} - \frac{(\hat{d}_{31})^2}{\hat{S}_{11}} \right] \hat{E}_3 \quad . \quad \text{(A2-49)}$$

The total transducer terminal current, I, is obtained by integrating (A2-49) over electrode finger 1 in Fig. A2-2, differentiating with respect to time, and then multiplying by the total number N,

$$N = \frac{D}{L} \quad , \quad \text{(A2-50)}$$

of transducer electrode finger pairs. The result of these computations is

$$I = j\omega C_0 V_0 + V_0 Y_p(j\omega) + V_0 Y_h(j\omega) \quad \text{(A2-51)}$$

where

$$C_0 = \left(\frac{WD}{2d}\right)\left(\frac{w}{L}\right)\left[\hat{\epsilon}_{33} - \frac{(\hat{d}_{31})^2}{\hat{S}_{11}} \right] \quad \text{(A2-52)}$$

$$Y_p(j\omega) = j\frac{\omega WD}{d}\sum_{\substack{n=1\\ n\ odd}}^{\infty}\frac{2(\hat{d}_{31})^2\sin^2\left(\frac{n\pi W}{L}\right)}{n^2\pi^2\,\hat{s}_{11}\left[1-\left(\frac{L\omega}{2\pi n v}\right)^2\right]} \tag{A2-53}$$

$$Y_h(j\omega) = j\frac{WD}{d}\sum_{\substack{n=1\\ n\ odd}}^{\infty}\left\{\frac{(\hat{d}_{31})^2 L\,\omega^2(-1)^{\left(\frac{n+1}{2}\right)}\sin\left(\frac{n\pi W}{L}\right)\sin\left(\frac{n\pi D}{L}\right)}{n^2\pi^2\,v\,\hat{s}_{11}\left[1-\left(\frac{L\omega}{2\pi n v}\right)^2\right]}\right\}$$

$$\left\{\frac{\sin\left(\frac{\omega L}{4v}\right)\sin\left(\frac{\omega W}{2v}\right)}{\sin\left(\frac{\omega D}{2v}\right)}\right\} \ . \tag{A2-54}$$

It is evident from Eq. (A2-51) that we may consider the electrical admittance of the transducer as resulting from the parallel combination of three elements:

1. "Clamped" capacitance, C_0, which is equal to the electrical capacitance that would be measured across the transducer terminals if the substrate could be clamped to prevent any lateral movement (i.e., if $u_2(x_2) = 0$ in Eq. (A2-49))

2. an admittance $Y_p(j\omega)$ due to the driven substrate response (see Section 4-2)

3. an admittance $Y_h(j\omega)$ due to the homogeneous substrate response (see Section 4-2).

Our final task, as stated at the beginning of this appendix, is the derivation of the Q of the fundamental resonance of the transducer. The fundamental resonance of the transducer is the resonance of the first term (n=1) of the summation on the right side of (A2-40), occurring at the temporal frequency

$$\omega_r = \frac{2\pi v}{L} \ . \tag{A2-55}$$

We assume the substrate motion consists of a single traveling wave moving in the $+x_2$-direction,

$$u_{2r}(x_2) = e^{-j\frac{\omega_r}{v}x_2} \qquad (A2-56)$$

(recall that $u_{2r}(x_2)$ contains a suppressed $e^{j\omega_r t}$ time dependence). Substituting Eq. (A2-56) into (A2-36), we see that

$$\hat{E}_3(x_2) = 0 \quad ; \qquad (A2-57)$$

therefore the fundamental transducer resonance corresponds to a short-circuit natural frequency as seen from the transducer electrical ports. This observation also follows from (A2-53).

According to the substrate analysis performed thus far, the Q of the fundamental transducer resonance should be infinite because no electrical or mechanical loss mechanisms have been considered. But if the transducer produces acoustic radiation, conservation of energy requires that the transducer substrate experience some loss due to mechanical-to-acoustic energy conversion. Thus we now "perturb" our earlier analysis by assuming finite mechanical Q of the transducer substrate motion to account for energy loss due to acoustic radiation.

The Q of the transducer may be calculated as follows:[35]

$$Q = 2\pi\left[\frac{\text{average energy stored at the resonant frequency}}{\text{energy dissipated per cycle at resonant frequency}}\right]$$

$$(A2-58)$$

For a large transducer (compared to an acoustic wavelength), we must determine the average energy stored per unit substrate area under the conditions (A2-56) and (A2-57). According to Ref. 7 (page 189), the total energy stored per unit substrate volume is

$$u = \frac{1}{2} \sum_{i=1}^{6} S_i T_i + \frac{1}{2} \sum_{i=1}^{3} E_i D_i \quad . \tag{A2-59}$$

Therefore the average energy stored per unit cycle per unit area in the substrate is

$$\left(\frac{d}{4 \hat{s}_{11}}\right)\left(\frac{\omega_r}{\nu}\right)^2 \quad , \tag{A2-60}$$

where Eqs. (A2-59), (A2-57), (A2-56) and (A2-22) have been used to obtain (A2-60).

Equations (A2-22), (A2-24) and (A2-57) yield

$$S_3 = \left(\frac{\hat{s}_{13}}{\hat{s}_{11}}\right) S_2 \quad . \tag{A2-61}$$

This result, together with (A2-56) and (A2-43), determines

$$u_3(x_1,x_2,0) = -j\left(\frac{\omega_r}{\nu}\right)\left(\frac{d}{2}\right)\left(\frac{\hat{s}_{13}}{\hat{s}_{11}}\right) e^{-j \frac{\omega_r}{\nu} x_2} \quad . \tag{A2-62}$$

From Appendix I, Eq. (A2-62) will produce acoustic radiation at angle θ with respect to the transducer normal, where

$$\sin\theta = \frac{2\pi c}{L\omega_r} = \frac{c}{\nu} \quad . \tag{A2-63}$$

From (A1-7), the radiated acoustic pressure amplitude is

$$P_{rad} = -\left(\frac{\rho c d \omega_r^2}{2\nu \cos\theta}\right)\left(\frac{\hat{s}_{13}}{\hat{s}_{11}}\right) \quad . \tag{A2-64}$$

Hence the averaged radiated power per unit substrate area is

$$\frac{1}{2} \frac{|P_{rad}|^2}{\rho c} \cos\theta = \left(\frac{\rho c d^2 \omega_r^4}{8\nu^2 \cos\theta}\right)\left(\frac{\hat{s}_{13}}{\hat{s}_{11}}\right)^2 \quad . \tag{A2-65}$$

Finally, we can combine Eqs. (A2-33), (A2-58), (A2-60), (A2-63) and (A2-65) to find the transducer Q,

$$Q_{(one\ lobe)} = \left(\frac{1}{2\pi^2}\right)\left(\frac{L}{d}\right)\left(\frac{\rho_s}{\rho}\right)\left(\frac{\hat{s}_{11}}{\hat{s}_{13}}\right)^2\left[\left(\frac{v}{c}\right)^2 - 1\right]^{\frac{1}{2}} \qquad (A2\text{-}66)$$

Since the traveling wave described in (A2-62) produces a single radiation lobe (see Appendix I and Section 2.4), the Q given in (A2-66) applies to one lobe only. However, the prototype transducer discussed in Chapter 2 is inherently bi-directional, and produces two symmetrically-located radiation lobes; therefore the $Q_{(one\ lobe)}$ given in (A2-66) should be divided by two in order to find the total substrate Q for the bi-directional transducer.

Appendix III

CIRCUIT DIAGRAMS

This appendix supplies schematic diagrams for the transmitter, receiver and timer used in the experimental apparatus diagrammed in Fig. 5-4. The receiver functions as a low-noise RF preamplifier for the spectrum analyzer (see Fig. 5-4) and isolates the sensitive input stage of the spectrum analyzer from the transmitter output. Important receiver characteristics are its 3 dB noise figure when operated from a 50 Ω source and its 4 μs recovery time from overload.

The transmitter is essentially a high-speed current-output switch. The transmitter has two TTL inputs, $\overline{G}$ and $\overline{S}$, which determine its short-circuit output current I_{sc} according to the following table:

$\overline{G}$	$\overline{S}$	I_{sc}
0	0	$+ I_t$
0	1	$- I_t$
1	1	0
1	0	0

The current I_t is adjustable from 0 mA to 100 mA using the ten-turn potentiometer in Fig. A3-2.

A timer suitable for the experimental apparatus diagrammed in Fig. 5-4 could be implemented in a straightforward manner using commercially available pulse generators, such as found in most electronics laboratories. For purposes of documentation, the timer actually used is shown in Figs. A3-3a and A3-3b; this timer is substantially more versatile than required for the apparatus in Fig. 5-4.
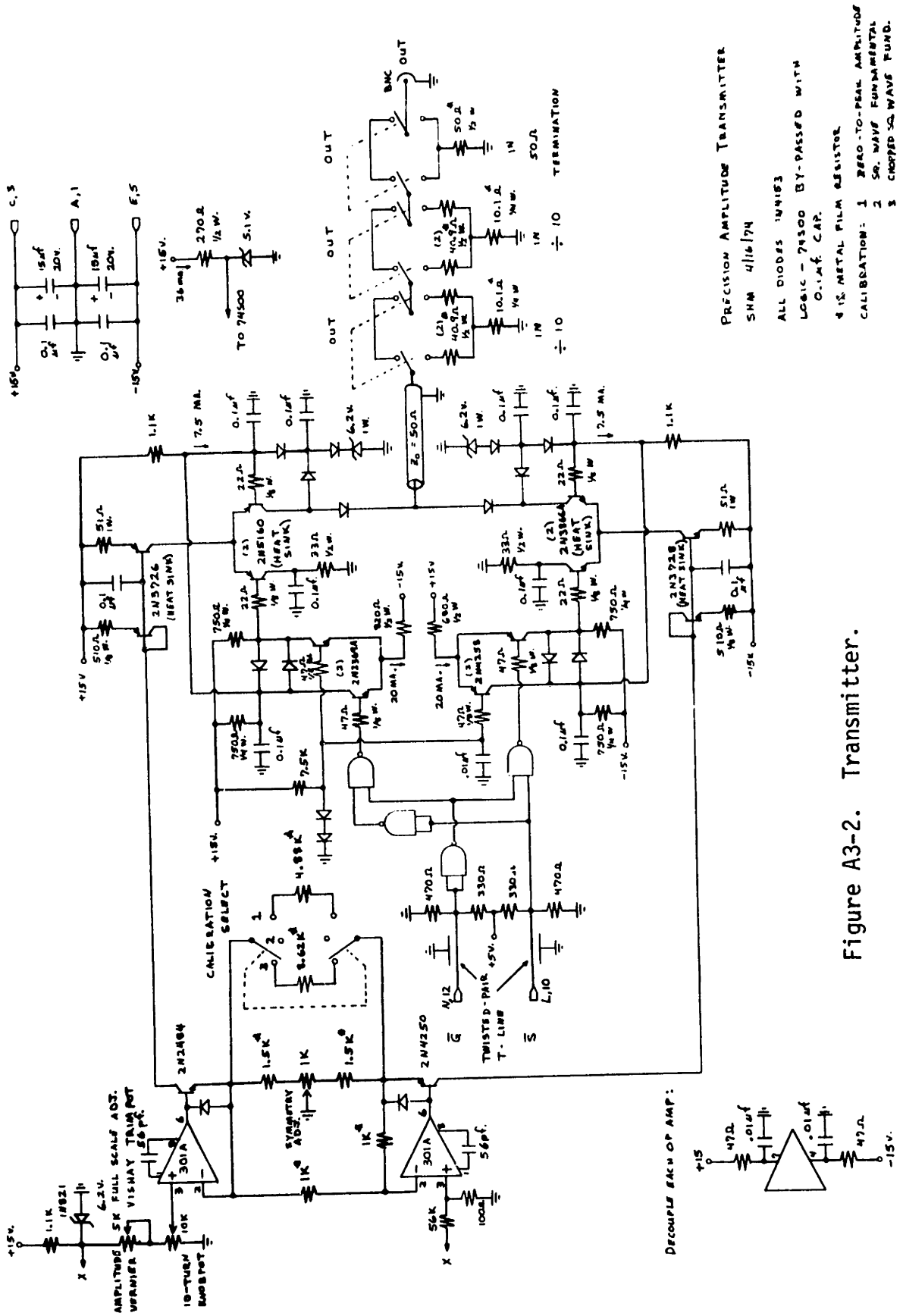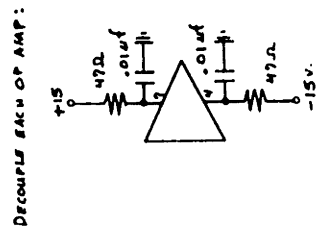
Figure A3-1. Receiver.

Figure A3-2. Transmitter.

Figure A3-3a. Timer Board A.

Figure A3-3b. Timer Board B.

Timer Board A converts the output of the tracking generator in Fig. 5-4 (connected to "ext clock in" in Fig. A3-3a) to TTL logic levels. Timer Board A also determines the repetition rate for the pulse-echo measurements and generates a 1.5 µs pulse to control the sample-and-hold shown in Fig. 5-4.

The only section of Timer Board B used with the experimental apparatus of Fig. 5-4 is the "analog pulse duration" one-shot which selects the transmitted pulse width. For all experimental measurements reported in Chapter 5, the pulse width was adjusted to 250 µs. Other switch settings for Timer Board B when used in the experimental apparatus of Fig. 5-4 are:

Switch Name:	Switch Setting:
select waveform	square wave
pulse duration	analog (anl.)
function	timer

The remaining logic circuitry on Timer Board B (which is unused in Fig. 5-4) allows the transmitter pulse duration to be digitally controlled by setting the "pulse duration" switch to "digital" (dig.). In this mode, the transmitter produces an N-cycle square-wave burst instead of the 250 µs pulse width used for the apparatus diagrammed in Fig. 5-4. The number N of cycles in this burst is determined by the setting of the Digi-switch (Z-12 in Fig. A3-3b).

Table A3-1 is an interconnection list for the transmitter, receiver and timer. Each circuit was built on a 4.5" × 6.5" card and mounted in a rack within a few inches of one another. The transmitter and receiver were constructed on ground planes, and the receiver was placed in a shielded box to prevent interference from the timer.

Table A3-1.   Interconnection list for transmitter,
receiver and timer shown in Figs. A3-1 through A3-3.

Function	Timer Board A	Timer Board B	Transmitter	Receiver
Dig Gnd	Z, 22	Z, 22	Z, 22	
+5V	X, 20	X, 20	X, 20	
Int Sync	Y, 21	Y, 21		
Int CKA	V, 18	V, 18		
Int $\overline{CKA}$	U, 17	U, 17		
Int CKB	T, 16	T, 16		
Int $\overline{CKB}$	S, 15	S, 15		
Gate A	R, 14	R, 14		
G		P, 13		
$\overline{G}$		N, 12	N, 12	
S		M, 11		
$\overline{S}$		L, 10	L, 10	
Int Trig	W, 19	W, 19		
Anl Gnd			A, 1	A, 1
+ 15V			C, 3	C, 3
- 15V			E, 5	E, 5

BIOGRAPHICAL NOTE

Samuel H. Maslak was born in Washington, D. C., on July 23, 1948.
He attended Massachusetts Institute of Technology, receiving the S.B.,
S.M. and E.E. degrees in Electrical Engineering in June, 1971. While a
graduate student, he received an NSF Fellowship for graduate study and
has been a Research Assistant at Lincoln Laboratory, Lexington, Massa-
chusetts since 1971. He has been employed as a consultant by Microbit
Corporation, Lexington, Massachusetts; Eastman Kodak Company, Rochester,
New York and the Non-Invasive Diagnostics Laboratory of Massachusetts
General Hospital. Mr. Maslak is a member of Sigma Xi.